AN ABSTRACT OF THE DISSERTATION OF

Gregory E. Guannel for the degree of Doctor of Philosophy in Civil Engineering presented on September 25, 2009.

Title:

Observations of Cross-Shore Sediment Transport and Formulation of the Undertow

Abstract approved:

H. Tuba Özkan-Haller

A new set of data from a large-scale sand bar migration experiment is presented. During this experiment, two sandbars were generated. One of the bar was generated by the action of undertow, and sediment moved offshore. The other bar was generated by the shoreward movement of sediment coming from the first bar. The principal mechanism responsible for shoreward movement is associated with effects of velocity asymmetry. Analysis of bathymetric surveys and suspended sediment concentration data reveals that suspended load contributed to a large extent to the formation of the first bar. Bed load was also important, and was moving in the same direction as suspended load. For the second bar, shoreward sediment movement occurred as bedload. Suspended load was moving in the opposite direction as bed load. This difference in sediment movement is explained by the predominance of the undertow in the suspended sediment flux. Two models were tested to reproduce the observed sediment transport, a wave-averaged (energetics) model and a wave-resolved model. After proper calibration, both models yielded satisfactory results. Calibration efforts highlighted the need for robust models of sediment pickup functions and sediment eddy diffusivity. They also showed the need for a deterministic undertow models. Formulations of the undertow are presented. These formulations are valid for all

relative water depths, and include mean current advective terms. These formulations show that the forcing of the undertow is depth-uniform, assuming linear water wave theory. The model is tested against four datasets to evaluate the possibility of a deterministic model. Although a constant eddy viscosity would yield such a model, no universal parametrization could be determined.

Observations of Cross-Shore Sediment Transport and Formulation of the Undertow

by

Gregory E. Guannel

A DISSERTATION

submitted to

Oregon State University

in partial fulfillment of
the requirements for the
degree of

Doctor of Philosophy

Presented September 25, 2009

Commencement June 2010

Doctor of Philosophy dissertation of Gregory E. Guannel

presented on September 25, 2009

APPROVED:

Major Professor, representing Civil Engineering

Head of the School of Civil and Construction Engineering

Dean of the Graduate School

I understand that my dissertation will become part of the permanent collection of the Oregon State University libraries. My signature below authorizes release of my dissertation to any reader upon request

---

Gregory E. Guannel, Author

ACKNOWLEDGEMENTS

I would like to first thank my Advisor, Dr. H.Tuba Özkan-Haller for her mentoring, support and leadership. I would also like to thank my committee members. First, I would like to thank Dr. Daniel Cox, my Master of Science Advisor, for his mentoring and research ideas. I would also like to thank him for some of the undertow dataset that I used in my research. I would like to thank Dr. Merrick Haller who provided me with insightful comments when I was developing research ideas. Finally, I would like to thank Dr. Jonathan Nash for showing me the beauty of $u\partial_x u$.

I would also like to thank all members of the CIL and the Coastal and Ocean Engineering Program. In particular, I would like to thank Dr. Rob Holman, for creating such a great environment. Also, I would like to thank Greg Wilson, Lisa Andes and Jeremy Mull for their great (late night) companionship. And of course, I would like to thank Joe Long, Meg Palmsten, Kristen Splinter, Patricio Catalan and Erica Harris for their support and help.

Finally, I would like to thank my wife, Michele, my parents, my brothers, my extended family, and my longtime friends for their unconditional support.

TABLE OF CONTENTS

TABLE OF CONTENTS (Continued)

Page

TABLE OF CONTENTS (Continued)

Page

TABLE OF CONTENTS (Continued)

Page

LIST OF FIGURES

LIST OF FIGURES (Continued)

Figure Page

LIST OF FIGURES (Continued)

Figure Page

LIST OF TABLES

OBSERVATIONS OF CROSS-SHORE SEDIMENT TRANSPORT AND FORMULATION OF THE UNDERTOW

1. GENERAL INTRODUCTION

Coastlines are dynamic environments that undergo forcing from fluid motions that span the frequency band from seconds to years (Holman *et al.* (1989)). In response to this forcing, coastlines evolve: they lose or gain sediment, or sometimes they attain a state of equilibrium (Komar (1998)). Coastlines are also a place where most humans live. In the U.S. alone, more than 50% of the population lives 1 hour or less from the coast. Public as well as private infrastructures and developments that are built on coastlines sometimes disrupt the shoreline's natural response to wave forcing, and are often endangered by such response. As a result, roads, ports, houses or towns often fall into the sea or are faced with unmanageable supplies of sand.

The mission of coastal engineers is to help remedy these problems. They rely on empirical as well as theoretical tools that are constantly updated as more is learned about nearshore processes. One type of process that is particularly puzzling is cross-shore sediment transport. Although longshore currents, generated by obliquely incident waves, transport millions of cubic yards of sediment a year and are more energetic than cross-shore currents, cross-shore sedimentary processes are responsible in great part for the inter-annual variability of shorelines (Komar (1998)).

Under the action of storm-generated waves, which tend to occur during the winter season, sediment is eroded from the upper portion of a beach and moves offshore. It often accumulates near the breakpoint to form a sand bar. The principal forcing mechanism for the mobilization and offshore transport of sediment is the undertow. The undertow is an

offshore-directed current which becomes stronger as waves are more energetic. Under the action of fair-weather waves, which tend to occur during the summer season, the undertow weakens, and the wave-generated non-linear orbital velocities move sediment shoreward.

Knowledge and modeling cross-shore sediment transport is important to coastal engineers and the scientific community for many reasons. Storms erode beaches in a matter of hours, and a better understanding of erosional forces can benefit the planning and maintenance of coastal infrastructures. Similarly, an understanding of the forcing mechanisms behind the shoreward movement of sand would improve the planning and design of beach replenishment projects. Finally, knowledge of long-term cross-shore variability is critical to understanding general beach ecology and dispersal of pollutants (Ruessink & Kuriyama (2008); Feddersen (2007); McLachlan *et al.* (1993)).

Modeling of cross-shore sediment transport has been approached from various theoretical point of views. Some models have been developed to predict general beach states and direction of sediment transport, based on hydrodynamic conditions and site characteristics (see, e.g., Kraus & Smith (1994); Roelvink & Brøker (1993); Lippmann & Holman (1990); Wright & Short (1984); Dean (1977)). Other models have been developed to evaluate change in bar morphology over relatively large temporal scales (i.e., days to years) based on general wave field and site characteristics (see, e.g., Marino-Tapia *et al.* (2007); Plant *et al.* (2001)). In this dissertation, we are interested in exploring the capabilities of process-based models, which predict shoreline evolution on a shorter time scale. These models are developed to reproduce in detail the forcing responsible for the mobilization and transport of sediment and, ultimately, for the movement of sandbars.

Process-based models have been proven successful when applied to offshore bar generation cases (Thornton *et al.* (1996); Gallagher *et al.* (1998); Henderson *et al.* (2004)). Yet, shoreward bar migration has been more difficult to model (Gallagher *et al.* (1998)). Some recent approaches show promise in modeling both cases (Hoefel & Elgar (2003); Hender-

son *et al.* (2004)). These models have confirmed that undertow is the primary forcing mechanism for offshore sediment transport. They have also highlighted the role of various nonlinear forcing mechanisms for moving sediment shoreward. However, questions remain as to the role of these forcing mechanisms in the mobilization and movement of sediment in the nearshore. Furthermore, it is unclear how sediment moves when bars are migrating offshore and shoreward. Two recent models achieved similar results in the modeling of bar migration, even though they are based on different assumptions. One model (Hoefel & Elgar (2003)) assumed that sediment moved as bedload and suspended load, and that effects of velocity asymmetry on the bed were important. Another model (Henderson *et al.* (2004)) assumed that all sediment moved as suspended load and bedload can be neglected. Finally, these models performed well when measured times series of velocity are used. Important forcing mechanisms such as undertow or irregular velocity fields are still difficult to model without proper calibration.

The main drawback to the reconciliation and/or to further development of sediment transport models is a lack of data on which to test them. Detailed observations of sediment transport on natural beaches, under various weather conditions, are sparse (Birkemeier (1984); Gallagher *et al.* (1998)). Laboratory datasets are easier to obtain, but the majority of experiments on sand movement have been performed in oscillatory water tunnels (van der Werf *et al.* (2009)) where non-linear features such as velocity asymmetry or boundary layer streaming can not reproduced. Only a few experiments have been conducted with irregular waves, in open wave flumes (Kraus & Smith (1994); Roelvink & Reniers (1995); Thorne *et al.* (2002); Ribberink *et al.* (2000)). Furthermore, many formulations for the undertow have been proposed, but they are often tested on a limited dataset. The few publications that compared different formulations on a same dataset indicated that they yield different results (Spielmann *et al.* (2004); Gallagher *et al.* (1998)).

In this dissertation, my objective is to evaluate in details the assumptions of two process-based models, and to compare them against a new dataset. I also compare the

differences between the different undertow formulations, and reconcile them when possible. The formulation of undertow is compared against four dataset in order to analyze the relative importance of its main components. This comparison also evaluates whether it is possible to create a simple, robust, deterministic undertow model.

The dissertation is organized as follows. In Chapter I, I present in detail the results of the CrossTex experiment. This experiment produced a high quality dataset of wave height measurement, suspended sediment concentration, remote sensing of bore fronts propagation and bathymetric changes, obtained under various wave fields (Magalen (2006)). Dr. T. Özkan-Haller, Dr. M. Haller, and Dr. J. Kirby led the experiment, assisted by J. Magalen, P. Teràn-Cobo, C. Scott, Dr. P. Catalàn and myself. First, I analyzed the temporal evolution of the different bars that we created, and evaluated the relative role of velocity moments in the observed total transport of sediment. Next, I analyzed records of suspended sediment time series to determine the forcing mechanisms behind cross-shore suspended sediment flux. I also evaluated the relative importance of modes of sediment transport in the flume. Finally, I compared the performance of two process-based models at reproducing the observed transport: the Enhanced Energetics Model (EEM), proposed by Hoefel & Elgar (2003), and a combination of bedload and suspended sediment flux models, based on the eddy-diffusive boundary layer model proposed by Henderson *et al.* (2004). In particular, I evaluated whether these models reproduced the same mechanisms of sediment transport that we observed in the flume. The results presented in Chapter II will be submitted to *Marine Geology*.

Based on the findings of Chapter I, a correct formulation of the undertow is key to successful modeling of sediment transport. In Chapter II, I present the results of the theoretical formulation of the undertow based on linear wave theory. I conducted the derivations by relaxing the common assumption of shallow water waves, and I included effects of mean current advection terms as well as bottom shear stress. Under the same assumptions, I also highlighted the generality of the expression for mean shear stress at

the MWL that Deigaard & Fredsøe (1989) originally derived. Finally, I analyzed four datasets of undertow obtained under irregular waves conditions to evaluate whether a robust and simple deterministic model could be proposed. The datasets were collected by Sultan (1995), Okayasu & Katayama (1992), Garcez-Faria *et al.* (1998) and Scott *et al.* (2005). The results presented in Chapter III will be submitted to *Coastal Engineering*.

This research was made possible because of the gracious funding from NSF grant OCE-0351297 and OCE-0351153, and Sea Grant grant NA16RG1039. We wish to thank all the faculty and staff of the O.H. Hinsdale Wave Research Laboratory for their time and support during the experimental phase of CrossTex. The O.H. Hinsdale Wave Research Laboratory is partially supported by the George E. Brown Jr. Network for Earthquake Engineering Simulation (NEES) Consortium Incorporated contract OMSA v.3.1 through their National Science Foundation Cooperative Agreement CMS-0402490. Some of the instrumentation used during this experiment was purchased under National Science Foundation grant NSF-0429219. I thank Dr. Daniel Cox for some of the undertow data, and Dr. Patricio Catalàn for his help in computing percent of wave breaking from the Argus videos. I also thank Dr. S. Henderson for providing me with his eddy-diffusive hydrodynamic and sediment transport code.

2. 2. OBSERVATIONS OF CROSS-SHORE SEDIMENT TRANSPORT

2.1 Introduction

Sandbars are common features on beaches (Lippmann & Holman (1990)). They are an important element of the seasonal variation of coastlines (Keulegan (1945); Komar (1998); Ruessink & Kroon (1994)), and sometimes constitute a danger for mariners (Ross (2003)). Generally, under winter storm conditions, strong undertow currents move sediment offshore from the face of the beach to form a sandbar at, or near the breakpoint. Such understanding has been complemented by successful modeling of bar formation observed in the field (Thornton *et al.* (1996); Gallagher *et al.* (1998)). Under summer fair-weather conditions, sandbars move shoreward and degenerate, and the beach is replenished (Shepard (1950); Bascom (1953)).

The shoreward movement of sand is caused by nonlinear velocities induced by waves. Although purely sinusoidal waves cannot transport sand, nonlinear waves have the capacity to do so. As waves shoal, they are progressively affected by the bed, and their shape evolves from symmetric to skewed to asymmetric, before finally breaking. Skewed waves are characterized by high, peaky crests and shallow, flat troughs. They have strong shoreward, and weak offshore, velocities, which, over time, transport sand shoreward. This has been supported by observations (Osborne & Greenwood (1992a); Ribberink (1998)), as well as models of sediment transport (Trowbridge & Young (1989); Hsu & Hanes (2004)). Asymmetric, or 'saw-toothed' waves are characterized by sharp fronts and mild rears. Asymmetric waves have skewed acceleration profiles (Elgar *et al.* (1988)), which generate strong shoreward oriented horizontal pressure gradients on sand under their sharp front faces, and weak offshore oriented pressure gradients under their gentler rear faces. Thus, they have the capacity to transport sand shoreward. The effect of velocity asymmetry on

the shoreward transport of sand has been observed in various studies (Hanes & Huntley (1986); Gallagher *et al.* (1998); Nielsen (1982); Elgar *et al.* (2001)), and has generally been associated with bedload transport based on observations (King (1990); Dohmen-Janssen & Hanes (2002); Watanabe & Sato (2004)), and modeling (Drake & Calantoni (2001); Nielsen & Callaghan (2003)).

The incorporation of the effect of velocity asymmetry, or acceleration skewness, in models that only considered velocity skewness yielded successful results in the prediction, and quantification, of offshore and shoreward bar migration (Hoefel & Elgar (2003)). However, uncertainties remain as to the exact mode of transport of sediment during these phases of beach evolution. During both offshore and shoreward bar migration, sediment moves as bedload and suspended load (Bailard (1981); Bowen (1980); Jaffe *et al.* (1984); Hanes & Huntley (1986)). Models that had a strong bedload component successfully reproduced observed events of sandbars migration (Hoefel & Elgar (2003)). On the other hand, models that ignored the role of bedload, but assumed that all sediment transport occurred as suspended load, also reproduced the shoreward movement of sandbars successfully (Henderson *et al.* (2004)). Thus, in order to quantify the effectiveness of sediment transport models, it is necessary to not only evaluate their capacity at reproducing the total observed transport of sediment, but also their capacity at reproducing the relative balance between suspended and bedload.

Few experiments have been able to quantify the relative roles of bedload and suspended load in the total transport of sediment. For example, Janssen *et al.* (1997), Ribberink (1998) and Dohmen-Janssen & Hanes (2002) estimated that most of the transport that they observed in the laboratory occurred as bedload (sheet flow). Conley & Beach (2003) found in a field study that most of the suspended transport was concentrated in the bottom 5 cm of the water column, which would imply that bedload might have been important. Conversely, Aagaard *et al.* (1998) estimated that suspended load might be a substantial fraction of total sediment transport. Other estimates of the relative role of

bedload have been made from calculations using the energetics models (Ruessink *et al.* (1998); Gallagher *et al.* (1998)), and estimated that suspended load dominated over bedload.

Additionally, although there have been many studies on the relative importance of various wave frequency bands on suspended sediment transport (Hanes & Huntley (1986); Jaffe *et al.* (1984); Osborne & Greenwood (1992a); among others), few models successfully reproduced details of observed suspended sediment concentration time series in the surf zone (Black *et al.* (1995); Jaffe & Rubin (1996); Ogston & Sternberg (2002); Hsu & Liu (2004)). Most suspended sediment transport models (see, e.g., Henderson *et al.* (2004); van Rijn (2006)) use a sediment pickup function that is a function of shear stress (see Nielsen (1982); Fredsøe & Deigaard (1992); Soulsby (1997)) to mobilize and put sediment in suspension. They also assume that sediment eddy diffusivity can be represented by turbulent eddy viscosity in order to simulate sediment advection/diffusion in the water column. However, few studies attempted to relate eddy viscosity to eddy diffusivity (Lees (1981); Dyer & Soulsby (1988); Ogston & Sternberg (2002)), and there are indications that they are not always equal (Thorne *et al.* (2009)). Finally, there are even fewer models that describe the observed details of bedload and suspended load that resulted in bathymetric change (Ribberink & Al-Salem (1995)). Thus, questions persist as to the correct parametrization of bedload, sediment pickup function and sediment eddy diffusivity in shoreline evolution models.

In order to address these questions, we present in this paper results obtained during a large scale flume experiment. The objectives of this experiment were to obtain high quality datasets of sandbar migration under various wave fields. First, we sought to establish if offshore as well as shoreward sandbar movement could be reproduced in a laboratory setting, and under what type of wave conditions. Also, we evaluated the relationship between position of wave breaking and shoreward transport of sand, and the relative importance of suspended sediment on total sediment transport. Information gathered from

the laboratory experiment was then used to evaluate the performance two process-based models: a wave-averaged energetics model, proposed by Hoefel & Elgar (2003), and a wave resolving eddy-diffusive boundary layer model (Henderson *et al.* (2004)) which incorporates suspended and bedload transport.

This paper is organized as follow. In Section 2.2, we present our dataset. In Section 2.3, we describe the observed bathymetric changes, and relate cross-shore evolution of velocity moments (undertow, skewness and asymmetry) to observed total sediment fluxes. In Section 2.4, we analyze suspended sediment concentration time series, and evaluate the frequency dependence of suspended sediment flux. We also estimate the relative importance of suspended load in the flume compared to the total sediment transport. In Section 2.5, we present the wave-averaged model developed by Hoefel & Elgar (2003) and the wave-resolving model that we used on the dataset. The wave-resolving model consists of the suspended load model developed by Henderson *et al.* (2004), to which we added a bedload model based on the Meyer-Peter and Müller equations (Meyer-Peter & Müller (1948)). In Section 2.6, we present results of the modeling of sediment transport observed in the flume. We present our conclusions in Section 2.7.

2.2 Experimental Set-Up

2.2.1 Facility and Instrumentation

We conducted a large-scale study of sand movement in the Large Wave Flume (LWF) at the O.H. Hinsdale Wave Research Laboratory, Oregon State University (Figure 2.1) to generate a sandbar under storm condition and to induce shoreward transport of sediment under summer conditions. The LWF is 104 meters long, 3.7 meters wide and 4.6 meters deep, and was equipped with a flap-type wavemaker. The reference system in the flume is such that the origin is set at the wavemaker, with positive X pointing shoreward.

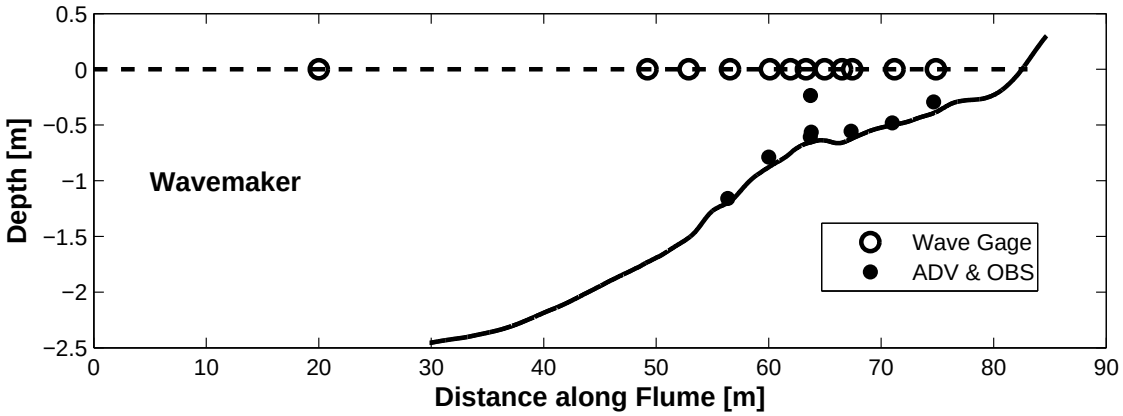

Fig. 2.1: Instrument's position along wave flume wall. Dots show position of ADV and OBS; circles show position of wave gages.

The flume was filled with well sorted, fine to medium natural sand. The basic sand characteristics were: median grain size 0.22 mm ($\phi = 2.18$); standard deviation $\sigma_\phi = 0.3$; estimated fall velocity at $w_o = 2.65$ cm/s (from Gibbs, 1971). Initial beach profile was adjusted to an average 1V:20H slope. The foreshore slope was 1:7, and the surf zone and offshore regions were 1:33 and 1:17, respectively.

To scale the experiment, we compared wave characteristics (height and period) and bar geometry observed in the flume (see Section 2.3) to conditions observed during DUCK94 (Gallagher *et al.* (1998)) and general characteristics of sandbars (Keulegan (1945, 1948), Miller *et al.* (2006)). We found that the experiment had an average 1:10 scale, which means that results presented herein should apply to natural beaches with coarse sediments. This type of beach is different from most of the beaches where sandbar migration was observed. However, it can be impractical to scale down sediment in laboratory flume; fine sediments are cohesive and carry electro-magnetic charges, lower density material such as plastic have different shape, angularity and porosity, and respond to forcing differently than sands (Soulsby & Damgaard (2005a)). We believe that conclusions drawn in this paper should be pertinent to general sand dynamics discussions, as will be shown in the following sections.

The experiment was conducted by running a series of waves over the mobile bed for periods (runs) of 20 min each (see Section 2.2.2). During each run, we measured water surface elevation, flow velocity, and sediment concentration at fixed locations in the flume using twelve resistance-type wave gages, eight wall-mounted Acoustic Doppler Velocimeters (ADVs) and co-located Optical Backscatter Sensors (OBS; see Figure 2.1 and Table 2.1). Each of the ADV and OBS were approximately 44 cm away from the wall of the flume.

Table 2.1: Position of Wall Mounted ADV and OBS

Position [m]	ADV	75	71	67	64	64	64	60	56
	OBS	75	71	67	64	64	64	60	56
Dist. abv. Bed [cm]		10	2	7	9	5	42	9	4

In addition to wall instruments, one wave gage, 8 ADV, 7 OBS, and 19 Fiber-Optic Backscatter Sensors (FOBS)were mounted on a cart (see Figure 2.2) equipped with a vertically moving frame, which allowed a variable placement of the instruments within the water column. The instruments were positioned on the mobile frame such that most of the measurement volumes for the FOBS and OBS were co-located with an ADV. However, some OBS and ADV were separated by as much as 96 cm across the flume. The 19 FOBS were separated into two vertical stacks, offset by 4 cm across the flume and 2 mm in the vertical. All instruments sampled at 50 Hz, except for the FOBS, which sampled at 10 Hz.

Between runs, we measured bathymetric changes offshore of the swash zone with an array of high-definition acoustic transducers mounted on the mobile cart. This array consisted of 32 transducers placed 8 cm apart across the flume, with sampling gaps of 66 cm and 49 cm between the ends of the array and the walls of the flume. The horizontal position of each sample was determined using a laser range finder that measured distance from a fixed target. In the swash zone, bed elevation was measured manually along a single cross-shore transect. Finally, three ARGUS video cameras (Holman & Stanley (2007)), which were sampling at 10 Hz, were mounted near the ceiling and were used episodically to quantify wave breaking conditions.

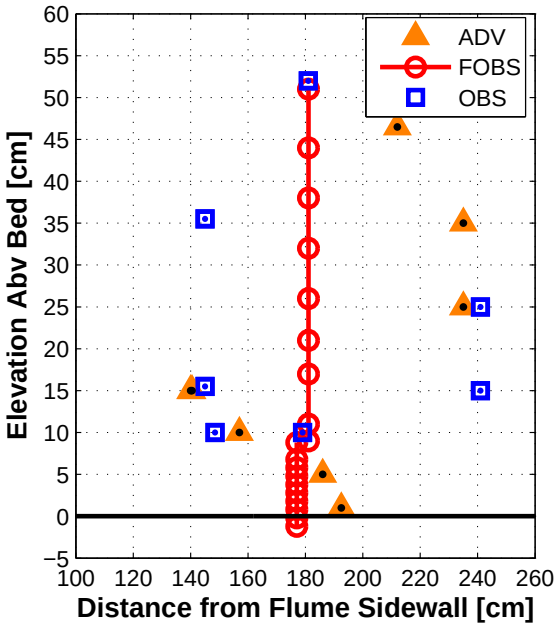

Fig. 2.2: Position of instruments on mobile cart. Distances on x-axis are measured from one of the flume sidewalls; flume total width=370 cm. Bed position is indicated by thick black line; ADV and OBS sample volume position indicated by back and blue dots.

2.2.2 Experimental Procedure, Data Processing and Quality Control

During a typical experimental run, we first positioned the mobile cart at a specified cross-shore location in the flume using the laser range finder. Next, when the water was shallower than approximately 2 m, we dropped the instrument frame until the sampling volume of the lowermost ADV sat 1 cm above the bed (cmab, hereafter). Under such conditions, the entire FOBS array spanned the vertical profile from -1.2 to 51 cmab. At one cross-section in the flume where the water was deeper than 2 m ($X \approx 45\,m$ in Figure 2.1) and where no significant bed change were observed (see Section 2.3), the water was too deep for the mobile frame to reach the bed, and lowermost FOBS and ADV were well above the bed. Once the instruments were in place, we produced a wave field by feeding various TMA spectra (Bouws *et al.* (1985)) to the LWF wavemaker.

Discrete experimental runs lasted 20 minutes. No waves were generated during the first minute of data collection in order to establish a baseline for all instruments. Next, waves were generated for 15 minutes, followed by 4 minutes of data collection without waves. After most wave runs, we conducted a bathymetric survey. At the completion of the experiment, 141 wave runs and 89 surveys had been generated. Further information on wave conditions and survey frequency is presented in Section 2.3.

We processed the velocity time series measured by ADV by first passing them through a phase-space-threshold filter (Goring & Nikora (2002)) followed by a signal-to-noise ratio and a correlation filter (Scott *et al.* (2005)). On some occasions, we applied an additional filter that identified remaining outliers that were 3 or 4 standard deviations above the signal mean. After visual inspection, we discarded time series that contained a large number of outliers, as identified by the combination of all these filters. As a result, we retained 1,583 out of 2,256 horizontal velocity time series. In the remaining time series, we replaced flagged points with a cubic spline interpolation.

We calibrated the OBS and FOBS data in a recirculation tank after the experiment concluded, following the method of Beach *et al.* (1992). Post-calibration, we used data from the quiescent period before the start of wave generation to remove any constant bias in the sensors. In each time series, we removed background concentration of fines using the method of Beach & Sternberg (1988). Also, we discarded outliers that deviated from the mean by more than 5 standard deviations. Time series were discarded due to excessive background noise. As a result, we utilized 93 out of the 141 records of FOBS time series.

The acoustic bathymetric surveys spanned from a depth of 20 cm to between 1.5 and 2.5 meters, with an average horizontal resolution of 6 cm. We first averaged alongshore transducer records to produce a single mean profile representative of the cross-shore bathymetric variation, then we smoothed the profile with a five-point running average filter. Finally, data from the ARGUS cameras were reduced to a cross-shore pixel ar-

ray with a cross-shore resolution of 1 cm. For further details regarding the rectification and merging of the image data, see Catalán (2005). The image data were used to identify breaking waves and quantify the cross-shore variation of the percent breaking. The procedure for breaking wave identification follows that of Caálan & Haller (2008). The percent of breaking waves represents the number of breaking waves identified in the video observations, normalized by the number of waves identified in the wave gages (with linear interpolation between the gages). For more information on the experiment procedure, the reader is referred to Magalen (2006).

2.3 Bathymetric and Hydrodynamic Observations

In this section, we describe the general bed evolution that we observed in the LWF during our experiment. Because our objective is to model sand transport under various wave fields, we will evaluate the relationship between hydrodynamic conditions and bed evolution. We will present information on the cross-shore evolution of wave height as well as velocity moments (mean, skewness and asymmetry) in the LWF.

We first define a few terms used in this paper. The term 'breakpoint' will stand for the location of maximum rms wave height, H_{rms}, and the term 'breaking ratio' will refer to the maximum value of wave height over total water depth H_{rms}/h. Surf zone will refer to the region in which most of the waves were breaking (generally more than 80%). Conversely, the shoaling region will refer to the section of the flume that was located offshore of the breakpoint, where minimal, if any, wave breaking occurred.

As will be shown in this section, we identified four phases of bed evolution, and the generation/degeneration of two sandbars. For each phase, which lasted an interval of time Δt, bed elevation changed by an amount $\Delta h(x)$. To quantify the total amount and the net direction of sediment movement that occurred during that time, we computed the net

sediment flux Q (Thornton *et al.* (1996)):

$$Q(x) = \int_{X_0}^{X} \frac{1}{1-n} \frac{\Delta h}{\Delta t}\, dx \tag{2.1}$$

where $n = 0.3$ represents a standard value of bed porosity. Based on our reference system, positive (negative) Q-values represent shoreward (offshore) sediment movement. Throughout the experiment, the sediment movement occurred between the shoreline and $X \approx 52\, m$ (see Figure 2.3). Consequently, we set the lower limit of the integral in Equation 2.1 at $X_0 = 40\, m$, where no bed changes occurred and $Q(X_0) \approx 0$. We computed the average sediment flux during a certain phase as:

$$\bar{q} = \frac{1}{L} \int_{X_0}^{X_0+L} |Q(x)|\, dx \tag{2.2}$$

where vertical bars represent absolute values. L represents the length of the region of active sediment movement, between X_0 and the shoreline.

We explored the spatial and temporal behavior of the sandbars by tracking their height, cross-shore position, and crest half-width. To simplify the tracking of bars' characteristics, we filtered out bedforms with a wavelength smaller than 2 m by passing measured bathymetric profiles over a 32-point running-average filter. Sandbars were identified as the most prominent features in the profiles. Bar crest and trough positions were located by finding the highest and lowest points on a sandbar. The height of a given bar was defined as the vertical distance between bar crest and trough. Bar position was defined as the horizontal distance of the bar crest from the origin (the wavemaker). Crest half-width was defined as the horizontal distance between the location of the bar crest and trough. Increasing (decreasing) cross-shore position values correspond to onshore (offshore) sandbar movement.

We computed wave height from wave gage time series as $H_{rms} = \sqrt{8\sigma^2}$, where σ^2 represents the variance of the free surface elevation $\eta(x,t)$. From spectra of free water

surface elevation time series measured along the flume, we estimated σ^2_{Wave}, the variance of the signal around the spectral peak $f_p = 1/T$, by band passing the spectrum between $0.1Hz \leq f \leq 4f_p$. We also estimated σ^2_{LF}, the variance of the signal in the low-frequency range, by low-pass filtering any frequency $f \leq 0.1$ Hz.

To quantify the relative importance of the undertow and wave-induced forcing on the observed total sediment transport, we computed velocity moments (undertow, asymmetry and skewness) by using all valid signals (see Section 2.2.2) measured at specific locations in the flume below 25 cmab. We used wall as well as cart ADV. We computed undertow strength by taking the mean of measured time series of velocity. Velocity skewness was computed by:

$$Skew = \frac{< \widetilde{u}^3 >}{\sigma(< \widetilde{u}^3 >)} \tag{2.3}$$

where $\sigma(\alpha)$ represents the standard deviation of a signal α, and $\widetilde{u}$ the wave velocity. Brackets represent the averaging operation. This velocity was computed by band-passing total velocity to remove seiching and turbulent signals(cutoff frequency for seiching was set at 0.1 Hz, and cutoff frequency for turbulence was set at $4f_p$ Hz, where f_p is the spectrum peak frequency). Velocity asymmetry was computed by estimating the skewness of the imaginary part of the Hilbert transform of the velocity signal (Elgar (1987); Elgar & Guza (1985)). Because skewness and asymmetry are normalized quantities, they generally vary between 0 and 1.

Finally, using linear wave theory (LWT) we modeled wave-averaged and roller momentum fluxes for various runs during offshore bar generation to evaluate the effects of bathymetric change on undertow. The depth-averaged mean current is defined as: $U_r = (Q_w + Q_r)/(\rho h)$, where $Q_w = E_w/C$ represents the wave mass flux, E_w is the wave energy density, C the wave celerity. $Q_r = 2E_r/C$ represents the mass flux of the roller (Svendsen (1984a)), and E_r is the roller energy density.

We computed wave energy density from modeled wave height. To reproduce observed

H_{rms}, we calibrated the model of Baldock *et al.* (1998) for wave dissipation and we used the breaking parameter proposed by Ruessink *et al.* (2003a). We used the model of Reniers & Battjes (1997) to model the energy flux due to rollers. We calibrated roller angle to minimize the error between measured and modeled mean water level (MWL, $\bar{\eta}(x)$).

2.3.1 Bed, Waves and Velocity Moment Evolution during Offshore Bar Generation

During the first 14 runs of the experiment, we produced relatively high energy waves to simulate storm conditions (Table 2.2). Design rms wave height during this period was $H_o = 0.42$ m, with a peak period of $T = 4$ s. During this period, an offshore sand bar formed at $X \approx 61$ m (see Figure 2.3a). In the surf zone, we observed the presence of offshore-migrating mega-ripples with an average length of 2.7 m and average height of 13 mm (see Figure 2.3a, at $X \approx 74\,m$). In the remainder of this paper, we will refer to this period as the offshore bar generation period ('OG' in the figures), and to this bar as bar O.

Table 2.2: Consecutive Wave Conditions during Experiment

Experimental Phase	Wave Run Interval	Wave Height [m]	Wave Period [s]	γ^*	Time** [min]
Offshore Bar Generation (OG)	1-14	0.42	4.0	2	210
Middle Bar Generation (MG)/Offshore Bar Degeneration	15-56	0.21-0.23	8.0	10	885
Middle Bar Stagnation (MS)	57-89	0.4-0.25	3.5	2	1,020
	23	0.28-0.23	5.5	2	1,350
Middle Bar Degeneration (MD)	90-141	0.23-0.12	3.5	2	2,145

*: spectral width parameter.

**: duration of experimental phase.

The profile of cross-shore sediment flux during offshore bar generation (Figure 2.3a) indicates that the offshore bar was formed by the offshore movement of sediment in the surf zone, with little input from sediment in the shoaling region, at $X \approx 55$ m. Offshore sediment flux was greatest near the trough of the bar, and the point of flux convergence ($Q = 0$) was offshore of the crest: the bar grew mostly from the offshore movement of

sediment coming from the trough region. During this first phase of bed evolution, average sediment flux $\bar{q} \approx 2.510^{-4} m^2/s$.

As the offshore bar was forming, the maximum wave height measured by wave gages moved slightly offshore but remained near the final position of the bar crest, at $X \approx 60$ m (Figure 2.4). Values of maximum measured wave height increased by approximately 2 cm between Run 1 and Run 14, which indicates that waves were affected by the bathymetric changes. During this period, the amount of low-frequency energy increased steadily in the flume up until the breakpoint ($X \approx 60$ m). Past the breakpoint, low-frequency and wave energy were of similar magnitude.

The effect of bathymetric change on the wave field is not reflected in the profiles of percent wave breaking. Percent wave breaking remained fairly stable, with approximately 6% of the waves broken at the breakpoint, and approximately 40% of the waves breaking between bar crest and trough. Past the trough of bar O, waves continued to break at a slower rate.

Figure 2.5 shows profiles of velocity moments during offshore bar generation. For cart instruments, error bars represent $\pm$ 1 standard deviation around the mean of all moments measured during a particular run, from 1 cmab to 25 cmab. For wall-mounted instruments, they represent $\pm$ 1 standard deviation around the mean of all moments measured during the whole phase of bed evolution considered. Because we measured velocity signals mostly in the lower portion of the water column, we do not present depth-averaged values of the moments, but rather their mean values.

In the shoaling region, between $X \approx 53$ and 58 m, undertow increased modestly from approximately 0.025 to 0.06 m/s (Figure 2.5, column 'OG'). On the other hand, waves became more nonlinear, as demonstrated by the profiles of velocity skewness and asymmetry, which increased relatively rapidly to approximately 0.4. This difference might explain

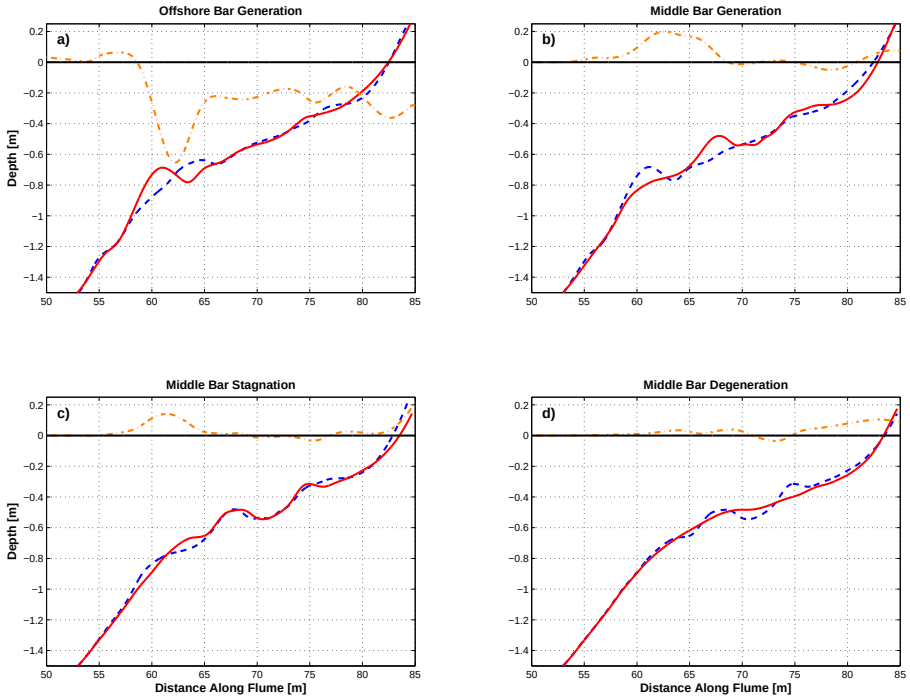

Fig. 2.3: Bed evolution stages and sediment flux during: (a) Offshore Bar generation; (b) Offshore Bar degeneration and Middle Bar generation; (c) Middle Bar stagnation, and (d) degeneration of all bedforms. Orange profiles, centered around the origin, show cross-shore variation of total sediment flux Q. Red solid line and blue dashed lines represent bathymetry measured at the beginning and end of each phase of bed evolution, respectively (Table 2.2).

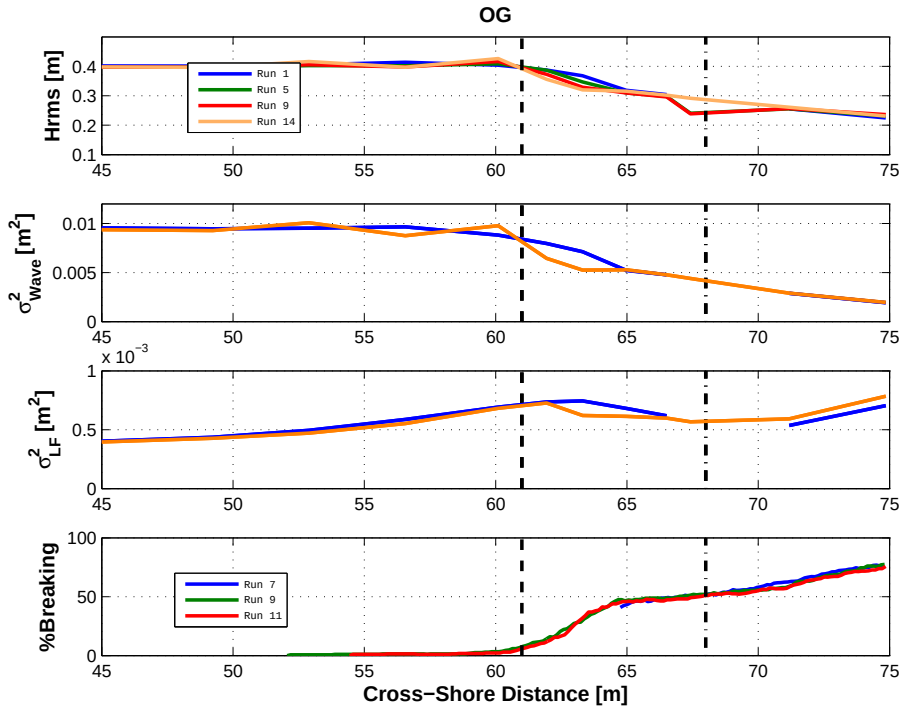

Fig. 2.4: Wave field during offshore bar generation. Top panel: rms wave height, H_{rms}. Second panel: variance at the wave frequency, σ^2_{Wave}. Third panel: variance in the low frequency range, σ^2_{LF}. Fourth panel: percent wave breaking. Dashed and dashed dotted lines represent average location of offshore and middle bars crest, respectively.

the shoreward movement of sediment observed in this region. At the breakpoint, the undertow current increased sharply, and peaked at 0.2 m/s shoreward of the breakpoint, at the trough of bar O. This profile is characteristic of undertow currents generated by the breaking of relatively high waves, and was also observed in the field (see, e.g., Gallagher *et al.* (1998); Garcez-Faria *et al.* (2000)). This region also corresponds to the section of the flume that experienced the most offshore directed sediment transport (see Figure 2.3a between $X \approx 61m$). In contrast, wave asymmetry and skewness increased slightly to approximately 0.5 at the trough of bar O.

In the surf zone, undertow strength steadily decreased to 0.1 m/s near the shoreline (Figure 2.5). Velocity skewness and asymmetry increased only modestly to approximately 0.55. This suggests that, even though waves were breaking intensely over the bar (40% of the waves were broken in the trough), they maintained a fairly constant shape in the surf zone. The relatively low level of nonlinearity, compared to the strength of the undertow, indicates that undertow was the dominant factor responsible for the offshore-directed sediment transport in this region.

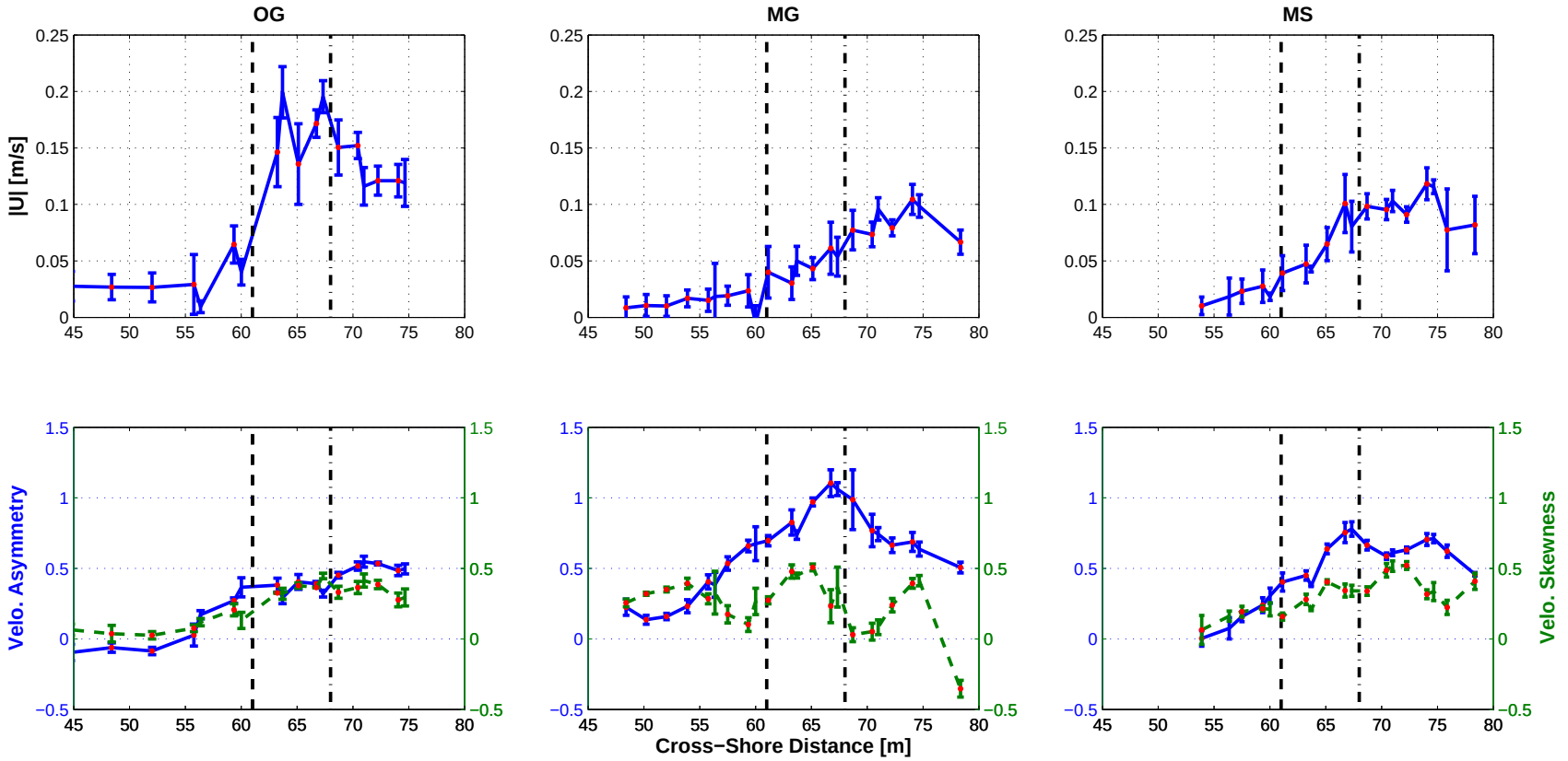

Fig. 2.5: Profiles of velocity moments during various phases of bed evolution. Profiles of undertow (top row), acceleration skewness (blue lines, second row), and velocity skewness (green lines, second row) during offshore bar generation ('OG', left panels), middle bar generation ('MG', center panels) and middle bar stagnation ('MS', right panels), as measured by wall and cart (red dots) instruments. Error bars represent standard deviation around the mean. Vertical dashed and dashed dotted lines represent average location of offshore and middle bars, respectively.

We modeled wave height, mean water level and depth-averaged mean current in the flume for Runs 1, 6 and 14 in order to quantify the relative importance of bed change on the undertow. The model of Baldock *et al.* (1998) reproduced quite well the profiles of measured H_{rms} and $\bar{\eta}$ in the flume (see Figure 2.6). Profiles of depth-averaged return current, U_r, indicate that, as the bar was forming and bar O was migrating offshore, maximum of U_r also moved offshore by approximately 1 to 2 m. The comparison of the profiles of U_r with the profile of mean undertow values presented in Figure 2.6 shows that, although mean currents were affected by bathymetric changes, profiles of measured mean undertow are quite representative of the overall shape and strength of the undertow during the entire phase of offshore bar generation.

Finally, analysis of the temporal evolution of the offshore bar (Figure 2.7) shows that this bar started to form shortly after the beginning of the experiment at $X \approx 65\,m$. This position also corresponds to the offshore slope break in the initial profile (see Figure 2.3a). After an initial offshore retreat without much change in height, the bar started to grow, and moved offshore at approximately 1 cm/min. This growth stopped when wave conditions changed, at around 900 minutes.

In summary, a sandbar was formed during the first 14 runs of our experiment. The sand bar formed at or near the breakpoint by the offshore movement of sediment coming principally from the surf zone. Undertow was strong at the breakpoint and in the surf zone, whereas velocity asymmetry and skewness were relatively constant in this region. Both waves and undertow profiles were affected by the bathymetric evolution. However, modeled cross-shore profiles of U_r are quite similar to each other, and within the range of measured undertow. In addition, error bars around the profiles of velocity skewness and asymmetry are relatively small. Thus, we will assume that wave and velocity moments, measured during the generation of bar O, are representative of the whole phase.

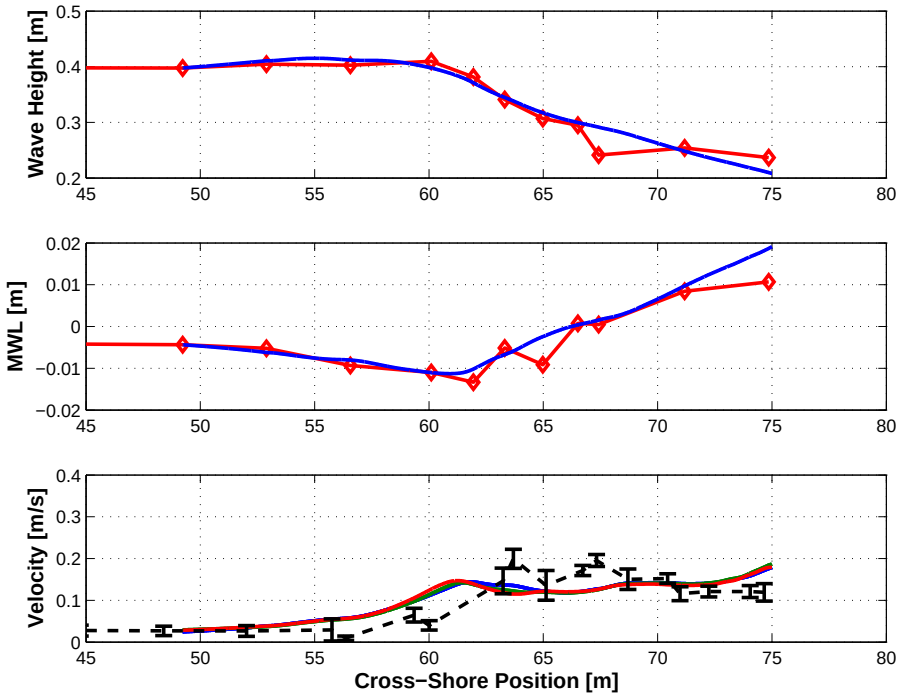

Fig. 2.6: Modeled depth-averaged undertow. Top and second panels: measured (red solid line with diamonds) versus modeled (blue line) rms wave height, and MWL $\overline{\eta}$ at the beginning of offshore bar generation, Run 1. Bottom panel: modeled depth-averaged mean current at the beginning (blue line), middle (green line) and end (red line) of offshore bar generation. Black dashed line represents profile of mean undertow measured during generation of offshore bar (see Figure 2.5).

2.3.2 Bed, Waves and Velocity Moment Evolution during Middle Bar Generation

Following the offshore bar generation period, we simulated summer fair-weather conditions, using reduced wave heights and increased wave periods (Table 2.2, Figure 2.7). From Runs 15 to 45 (time 210 to 720 min in Figure 2.7), rms wave height at the wavemaker was set at 0.21 m, and from Runs 46 to 56 (wave time 720 to 885 min.) rms wave height was set at 0.23 m. As a result, between Runs 15 and 56, the bar O degenerated, and a middle bar formed at $X \approx 68m$ (Figure 2.3b). We also observed the presence of small asymmetric ripples, 0.5-2.5 cm high and 5-10 cm long, in most areas of the flume. These ripples were variable in shape in the alongshore direction, but did not seem to migrate during the experiment. We will refer to this period of bed evolution as the middle bar generation phase ('MG' in the figures), and we will refer to the middle bar as bar M.

The sediment flux profile during this period (Figure 2.3b), indicates that the middle bar was formed principally by the shoreward movement of sediments originating from the offshore bar. Sediment also moved offshore between $X \approx 75$ and 80 m, forming a slope break at $X \approx 74m$. The average sediment flux value $\overline{q}$ for the middle bar was a quarter the size of the value obtained during offshore bar generation. This indicates that sediment moved more slowly than during offshore bar generation.

At the beginning of the bar M generation period (Runs 14 and 15), waves stopped shoaling when they reached the bar O. H_{rms} and H_{rms}/h are approximately constant at $X \approx 60$ m (Figure 2.8). However, they did not break. Past the offshore bar, waves shoaled again until they reached the new breakpoint, located at $X \approx 67$ m. During Runs 20 to 56, wave height decreased while waves were traveling over the degenerating bar O. Between $X \approx 56\,m$ and $X \approx 62\,m$, wave height decreased by approximately 0.3 m. This decrease in wave height, as waves proceeded over bar O, suggests breaking. However, profiles of breaking ratio indicate that waves started to break at X $\approx$ 63 m, shoreward of bar O.

Additionally, as bar O was degenerating and moving shoreward, values of H_{rms} steadily decreased at $X \approx 60\,m$, from 0.28 m during Run 15, to 0.25 m during Run 45 (Figure 2.8). After H_o was increased to 0.23 m, rms wave height remained at approximately 0.27 m at that location. In contrast, wave height increased from 0.27 to 0.28 m at the breakpoint between Runs 15 and 45, and from 0.28 to 0.29 m between Runs 46 and 56.

The breakpoint was fairly stable during bar M generation. From wave gage observations, the breakpoint was at $X \approx 66.5\,m$ during Run 15, moving slightly shoreward to $X \approx 67.4\,m$ during Run 45. After wave height was increased to 0.23 m, the breakpoint moved offshore by 1 m, and remained at the same position until the end of the generation phase of bar M, or Run 56. As was observed during offshore bar generation, the breakpoint during the generation of the middle bar is located slightly offshore of the final location of the middle bar. Additionally, percent of wave breaking, increased while the bar M was growing (Figure 2.8). While the percent of waves breaking at the breakpoint increased modestly from 14% to 18%, the percent of wave breaking in the trough of bar M increased from approximately 20% at Run 16 to 40% at Run 47. This is different from the bar O generation phase, where percent of wave breaking in the bar trough was higher, but remained fairly constant from one Run to another. Finally, comparing profiles σ^2_{Wave} between Runs 15 and 41 shows that energy was highest near the offshore bar O ($X \approx 60$ m) during Run 15, whereas energy highest near the middle bar M ($X \approx 65$ m) during Run 41. However, during both runs, low-frequency energy remained relatively low until waves reached the offshore bar location.

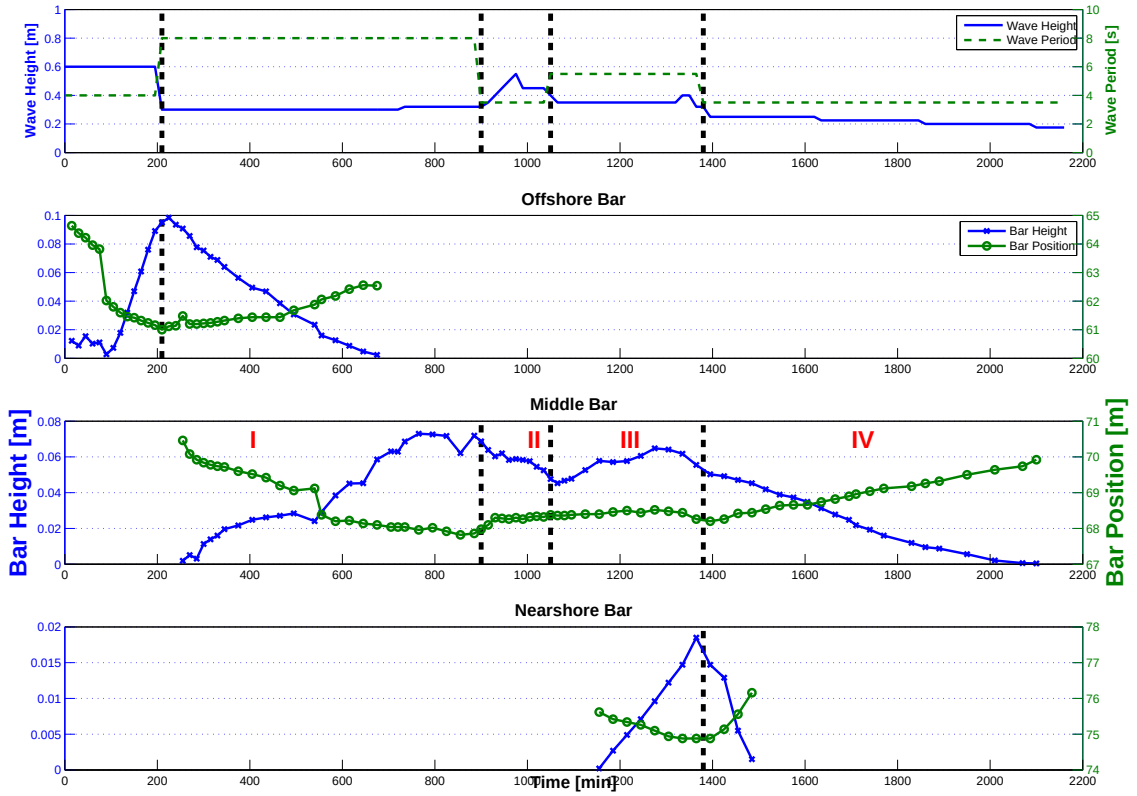

Fig. 2.7: Time Evolution of bars characteristics. Wave height and period changes (top subplot), and spatial and temporal evolution of offshore (second subplot), middle (third subplot) and nearshore (bottom subplot) bars during the experiment. Dashed vertical lines indicate time when wave period was changed, and grossly correspond to the different stages of bed evolution, and phases (red roman numbers) of middle bar life cycle.

The middle bar formed at or near the breakpoint, which is similar to the offshore bar case. However, waves and percent wave breaking were lower than during offshore bar generation, and sediment moved shoreward to form the bar. We computed profiles of velocity moments to assess the relative amount and importance of nonlinearity in the flume. Because we visited a particular location in the flume more than once, error bars around mean values are indicative of temporal changes in the value of the moments.

Figure 2.5 shows that undertow is lower compared to the offshore bar generation phase, and did not reach a maximum over bar M. Despite the increase in percent wave breaking that occurred as bar M formed, mean undertow at a fixed cross-shore location was fairly constant, as indicated by the small error bars. To better assess the temporal evolution of mean currents, we modeled wave height and MWL in the flume between Runs 15 and 45, during which H_o was similar.

Figure 2.9 shows profiles of modeled and observed H_{rms} and $\bar{\eta}$ for Run 45. Contrary to the offshore bar generation case, the wave model does not predict the observed wave height profile as well as during offshore bar generation. In particular, the model did not predict very well the shoaling and stagnation/decrease of wave height over the offshore bar, at $X \approx 60\,m$. Similarly, the model does not reproduce the observed variations in $\bar{\eta}$. We do not think that this is due to the choice of wave dissipation model (Baldock *et al.* (1998)) because waves were not breaking in that location. Rather, our choice of a model based on LWT, which excludes non-linear effect, could account for the poor reproduction of shoaling at $X \approx 60\,m$. Nonetheless, the model predicts an average undertow of similar magnitude to our measurement, demonstrating that undertow is weaker during middle bar generation than during offshore bar generation.

As mentioned earlier, we had difficulties in modeling the measured profiles of wave height. This is likely due to the fact that waves exhibited a fair amount of nonlinearity. Profiles of velocity asymmetry and skewness show that waves were originally fairly skewed

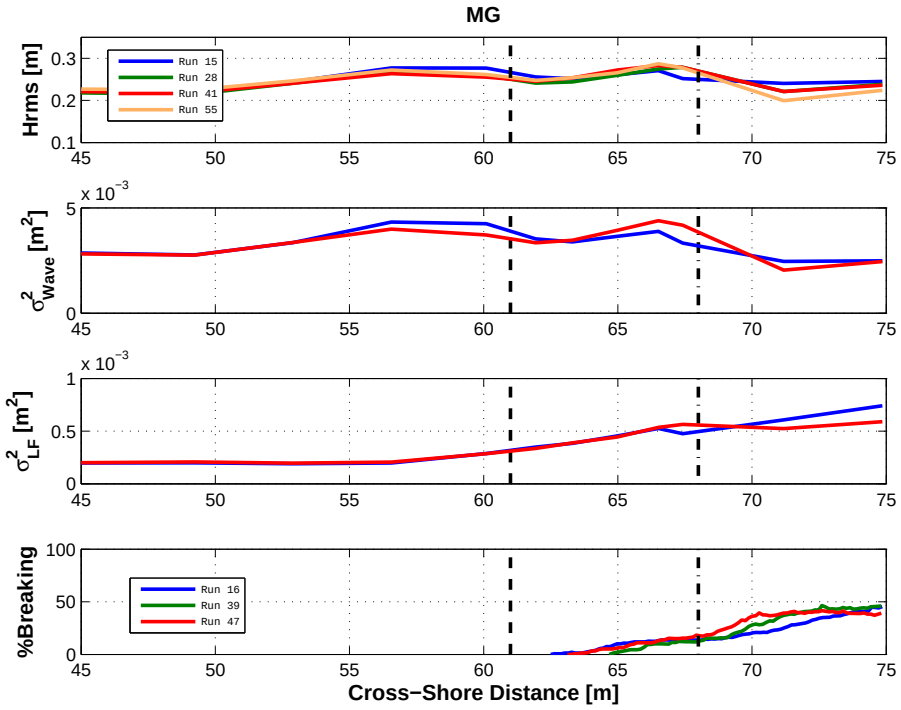

Fig. 2.8: Wave field during middle bar generation. Top panel: rms wave height, H_{rms}. Second panel: variance at the wave frequency, σ^2_{Wave}. Third panel: variance in the low frequency range, σ^2_{LF}. Fourth panel: percent wave breaking. Dashed and dashed dotted lines represent average location of offshore and middle bars crest, respectively.

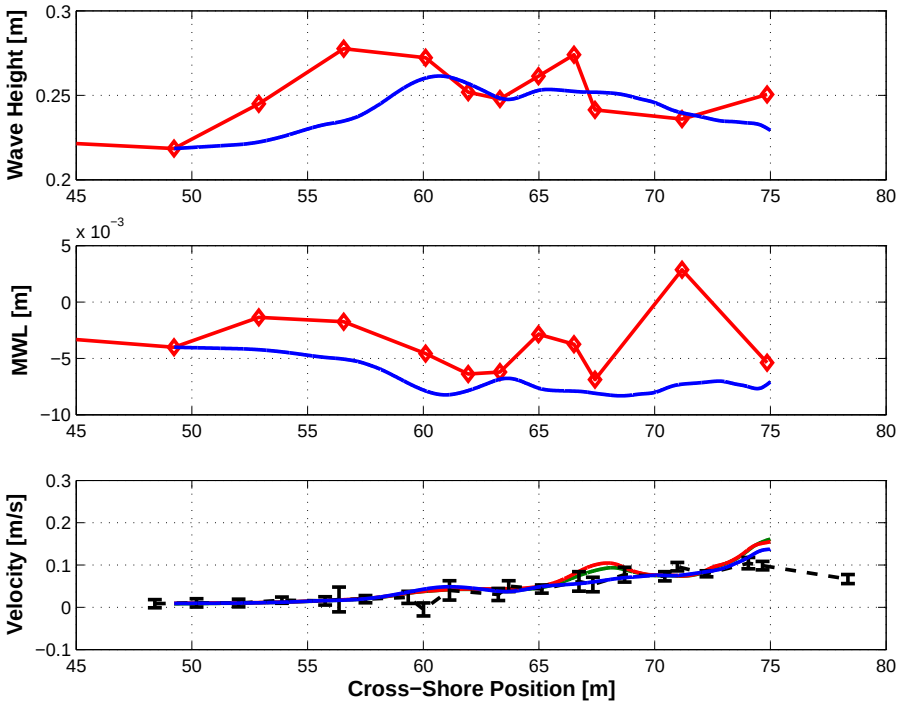

Fig. 2.9: Modeled depth-averaged undertow during middle bar generation. Top and second panels: measured (red solid line with diamonds) versus modeled (blue line) rms wave height, and MWL $\overline{\eta}$ at the beginning of middle bar generation, Run 15. Bottom panel: modeled depth-averaged mean current at the beginning (blue line), middle (green line) and end (red line) of middle bar generation. Black dashed line represents profile of mean undertow measured during middle bar generation (see Figure 2.5).

at X $\approx$ 50 m, and became more asymmetrical ('sawtoothed') as they shoaled in the flume (Figure 2.5). Velocity asymmetry peaked slightly offshore of the middle bar crest, at or near the breakpoint. At the breakpoint of the middle bar, velocity asymmetry is twice as high as it was during offshore bar generation. As waves propagated in the surf zone, velocity asymmetry decreased steadily to reach a minimum close to the shoreline. Velocity skewness, on the other hand, increased over much of the surf zone width, but had values of approximately half of the velocity asymmetry. The spatial evolution of velocity asymmetry and skewness illustrates the complex changes in wave shape, as waves were almost breaking on top of the offshore bar, and broke on top, and past, the middle bar.

The comparison between profiles of velocity moments (Figure 2.5) and of total sediment flux during the generation of the middle bar (Figure 2.3) shows that the maximum gradient in velocity asymmetry was reached in the region of the flume where sediment was being transported shoreward, between $X \approx 60$ and 68 m. Alternatively, in the surf zone ($X > 68\,m$), undertow steadily increased from 0 to approximately 0.5 m/s and velocity asymmetry decreased, but overall shoreward movement of sediment decreased, and/or stopped.

Analysis of the temporal evolution of the offshore and middle bars (Figure 2.7) indicates that when wave conditions changed at around 210 minutes (Run 14), the offshore bar started to degenerate: its height decreased while it slowly moved shoreward at an approximate speed of 0.3 cm/min. Simultaneously, the middle bar began forming and was moving offshore at approximately the same speed of 0.3 cm/min (Figure 2.7, Phase I). Once the offshore bar disappeared, the growth of the middle bar plateaued, until wave conditions changed. These observations indicate that the middle bar grew with sediment originating from the offshore bar.

In summary, the middle bar was formed at or near the breakpoint. However, waves had a relatively higher level of nonlinearity compared to the previous phase of bed evolution.

Undertow was approximately 6/10 of the value it had during offshore bar generation, but wave asymmetry was twice as high. The highest gradient in wave asymmetry was observed in the region of highest total transport. These observations suggests that forcing induced by wave orbital velocity was the primary factor in the formation of the middle bar. Finally, although the modeling of the waves does not have the same accuracy as during offshore migration, we found that profiles of mean return current were slightly affected by bed changes. However, overall shape and values of modeled undertow are similar to the observed values mean current. Further, error bars around velocity asymmetry and skewness are relatively low. Hence, we will once again assume that the whole phase can be described by wave heights and velocity moments measured during the various runs during this phase of bed evolution.

2.3.3 Bed, Waves and Velocity Moment Evolution during Middle Bar Stagnation

Once the middle bar formed, we subjected it to waves with varying heights and periods, from Run 57 to 89 (Table 2.2). As a result, the middle bar remained at the same position, but other minor changes in the profile occurred. Some sand accumulated in the trough of bar M, and a nearshore terrace, or nearshore bar, was generated at $X \approx 74$ m. The slope break located at the edge of the active profile region in the shoaling zone (at $X \approx 60\,m$) moved shoreward by approximately three meters (Figure 2.3c).

Although bar M remained at approximately the same position, its geometry changed markedly (Figure 2.7). After an increase in wave height and decrease in wave period (Table 2.2), the middle bar's height decreased by approximately 2 cm (Figure 2.7, Phase II). Conversely, it increased by approximately 2 cm after wave height was reduced and wave period increased (Phase III). Finally, we also tracked the movement of the nearshore terrace. It grew during Phase III and moved offshore during its generation. Only Phase III of the bed evolution phase will be analyzed in this paper because it experienced constant

wave height (Runs 69 to 86, wave time 1065 to 1335). We will refer to this period as the middle bar stagnation period ('MS' in the Figures).

The cross-shore profile of sediment flux during middle bar stagnation (Figure 2.3c) indicates that, as observed during the generation phase, most of the transport was directed shoreward. Rather than contribute to the growth of bar M, this shoreward transport resulted in shoreward movement of the slope break. Comparatively, a small amount of net offshore transport occurred shoreward of the middle bar. Average sediment flux value $\overline{q}$ was approximately 45 % smaller than during bar M generation.

When the middle bar remained constant, waves experienced minimal changes as they propagated over the offshore slope break, which replaced the offshore bar (Figure 2.10). We only noticed a slight increase in wave height of approximately 2 cm just before the slope break, and a slight decrease of the same amount just after the slope break. The breakpoint remained at the same position ($X \approx 68\,m$), and the maximum H_{rms} value experienced small changes. Finally, waves profiles are nearly identical among the various runs conducted during this phase of bed evolution. The only exception is Run 85, during which wave height near the breakpoint, $X \approx 67$ m decreased by less than 1 cm, compared to the previous runs. Similarly, profiles of σ_{Wave} and σ_{LF} show that bathymetric changes were limited: the amount of energy at the peak wave frequency is similar between Runs 15 and 45. However, we notice a decrease in peak low-frequency energy for Run 86 of approximately 38% compared to Run 69.

The middle bar triggered more wave breaking than during the previous bed evolution phases: 20% of the waves broke over the bar during middle bar stagnation, versus approximately 15% during middle bar generation and 8% during offshore bar generation. Also, almost 60% of the waves were broken shoreward of the trough, compared to 50% during middle bar generation, and approximately 40% during offshore bar generation. However, similar to the middle bar generation period, and unlike the offshore bar generation

period, percent wave breaking values plateaued in the surf zone, past the middle bar crest.

Measured undertow steadily increased from 0 near the wavemaker to approximately 0.1 m/s offshore of the breakpoint, at $X \approx 68$ m (Figure 2.5). It stagnated in the surf zone, before decreasing by approximately 25% closer to the shoreline. Offshore of the breakpoint, undertow was approximately twice as strong during stagnation of bar M than during its generation, but it was 50% weaker than during offshore bar generation.

Modeling results of wave height and depth-averaged mean currents are presented in Figure 2.11, and our estimates of U_r indicate that undertow was fairly stable during the various runs during which bar M stagnated. This confirms that the wave field did not vary much during this portion of the experiment. In addition, modeled profiles of U_r are within the range of values measured, and they exhibit a similar behavior to observed values of mean undertow: they peak over the middle bar, and reach a local minimum at the trough of bar M.

While undertow was stronger during the stagnation of bar M, compared to during its generation, velocity asymmetry, on the other hand, was weaker by approximately 20% (Figure 2.5). The profile of velocity asymmetry showed similar characteristics as during the middle bar generation: it steadily increased as waves shoaled, and decreased past the breakpoint, with a slight increase over the nearshore terrace. Interestingly, shoreward sediment flux reached a maximum at approximately the same location where velocity asymmetry peaked. Velocity skewness also increased steadily towards the shore, despite a minimal decrease at the breakpoint, and did not peak until waves were slightly offshore of the nearshore terrace.

In spite of the differences between middle bar generation and stagnation cases, profiles of total sediment transport exhibited the same overall characteristics. Specifically, sediments from shoaling regions moved shoreward and sediment in the surf zone region

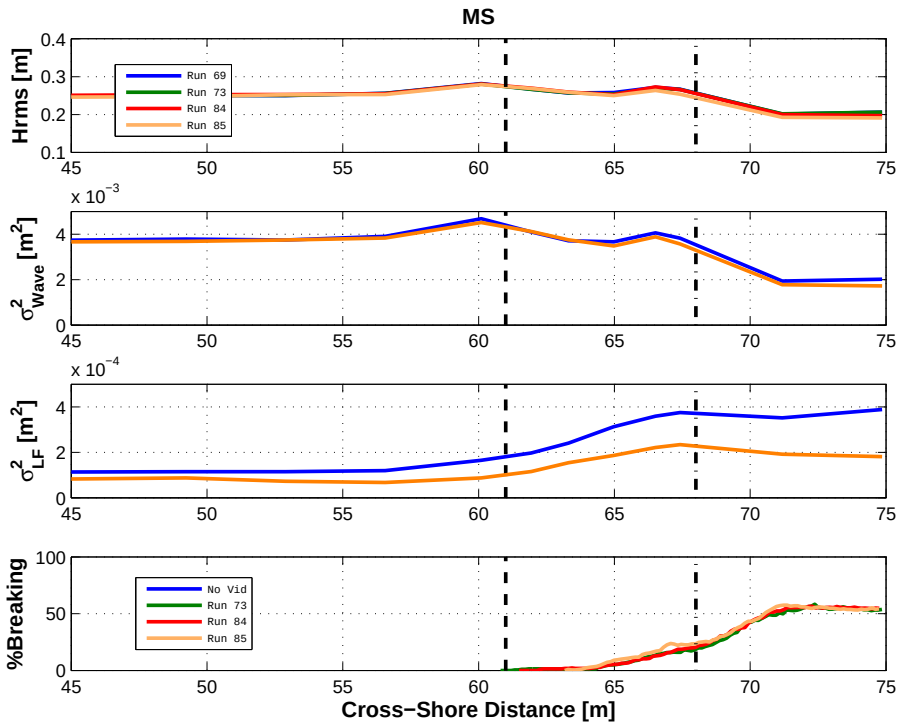

Fig. 2.10: Plots of rms wave height (H_{rms}, top panel), variance at the wave frequency (σ^2_{Wave}, second panel), variance in the low frequency range (σ^2_{LF}, third panel), and percent wave breaking (bottom panel) during middle bar generation. Dashed and dashed dotted lines represent average location of offshore and middle bars crest, respectively.

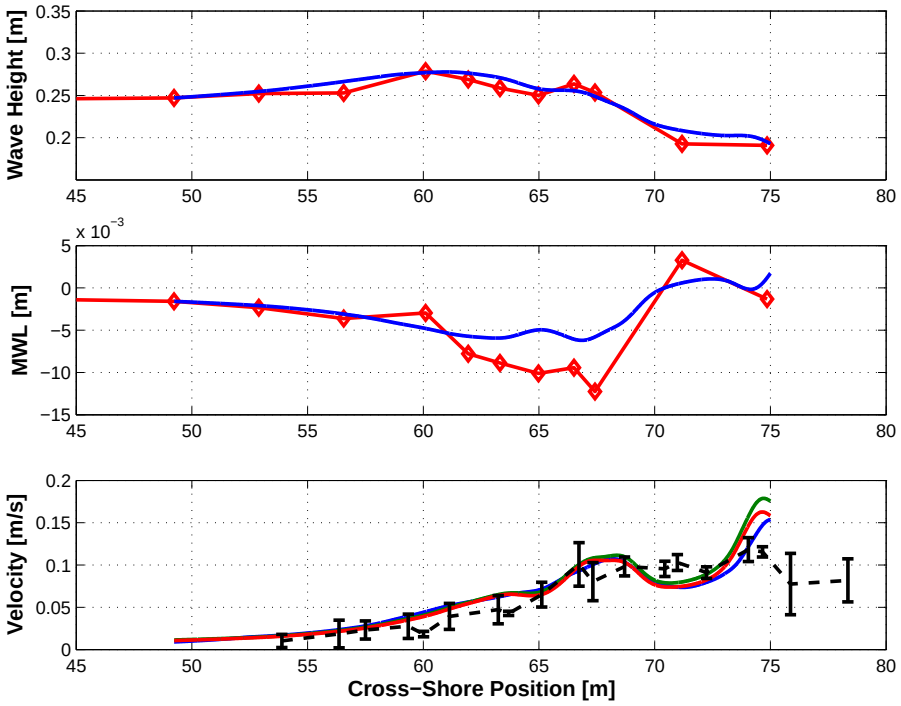

Fig. 2.11: Modeled depth-averaged undertow. Top and second panels: measured (red solid line with diamonds) versus modeled (blue line) rms wave height, and MWL $\overline{\eta}$ at the beginning of middle bar stagnation phase, Run 69. Bottom panel: modeled depth-averaged mean current at the beginning (blue line), middle (green line) and end (red line) of middle bar stagnation. Black dashed line represents profile of mean undertow measured during middle bar stagnation (see Figure 2.5).

moved moderately in both directions. However, we can hypothesize that a stronger undertow, and a weaker velocity asymmetry, resulted in less shoreward sediment transport offshore of the middle bar than during middle bar generation. In particular, total sediment flux was almost null at $X \approx 67$ m (see Figure 2.3), when a fair amount of sediment was moving shoreward in the same region during middle bar generation. The difference between the two phases was that velocity asymmetry is weaker, and undertow stronger at this cross-shore location during middle bar stagnation compared to middle bar generation.

2.3.4 Bed, Waves and Velocity Moment Evolution during Middle Bar Degeneration

At the end of the experiment, during Runs 90 to 141 (a total of 1,350 minutes of waves), we progressively reduced wave height and period, which generated an approximately monotonic beach profile (Figure 2.3d). This period, which will we refer to as the middle bar degeneration period, was characterized by the shoreward movement of sediments in the shoaling region up to the trough of the middle bar, while sediment from the nearshore terrace moved in both directions. Cross-shore sediment flux average magnitude $\overline{q}$ was approximately 60 % smaller than during middle bar generation.

Analysis of the temporal evolution of the bar (Figure 2.7, Phase IV) shows that during the last 52 runs, the middle bar decreased in height as it moved shoreward and disappeared at the end of the experiment. It moved shoreward at a speed of approximately 0.1 cm/min. This onshore migration speed is much slower than the offshore bar's speed (0.3 cm/min); this difference in speed is in line with previous field observations (see e.g., Lippmann & Holman (1990)). Finally, the nearshore terrace, which grew during Phase III, moved offshore during its generation, and degenerated rapidly during Phase IV while moving shoreward. We will not analyze this period further in the remainder of this paper.

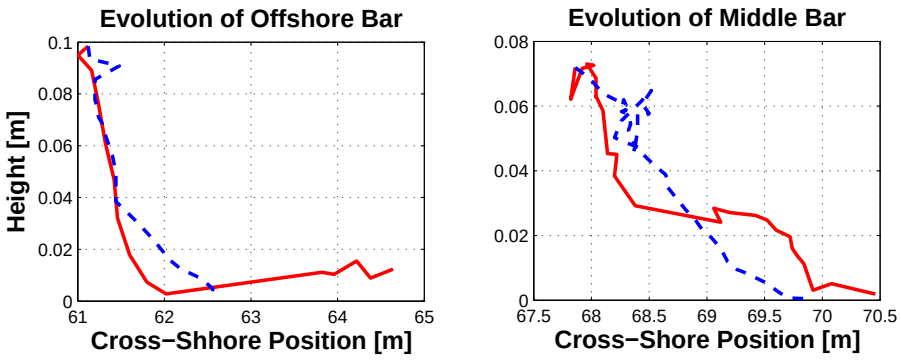

Fig. 2.12: Offshore and middle bars height versus position during their life cycle. Solid red line and dashed blue line represent bar height and position during bar generation and degeneration, respectively.

2.3.5 Summary

In summary, we observed four stages of bed evolution during the course of the experiment: (1) rapid generation of the offshore bar, (2) slow degeneration of the offshore bar and growth of a middle bar, and generation of a nearshore terrace, and (4) slower degeneration of the middle bar and the nearshore terrace, and smoothing of the bed profile. Offshore sediment movement occurred principally in the surf zone, while most shoreward movement took place in the shoaling region. This is consistent with previous laboratory and field experiments (Shepard (1950); Komar (1998); Gallagher *et al.* (1998)).

We observed that when the bars were being generated, they became taller and widened as they moved offshore. On the other hand, the bars decreased in height and became narrower as they moved shoreward during their degeneration period. This behavior has been observed on natural beaches (Ruessink *et al.* (2003b); Plant *et al.* (2001)). We can summarize their evolution by plotting bar height versus position (see Figure 2.12). The relationships between these two parameters varied with each bar and during each bar evolution. Remarkably, however, the location of bar genesis (defined as the point where they rapidly start moving offshore) and demise (when they can no longer be identified as a bar with a distinct trough) are similar for each bar.

Additionally, a few points can be drawn from the simple analysis of hydrodynamics presented in this section:

1. For both offshore and middle bar generation, the final position of the bars ended up being close to the breakpoint. Sediment that contributed to the growth of the offshore bar came from surf zone regions, while sediment that contributed to the growth of the middle bar came from offshore regions.

2. Waves and mean current were affected by bed changes. However, profiles of depth-averaged velocity are similar to the average measured values, and error bars around measurements are relatively low. Consequently, we will assume in the modeling section that velocity moment profiles presented in Figure 2.5 are representative of their values during a whole phase of bed evolution.

3. Contrary to offshore bar generation, during middle bar generation and stagnation waves were highly nonlinear and not of permanent shape. Gradients in velocity asymmetry were opposite in surf zone regions than in offshore regions, which indicates that waves were less non-linear past the breakpoint.

4. Total sediment flux at a particular location was the result of the local balance between forcing generated by, at least, two velocity moments: undertow and velocity asymmetry. The role of velocity skewness remains unclear. When undertow is weak and wave asymmetry is large (as in the shoaling region during the generation of bars O and M), sediment moves predominantly shoreward. When undertow is strong and the wave asymmetry is weak (as in the surf zone during the generation of bars O and M), sediment moves predominantly offshore. The delicate local balance between wave nonlinearity and undertow is also illustrated during the stagnation of bar M. During this period, undertow was slightly larger than during generation of bar M, while velocity asymmetry was slightly weaker, and there was weaker shoreward transport.

In the remainder of this paper, we will concentrate on the offshore bar generation and phase I (generation) and phase III (stagnation) of the middle bar. Wave conditions during

Phase II and IV of the middle bar life cycle varied too extensively to apply the same analyses. Finally, we will not analyze the dynamics and life cycle of the observed mega-ripples or the generation of the nearshore terrace because observations at the required spatial scale were not collected.

2.4 Sediment Transport Observations

Sediment transport is the sum of suspended and bedload sediment fluxes. Consequently, in order to evaluate the performance of transport models, it is important to compare their effectiveness at reproducing the overall observed sediment flux (Section 2.3). It is also important to evaluate whether the models reproduce the observed balance between suspended and bedload transport during various phases of bed evolution.

In this section, we analyze the records from the FOBS in order to assess the amount of sediment that was put into suspension in the flume. We will compute the strength of suspended transport during each run, and we will identify the relative role of the wave, low-frequency and mean motions in moving the suspended sediment. Furthermore, because we did not directly measure bed transport, we indirectly deduce its importance from the total observed sediment fluxes.

2.4.1 Mean Sediment Concentration

During each run, we measured sediment concentration from -1.2 to 41.5 cmab. Probes above 17 cmab were often polluted by bubbles, and we excluded them from our analysis. During the generation of bar O, mean sediment concentration values were similar among the four lowermost sensors. Maximum sediment concentration was highest in the trough of the offshore bar ($X \approx 62$ m), where total sediment flux was maximum (see Section 2.3). Mean sediment concentration decreased from -1.2 to 1.2 cmab, and in general, concentration at 0.8 cmab was approximately 50% lower than at -1.2 cm. This indicates that the

energetic wave conditions present during offshore bar generation, activated sediment well below the initial bed level.

During generation and stagnation of bar M, sediment sensors that were buried in the initial bed level often exhibited concentration levels that were either consistently higher than 100 kg/m^3 or, when conditions were more energetic, they exhibited concentration peaks greater than 100 kg/m^3. This would indicate that either sediment is not in suspension (Ribberink & Al-Salem (1995); Dohmen-Janssen & Hanes (2002)), or that sediment was mobilized for initiation of suspension (Conley & Beach (2003)). This also suggests that, during middle bar generation and degeneration, depth of sediment activation was shallower. Previous experiments have shown that the thickness of the bed mobile layer varies with velocity (e.g., Ribberink & Al-Salem (1995); Dohmen-Janssen *et al.* (2002)).

Highest sediment concentrations were measured between 0.8 and 2 cmab. Above 5 cmab, mean sediment concentration profiles were fairly uniform. This suggests that sand was well-mixed in the water column, and there was little contamination of the signal by horizontal advection of plumes at discrete elevations in the water column. This also suggests that, although time series were not repeatable at a particular cross-section, similarities existed between them in the way sediment was diffused/advected upwards. In the remainder of this paper, we will assume that sediment at or above 0.8 cmab was transported through suspended load.

We compared suspended load among the major phases of bar evolution. To represent the cross-shore variation of suspended sediment concentration, we computed the amount of suspended load (mass of suspended sediment per unit area, Figure 2.13) from the depth integration of profiles of mean sediment concentration from 0.8 to 17 cmab. In Figure 2.13, error bars represent standard deviation around the mean, and indicate the variability of measurement between different runs at the same location. Time series of suspended sediment were not repeatable in the flume.

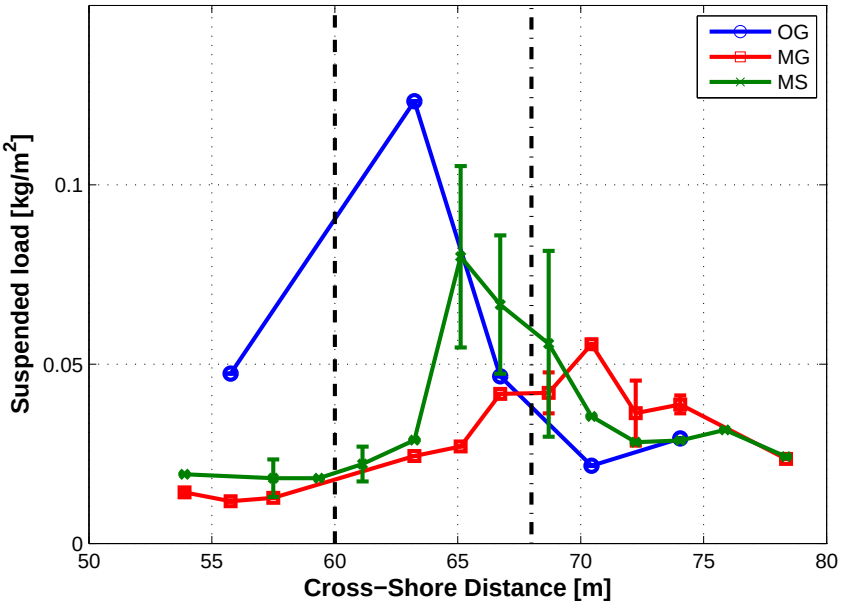

Fig. 2.13: Suspended load profiles. Suspended load measured during offshore bar generation ('OG'), middle bar generation ('MG') and middle bar stagnation ('MS'). Vertical dashed line represents breakpoint during offshore bar generation, and dashed-dotted line represents breakpoint during middle bar generation and stagnation.

During the generation of bar O, maximum suspended load was measured near the shoreward face of the bar at $X \approx 63$ m (Figure 2.13), where total sediment flux was highest (Figure 2.3). During the generation of bar M, suspended load steadily increased in the shoaling region, and peaked shoreward of the bar crest, at $X \approx 70$ m. Finally, during stagnation of bar M, suspended load sharply increased in the shoaling region of the waves to peak offshore of the crest of bar M, at $X \approx 65$ m. Suspended load steadily decreased in the surf zone. During both generation and stagnation of bar M, and contrary to the generation of bar O, suspended load peaked shoreward of the maximum in total sediment flux. In all cases, although maximum sediment concentration was measured between the bed and 5 cmab, less than 50% of the total load occurred in that region.

2.4.2 Frequency Decomposition of Suspended Sediment Transport

In order to elucidate the role of suspended sediment transport in total observed sediment flux, we computed suspended sediment flux by depth integrating the time-averaged value of the product of suspended sediment concentration and fluid velocity (Equation 2.4). We further decomposed this flux into contributions from the undertow (mean velocity), wave, and high and low-frequency fluctuations by separating velocity and sediment concentration values into frequency ranges, following Jaffe *et al.* (1984) and Hanes & Huntley (1986):

$$Q_s = \int_{z_1}^{z_2} \overline{CU} dz = \int_{z_1}^{z_2} \overline{CU} + \overline{C_L U_L} + \overline{C_W U_W} + \overline{C_H U_H}\, dz + \epsilon \tag{2.4}$$

where Q_s represents the suspended sediment flux, U and C represents the time series of velocity and sediment concentration, and overbars represent time averages. Subscripts L, W and H represent the low-, wave-, and high-frequencies components of the signal (frequency cutoffs of 0.1 Hz and $4.f_p$, where f_p represents the peak wave frequency). ϵ represents residual of that decomposition, and was found to be negligible after computation. Integration limit z_2 was taken at 17 cmab. The lower integration limit z_1 was taken at 0.8 cmab. Velocity signals U measured at 1, 5, 10, and 15 cmab were matched with sediment concentration signals C measured at 0.8, 5, 11 and 17 cmab. In instances where the ADV at 1 cmab or 15 cmab failed, the limits were changed to the elevation of the closest valid measurement. No flux was computed when the number of valid ADV measurements was less than three.

Results of the suspended sediment flux frequency decomposition are presented in Figures 2.14 and 2.15. During generation of bar O, suspended sediment flux in the flume contributed positively to the total sediment flux, i.e., sediment moved offshore in the water column, in the same direction as the total sediment flux (Figure 2.14). Most of the offshore advection of sediment is caused by the action of the undertow current; wave and low-frequency fluxes were low and balanced each other on average in the cross-shore direction as well as in the water column (Figure 2.15). At $X \approx 63.2\,m$, near the trough of

bar O, both waves and suspended fluxes were oriented offshore.

The ADV at 15 cmab failed when the cart was at station $X \approx 63m$ and $X \approx 66.73\,m$, where total sediment flux magnitude was highest. Hence, because mean sediment transport dominated the offshore suspended flux, it is likely our computation underestimates the relative importance of the suspended flux. Consequently, we revisited the estimate of Q_s for all cross-shore positions where measurements were available, by relying on the result that the undertow was responsible for most of the suspended sediment transport during offshore bar generation. In other words, we evaluated $Q_s \approx \int_{z_1}^{z_2} \overline{CU}$ between $z_1 = 0.8$ cmab and $z_2 = 17$ cmab.

We obtained profiles of $\overline{U}$ over a refined vertical grid (dz=0.5 cm) by fitting valid undertow measurements through a parabola. Profiles of suspended sediment concentration were also interpolated on the same refined grid. Results of the second estimate are presented in Figure 2.14, and they confirm that highest suspended sediment transport occurred in the bar region, where undertow was maximum. These results also indicate that suspended flux accounted for almost half of the total flux in the bar region, and for approximately one third of total flux in the surf zone. Offshore of the bar, suspended flux was negligible. From these observations, we infer that bedload (assumed to be the difference between total and suspended fluxes) contributed to a large portion of the offshore transport of sediment in the surf zone, as well as to the small shoreward flux of sediment offshore of the bar.

We repeated the same analysis for phases of middle bar generation and stagnation. In both cases, suspended flux negatively impacted the observed shoreward transport of sediment: suspended sediment was moving offshore, in the opposite direction of the total flux (Figure 2.14). During the generation of bar M, suspended transport profile peaks near the crest of the bar, at $X \approx 70\,m$, shoreward of total sediment flux maximum. Offshore, total suspended flux was small and did not influence the shoreward transport of sediment from bars O to M. In the surf zone suspended flux sometimes occurred in the opposite

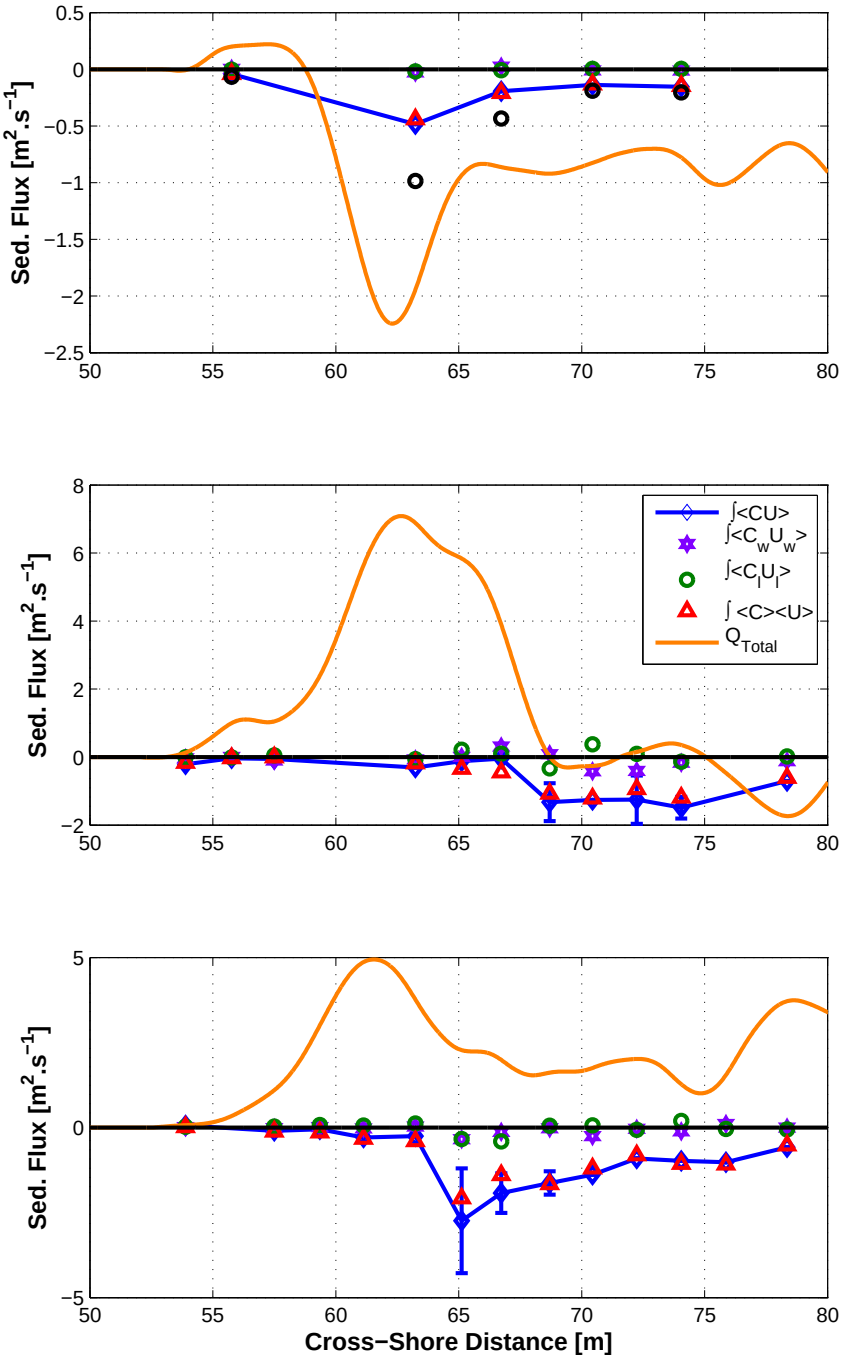

Fig. 2.14: Cross-shore decomposition of total sediment flux. Total measured flux Q_{Total} (orange curve), and suspended flux estimate (blue curve) during offshore bar generation (left panel), middle bar generation (middle panel) and degeneration (right panel). Suspended flux is decomposed in flux due to undertow (red triangles), due to waves (green circles), and low-frequency flows (purple stars). Black circles represent correction of flux due to undertow.

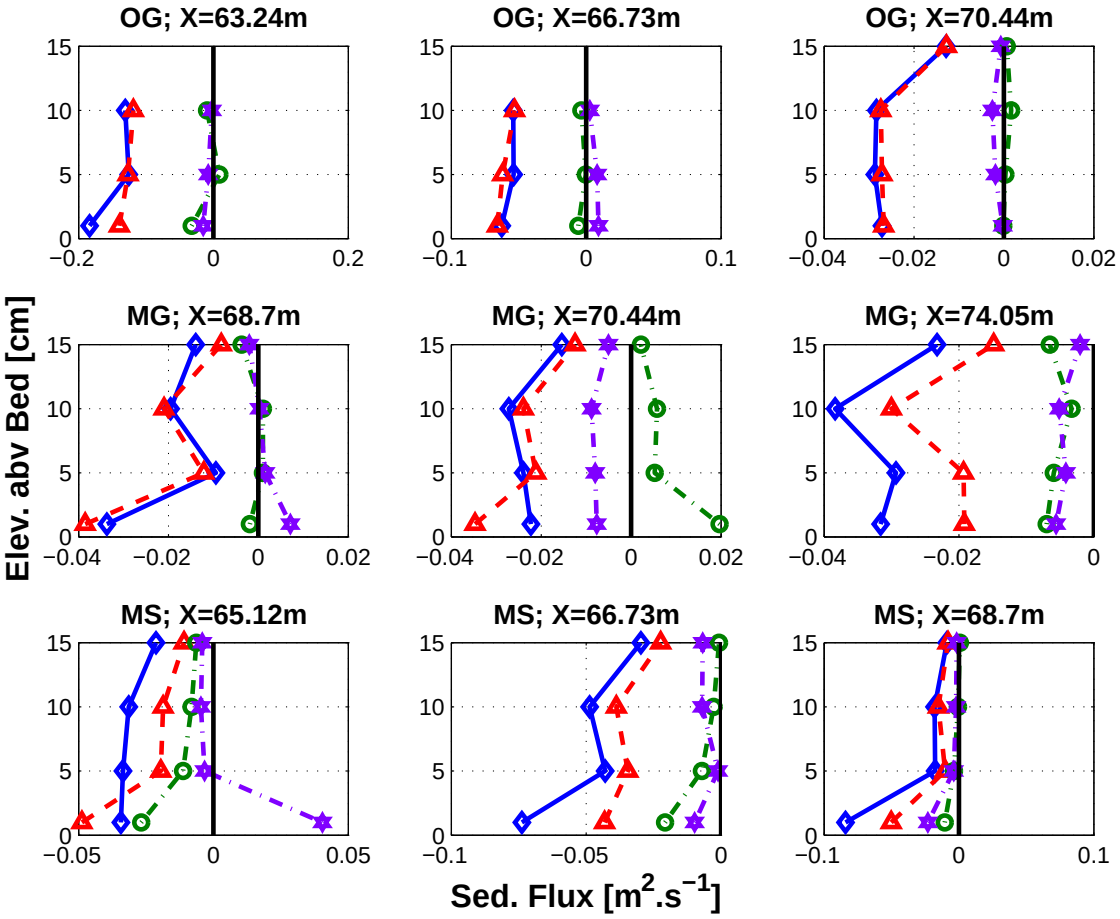

Fig. 2.15: Vertical decomposition of total suspended sediment flux. Decomposition of suspended flux into total flux (blue lines), flux due to undertow (red dashed lines), flux due to waves (green dashed lines) and flux due to low-frequency motions (purple dashed lines) at discrete elevations (symbols) above the bed. Measurements were made during offshore bar generation (top panels), middle bar generation (middle panels), and middle bar stagnation (bottom panels) at various cross-shore positions. During offshore bar generation, breakpoint was at $X \approx 61\,m$ and during middle bar generation and stagnation, breakpoint was at $X \approx 68\,m$.

direction of total transport ($X \approx 72\,m$). Throughout the water column, low-frequency and wave-induced transport were relatively weak, and compensated each other (Figures 2.15). Closer to the shoreline, at $X \approx 74\,m$, wave and low-frequency motions moved sediment offshore, and together they accounted for approximately 40% of the total transport.

Finally, during stagnation of bar M, suspended flux was oriented offshore, while observed total flux was oriented shoreward. Maximum suspended flux was observed offshore of the breakpoint, at $X \approx 65\,m$. This difference in position of maximum suspended flux, compared to the generation of bar M, might be due to the fact that undertow was stronger and velocity asymmetry was weaker offshore of the breakpoint during the stagnation of bar M that during its generation (see Section 2.3). Interestingly, low-frequency and wave fluxes were also oriented in the offshore direction. In the surf zone, past $X \approx 68\,m$ suspended flux as well as total flux decreased. Throughout the water column, wave and low-frequency fluxes were weak compared to the undertow-driven flux but they were oriented offshore (Figure 2.15), which is different from the previous two phases of bar evolution.

Frequency decomposition shows that, as was the case during offshore bar migration, most of the suspended sediment was advected by the undertow. Fluxes due to low- and wave-frequency components were small, and generally compensated each other in the water column (Figure 2.15). Assuming, once again, that the difference between total and measured suspended fluxes is due to bedload motion, most of the sediment that contributed to the middle bar growth, and to the offshore bar degeneration, moved shoreward as bedload. In the surf zone, the relative strength of the suspended transport points to an almost equal and opposite bedload. The first exception to this observation occurred closer to the shoreline, where all sediment was moving offshore.

In the absence of direct observations of bed load transport, we qualitatively evaluated whether our observations of bedload could be explained by sheet flow or ripple migration. We neglected plug flow, a third possible mechanism for bedload, because predictors pro-

posed by Zala Flores & Sleath (1998) and Foster *et al.* (2006) were well below threshold values for all wave conditions in the flume. To evaluate whether ripple migration might have explained the observed bedload, we estimated their migration speed. Based on the geometry of ripples observed between runs in the flume, we estimated a migration speed of 12 mm/s. This speed is at least one order of magnitude higher than typical speeds (Nielsen (1982)). On the other hand, we found that, for our dataset, values of predictors of sheet flow transport (Nielsen (1982); Soulsby (1997)) were often exceeded in the surf zone (i.e. $\theta \geq 0.8$). In the shoaling regions, where most bed load was observed, values were close to the threshold (i.e. $\theta \approx 0.6$). Consequently, it is likely that sediment moved as sheet flow. As explained in Soulsby & Damgaard (2005b), sheet flow conditions can exist even in the presence of ripples: sediment moves as a sheet over the ripples, but the ripples remain immobile.

To confirm this results, we fitted observed mean sediment concentration profiles to exponential, Rouse and power-law profiles. Other studies have observed the exponential profile when sediment was being resuspended by vortex shedding over rippled beds (Nielsen (1982); Ribberink & Al-Salem (1994)). The Rouse profile was originally derived for flows in rivers or channels, but has been applied to profiles of suspended sediment measured under waves (Soulsby (1997)). The power-law profile, derived by Smith (1977), has been observed in the field and in the laboratory (Dohmen-Janssen & Hanes (2002); Sumer *et al.* (1996); Ribberink & Al-Salem (1995); Lee *et al.* (2004). Both Rouse and power law profiles are usually indicative of sheet flow conditions (Soulsby (1997)). Expressions for these theoretical profiles of mean sediment concentration are:

$$C(z) = \begin{cases} C_o e^{-z/l} & \text{(Exponential profile)} \\ C_o \left[\frac{z}{z_o} \frac{h-z_o}{h-z} \right]^{-b} & \text{(Rouse profile)} \\ C_o \left(\frac{z}{z_o} \right)^{-b} & \text{(Power profile)} \end{cases}$$

In the exponential profile, l is a decay length scale (Nielsen (1982); Soulsby (1997)). In the Rouse and power profiles, h is the water depth, z_o a reference height above the seabed

where the reference concentration C_o is defined (we take $z_o = 0.8$ cmab herein), and b is a suspension parameter (Soulsby (1997)):

$$b = \frac{w_o}{\kappa u_*} \tag{2.5}$$

with u_* the friction velocity, and $\kappa = 0.4$ the von Karman constant.

We fitted our measured profiles with the distributions presented in Equation 2.5, and for each profile, we computed values of the coefficient of determination R^2:

$$R^2 = 1 - \frac{\sum_{n=1}^{N} \left(C_i^{meas} - C_i^{fit} \right)^2}{\sum_{n=1}^{N} (C_i^{meas} - < C_i >^{meas})^2} \tag{2.6}$$

where C_i^{meas} represents the discrete measurements of mean sediment concentration at the i^{th} cross-shore position, $< C_i^{meas} >$ is the mean value of C_i^{meas}. C_i^{fit} represents the values of fitted profile *C(z)* at the same N elevations as the measured mean concentration C_i^{meas}. An R^2 value of 1 means a perfect fit between model and observed profiles. A negative R^2 value indicates that the mean value $< C_i^{meas} >$ represents the vertical variation of the data better than the theoretical formulation. We fitted the measured profile with theoretical values between $z_o = 0.8$ to $z = 17$ cmab. Similar results were achieved using $z_o = 1.8$ cmab and $z_o = 5$ cmab.

The exponential profile did not fit our observations very well. R^2 values where negative for 95% of the runs. On the other hand, the Rouse and power profiles performed equally well, with R^2 values greater than 0.9 during generation of bar O and stagnation of bar M. High R^2 values were obtained during generation of bar M, averaging around 0.7. This would indicate that sheet flow conditions probably dominated during the experiment, and the ripples observed did not contribute to sediment transport.

In summary, for all cases considered, sand was mainly suspended in regions close to the sandbars and where wave breaking reached approximately 20%. Contributions from wave- and low-frequency components of the velocity generally compensated each other, even though waves experienced significant changes as they propagated over the bars and in the surf zone region (see Section 2.3). This balance between low-frequency and wave contribution is consistent with observations in the field by Beach & Sternberg (1991); Huntley & Hanes (1987). During the generation of bars O and M, this balance was approximately the same, in the cross-shore direction as well as in the water column. During stagnation of bar M, low-frequency and wave-induced fluxes were directed offshore.

During offshore bar generation, when waves were relatively high, both bedload and suspended flux contributed to the growth of the bar. During the milder wave conditions of middle bar generation and middle bar stagnation, suspended flux and bedload were generally moving in opposite directions. Because of the offshore direction of the suspended flux during these periods, bedload was much higher than the measured shoreward oriented total sediment flux.

We also estimated that sheet flow conditions were likely in the flume. Although other publications reported a reversal in the direction of suspended sediment transport, few have found a reversal of transport in the surf zone, and at elevations so close to the bed. Green & Vincent (1990) and Osborne & Greenwood (1992b) found a reversal of transport direction in suspended sediment transport offshore of the breakpoint, and their lowermost instrument was higher than 5 cmab. Wright *et al.* (1991), found that suspended and bed load were of similar magnitude in water depths of 7 to 9 meters off Duck, N.C. In the surf zone, Conley & Beach (2003) found shoreward directed suspended sediment transport due to wave motions at 2 cm above the bed. We are not aware of publications that mention differing bedload and suspended load transport in the surf zone, as we have found during our experiment.

2.5 Modeling of Sediment Transport: Theory

In this section, we present the two process-based models that we used to model the observed sediment transport in the flume. The first model is a wave-averaged model that is expressed as a function of velocity moments. The second model is a wave-resolved model that estimates suspended and bedload transport based on hydrodynamics modeled by an eddy-diffusive boundary layer model.

2.5.1 Wave-Averaged Model

The wave-averaged model that we used is a modification of the energetics models of Bowen (1980) and Bailard (1981) proposed by Hoefel & Elgar (2003). These models derive from the pioneering work of Bagnold (1963) and Bagnold (1966). In his model for sediment transport in river, Bagnold (1966) started from the idea that a work done by an internal force (here bed shear stress) generates dissipation:

$$\omega = \tau|\vec{u}| = \rho C_f |\vec{u}|^3 \tag{2.7}$$

where ω is the dissipated stream energy, and C_f is a friction coefficient. Next, Bagnold (1966) assumed that the transport rate of sediment in the water can be evaluated from the rate of energy used by the stream to transport sediment. Sediment put into motion by the shear stress can move as either bedload or suspended load. Incorporating effects of gravity and assuming that suspended sediment transport can be expressed as a fraction of total energy dissipated by the stream, Bagnold (1966) proposed the following formula for total transport:

$$i = i_b + i_s = \left(\frac{\epsilon_b}{\tan\phi - \tan\beta} + \frac{\epsilon_s}{w_o/\overline{u} - \tan\beta} \right) \omega \tag{2.8}$$

where i is the total transport rate, composed of bedload i_b and suspended load i_s. $\overline{u}$ is the mean velocity of the stream, and w_o is the sediment fall velocity. ϵ_b and ϵ_s are the bedload and suspended load efficiency. $\tan\phi$ is the sediment angle of repose (equal to 0.66

(Bagnold (1966))), and $\tan\beta$ the beach slope.

Bowen (1980) and Bailard (1981) revisited Bagnold (1966) work to devise a similar relationship for flows in nearshore environment by including oscillatory flows, i.e. $u = \widetilde{u}+\overline{u}$, in Equation 2.8. After expansion, they found an expression for bed and suspended cross-shore volumetric transport rate, per unit width per unit time:

$$Q_{Bailard} = K_b\left[\left\langle|\vec{u}|^2\tilde{u}\right\rangle + \left\langle|\vec{u}|^2\bar{u}\right\rangle - \frac{\tan\beta}{\tan\phi}\left\langle|\vec{u}|^3\right\rangle\right] + K_s\left[\left\langle|\vec{u}|^3\tilde{u}\right\rangle + \left\langle|\vec{u}|^3\bar{u}\right\rangle - \frac{\epsilon_s}{W}\tan\beta\left\langle|\vec{u}|^5\right\rangle\right] \tag{2.9}$$

where $\vec{u}$ is the total cross-shore velocity, measured above the wave bottom boundary layer, and $\tilde{u}$ and $\bar{u}$ are its oscillatory and mean components. Brackets, '$<>$',represent time averaging. Bedload and suspended transport coefficients, K_b and K_s, are:

$$K_b = \frac{\rho_w}{g(\rho_s-\rho_w)}C_b\frac{\epsilon_b}{\tan\phi} \qquad K_s = \frac{\rho_w}{g(\rho_s-\rho_w)}C_f\frac{\epsilon_s}{\tan\phi} \tag{2.10}$$

where ρ_s and ρ_w represent the density of sand and water, respectively. C_f (with a standard value of 0.03 (Thornton *et al.* (1996))) is the drag coefficient on sand particles, and the coefficients ϵ_b and ϵ_s are empirical, whose values will be taken as 0.135 and 0.015, respectively (Thornton *et al.* (1996)). Analysis of the various terms in this model shows that the transport is mostly dependent on wave skewness ($\sim|\vec{u}|^3$) and undertow ($\bar{u}$). This model gives good results when undertow (which causes offshore sediment movement) or wave (velocity) skewness (which cause shoreward sediment movement) are strong. It fails to predict transport when undertow is weak and waves are more asymmetric than skewed (Thornton *et al.* (1996); Gallagher *et al.* (1998)).

The lack of success of the energetics model is due to the fact that one of the dominant wave-induced transport terms in Equation 2.10, $<\widetilde{u}^3>$, goes zero for asymmetric waves. As experiments by King (1990), Ribberink *et al.* (2000) and Dohmen-Janssen & Hanes

(2002) have shown, for the same value of skewness, waves that have a certain degree of asymmetry transport much more sediment than waves that are purely skewed. Later, Elgar *et al.* (2001) observed that free-stream velocity asymmetry is closely related to acceleration skewness. Acceleration can be assumed to be represented by pressure gradients, and thus skewed acceleration time series will generate large pressure gradients under the sharp front face of asymmetric waves, and weaker pressure gradients under the mild rear of asymmetric waves. If these pressure gradients are strong enough, sediment is put into motion. These observations led Drake & Calantoni (2001) to suggest a threshold factor above which sediment is put into motion by the effects of acceleration skewness. Hoefel & Elgar (2003) incorporated this last idea in the model developed by Bailard (1981) and Bowen (1980) to compute total sediment flux Q_T in the nearshore:

$$Q_T = Q_{Bailard} + Q_{acc} \tag{2.11}$$

where Q_{acc} accounts for the cross-shore sediment transport caused by wave asymmetry (acceleration skewness) effects:

$$Q_{acc} = \begin{cases} K_a \left(a_{spike} - \text{sign}(a_{spike}) a_{crit}\right) & \text{if } a_{spike} \geq a_{crit} \\ 0 & \text{if } a_{spike} \leq a_{crit} \end{cases}$$

where acceleration skewness is parameterized by $a_{spike} = \left\langle a^3 \right\rangle / \left\langle a^2 \right\rangle$, with a the low-passed filtered acceleration signal (we chose a cutoff frequency $f_c = 1$Hz to remove seiching signal), and brackets represent the averaging operation. K_a is a calibration constant, and a_{crit} is an acceleration threshold for initiation of transport. Hoefel & Elgar (2003) suggested $K_a = 1.410^{-4} m/s$ and $a_{crit} = 0.2 m/s^2$. This model will be referred as the Enhanced Energetics Model (EEM) in the remainder of this paper.

2.5.2 Wave-Resolved Model

As an alternative to the wave-averaged model, we also modeled bedload and suspended sediment transport with a wave-resolving model. We combined an eddy-diffusive suspended sediment transport model, following the work of Henderson *et al.* (2004). We modeled bedload from wave-resolved velocity near the bed using the sheet flow formulation of Ribberink (1998).

To run our suspended and bedload models, we simulated velocity time series in the lower portion of the water column from the weakly nonlinear model of Henderson *et al.* (2004), which was developed for the wave bottom boundary layer (WBBL):

$$\frac{\partial u}{\partial t} - \frac{1}{C_o} u \frac{\partial u}{\partial t} + w \frac{\partial u}{\partial z} = \tag{2.12}$$

$$\left[\frac{\partial u^T}{\partial t} - \frac{1}{C_o} u^T \frac{\partial u^T}{\partial t} + w^T \frac{\partial u^T}{\partial z} - \frac{\partial}{\partial z}(\nu_t \frac{\partial u^T}{\partial z}) \right] + \frac{\partial}{\partial z}(\nu_t \frac{\partial u}{\partial z}) \tag{2.13}$$

where $C_o = \sqrt{gh}$, the wave phase speed in shallow water, and *u(x,z,t)* and *w(x,z,t)* are the horizontal and vertical fluid velocities evaluated at each vertical grid point z of the model domain. The first term between brackets on the right hand side of Equation 2.13 represents the second order estimate of the pressure gradient inside the WBBL (for details, cf. Appendix B of Henderson *et al.* (2004)), which is computed using measured velocities at the top of the domain, u^T. Eddy viscosity $\nu_t(x, z, t)$ is computed at each time step from a $k - \epsilon$ turbulence closure scheme (Pope (2000); see also Appendix A of Henderson *et al.* (2004)). These equations were developed assuming that waves were in shallow water and of permanent form. In addition, Henderson *et al.* (2004) assumed that low-frequency signals were in a constant stress layer, which means that vertical derivatives of mean shear stress is zero.

To estimate suspended load, we followed the work of Henderson *et al.* (2004), in which sediment is mobilized at bed level by a pickup function dependent on bed shear stress

(Equation (15) of Henderson *et al.* (2004)):

$$-\nu_t \frac{\partial C}{\partial z} = \begin{cases} \zeta w_o C_{ref} & \text{if } \tau_b > \tau_c \\ 0 & \text{if } \tau_b \leq \tau_c \end{cases} \tag{2.14}$$

Instantaneous bed shear stress τ_b was estimated from $\tau_b = \nu_t \partial_z u(x, z_l, t)$, where *u(x,z,t)* was the modeled time series of horizontal velocity at the lowermost grid point z_l. ∂_z denotes the derivative with respect to z. In Equation 2.14, ζ is a function of sediment diameter and bed shear stress. C_{ref} is a reference concentration estimated two grain diameters above the bed, and is a function of the excess shear stress (Smith & McLean (1977)):

$$C_{ref} = \alpha \left(\frac{\tau - \tau_c}{\tau_c} \right)^{\beta} \tag{2.15}$$

Coefficients α and β were introduced by Henderson *et al.* (2004) as calibration parameters.

Once the concentration of sediment at the lowermost grid point in the computational domain had been estimated, we distributed it in the water column following the classical advection/diffusion equation (Fredsøe & Deigaard (1992), Nielsen (1982)):

$$\frac{\partial C}{\partial t} + u \frac{\partial C}{\partial x} + (w - w_o) \frac{\partial C}{\partial z} = \frac{\partial}{\partial z} \left(\epsilon_f \frac{\partial C}{\partial z} \right) \tag{2.16}$$

where *C(z,t)* ([Vol/Vol]) is the sediment concentration, w_o the sediment fall velocity (see Section 2.2), and ϵ_f is the sediment eddy diffusivity. Total suspended sediment flux Q_s was computed by:

$$Q_s(x) = \int_{z_L}^{z_T} \langle C(x, z, t) u(x, z, t) \rangle \, dz \tag{2.17}$$

where z_L represents the height of the lowermost model grid point and z_T represents the elevation at the top of the computational domain.

Bedload transport Q_b under sheet flow conditions was estimated by the formulation of

Ribberink (1998), which is a modification of the Meyer-Peter & Müller (1948) equation:

$$Q_b = \Psi \sqrt{(s-1)gd^3} \tag{2.18}$$

where $\Psi = \left\langle 11\,\theta/|\theta|[|\theta| - \theta_c]^{1.65} \right\rangle$ is the non-dimensional transport rate, with

$$\theta = \frac{\tau_b}{\rho(s-1)gd} \tag{2.19}$$

the Shields parameter. θ_c (=0.05) is the critical Shields parameter for sediment motion. The parameters τ_b, ρ, s, and d represent the bed shear stress, water density, sediment specific gravity and sediment diameter, respectively.

Bed shear stress due to wave and current, τ_b, was computed by:

$$\tau_b = \tau_c + \tau_w \tag{2.20}$$

where subscripts w and c represent components of the shear stress τ.

Shear stress due to waves only, τ_w, was computed assuming law-of-the-wall formulation (Hsu *et al.* (2006)):

$$\tau_w = \rho \left(\frac{\kappa}{\ln(30 z_l / k_s)} \right) \widetilde{u}(z_l, t) |\widetilde{u}(z_l, t)| \tag{2.21}$$

where $\widetilde{u}(z_l, t)(zl, t)$ represents demeaned wave velocity at the first grid point z_l above the bed, and $\kappa = 0.4$. The roughness height coefficient k_s is a calibration factor. Shear stress due to the undertow was computed with:

$$\tau_c = \frac{1}{2} \rho f_c \overline{u} |\overline{u}| \tag{2.22}$$

where $\overline{u}$ represents the strength of the undertow at the first grid point, and f_c is a friction factor. From the application of bedload and suspended load model, total sediment transport flux was evaluated by adding bedload and suspended flux $Q_T = Q_s + Q_b$.

2.6 Modeling Results

We applied the EEM and wave-resolved models to the dataset, and evaluated their relative performance. Our objective was to identify components of the models that correctly reproduce the observed magnitude and modes of sediment transport (suspended and bedload). As mentioned in Section 2.3, waves and hydrodynamics were affected by the bathymetric changes that took place from one run to another. However, we also estimated that variations in velocity moments was relatively limited across one phase. We will assume that any measurement made during a phase of bed evolution was representative of this phase.

2.6.1 Enhanced Energetics Model

To apply the EEM model to our dataset, we had to change the calibration coefficients proposed by Hoefel & Elgar (2003). Similar to Hoefel & Elgar (2003), we used all velocity measurements from the ADV located below 25 cmab. We calibrated the model by minimizing rms errors between measured and modeled sediment fluxes , for each phase of bed evolution identified in Section 2.3. This operation yielded different values of calibration coefficients C_f, K_a and a_{crit} (Equations 2.10 and 2.11) for each phase of bed evolution. In order to use only one model parametrization for all phases considered herein, we decided to use values of $C_f = 1.2$, $K_a = 8.510^{-6}$, and $a_{crit} = 0.08$. These coefficients are different from the ones proposed by Hoefel & Elgar (2003) (see Section 2.5) and were obtained by minimizing rms errors between modeled and measured sediment fluxes during offshore and middle bar generation phases only.

Figures 2.16 to 2.18 compare modeled and measured sediment flux, for offshore bar generation and middle bar generation and stagnation. For the offshore bar generation phase (Figure 2.16), modeled and measured fluxes do not agree ($R^2 = 0.27$). The model underestimates the offshore transport of sediment in the surf zone and fails to reproduce

the shoreward transport that occurred at $X \approx 60\,m$. In another study, Thornton *et al.* (1996) explained the observed shoreward sand migration in regions offshore of the surf zone have been by action of wave skewness. In our study, transport terms due to velocity skewness indicated offshore transport.

In the surf zone, $Q_{Bailard}$ was oriented offshore and, with the friction factor chosen, approximates 70% of the observed transport (Figure 2.16). The shoreward oriented flux due to acceleration skewness Q_{acc} was quite large, and reduced the influence of $Q_{Bailard}$ in the total modeled transport. Most of the transport in $Q_{Bailard}$ was due to the suspended load term, which was twice as large as the bedload term. $Q_{Bailard}$ approximated the suspended flux relatively well; difference between measured and modeled suspended flux was 19% and gave an R^2 of 0.6. However, more than 50% of the transport was due to wave action, which as contrary to observation. To calibrate the EEM specifically for this case, the acceleration skewness term would need to be eliminated, and the friction factor C_f increased.

The EEM explained middle bar generation well (Figure 2.17), yielding an R^2 value of 0.8. If the measurement at $X \approx 78\,m$ is excluded, R^2 increases to 0.95. As expected from observation in Section 2.3, acceleration skewness (Q_{acc}) explained most of the shoreward transport observed in regions offshore of the middle bar. The Bailard term ($Q_{Bailard}$) contributed little to the observed positive flux. Shoreward of bar M ($X > 68\,m$), the importance of undertow in $Q_{Bailard}$ increased, and the importance of velocity skewness weakened. A strong offshore flux resulted, which balanced the action of acceleration skewness, and yielded a total transport with the correct sign and magnitude. In accordance with observations, suspended transport was weak overall, and approximated measured flux by a factor of two in the surf zone ($R^2 < 0$). Offshore of the bar crest, the disagreement was more pronounced. Here, the model predicted shoreward suspended flux on the offshore face of the bar, when in reality suspended sediment was moving offshore (Figure 2.14).

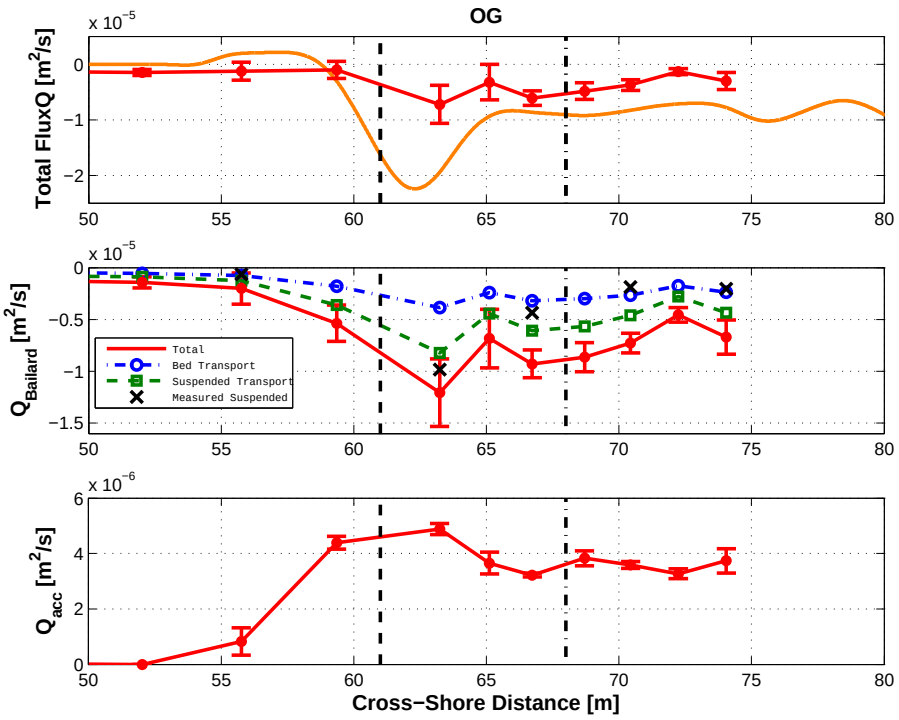

Fig. 2.16: EEM results for offshore bar generation. Top panel: Measured (orange curve) versus modeled (blue curve) sediment flux using EEM for offshore bar generation. Error bars represents 1 standard deviation around the mean. Middle panel: $Q_{Bailard}$ (red curve) decomposition into bed load (dashed blue curve) and suspended load (green dashed curve). Bottom panel: Estimate of Q_{acc}. Measured suspended transport is indicated by black crosses. Dashed and dashed-dotted lines represent average location of offshore and middle bars, respectively.

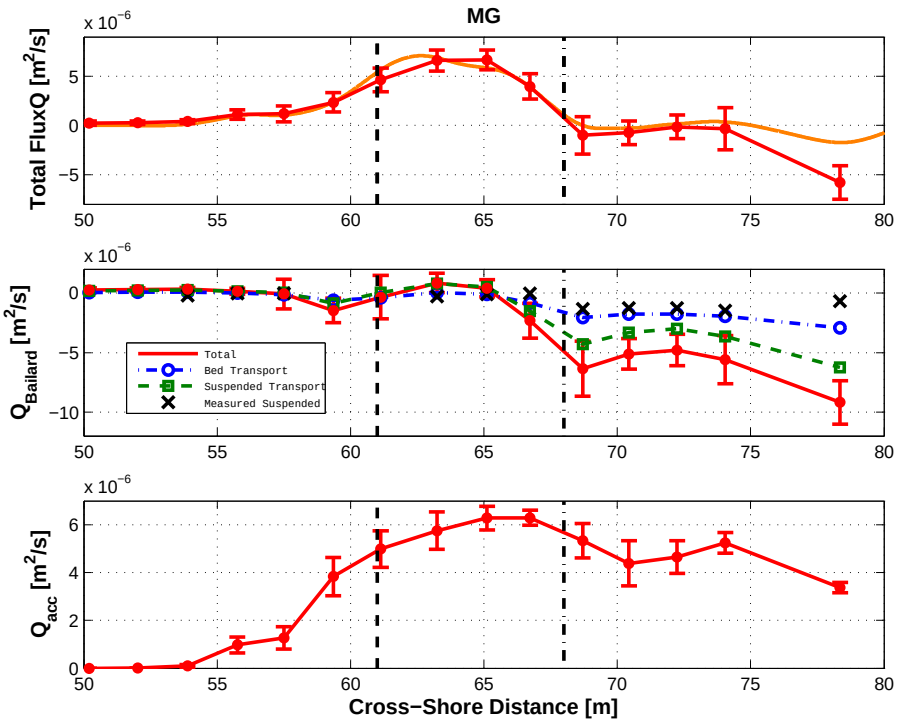

Fig. 2.17: EEM results for middle bar generation. Top panel: Measured (orange curve) versus modeled (blue curve) sediment flux using EEM for offshore bar generation. Error bars represents 1 standard deviation around the mean. Middle panel: $Q_{Bailard}$ (red curve) decomposition into bed load (dashed blue curve) and suspended load (green dashed curve). Bottom panel: Estimate of Q_{acc}. Measured suspended transport is indicated by black crosses. Dashed and dashed-dotted lines represent average location of offshore and middle bars, respectively.

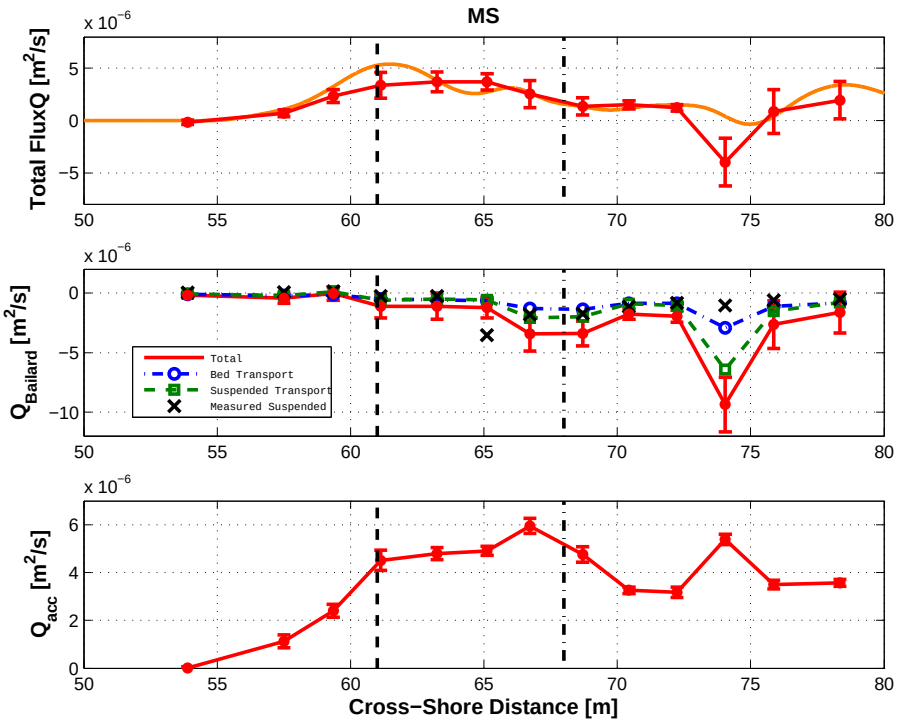

Fig. 2.18: EEM results for middle bar stagnation. Top panel: Measured (orange curve) versus modeled (blue curve) sediment flux using EEM for offshore bar generation. Error bars represents 1 standard deviation around the mean. Middle panel: $Q_{Bailard}$ (red curve) decomposition into bed load (dashed blue curve) and suspended load (green dashed curve). Bottom panel: Estimate of Q_{acc}. Measured suspended transport is indicated by black crosses. Dashed and dashed-dotted lines represent average location of offshore and middle bars, respectively.

Finally, application of the model to middle bar stagnation yielded reasonable results (Figure 2.18) . The model correctly predicted the shoreward movement of sediment offshore of the middle bar. In the surf zone, the model overestimated the offshore sediment flux at $X \approx 74\,m$, but correctly predicted the shoreward flux closer to the shoreline. After eliminating the data point at $X \approx 74\,m$, R^2 increased to 0.73. Similar to the previous case, most of the shoreward sediment transport was explained by the action of the acceleration skewness. The wave transport term in the Bailard formulation was, on average, directed shoreward, but was fairly weak compared to the sum of gravity and undertow-driven transport. In the surf zone, the model predicted that the wave term would move sediment offshore with greater capability than would undertow and gravity, which is contrary to our observations. Interestingly, suspended load predicted by the Bailard formulation approximated measured suspended load fairly well, except at $X \approx 74\,m$, and slightly offshore of the bar.

In summary, the EEM demonstrated some ability in reproducing the observed sediment flux in the flume during the three bed evolution phases. The inclusion of the acceleration skewness term (Q_{acc}) negatively impacted the model during offshore bar generation. Neglecting this term would have resulted in improved prediction skill. However, during middle bar generation and middle bar stagnation, the inclusion of Q_{acc} was critical to calculate shoreward sediment transport, as the Bailard term predicted offshore transport.

Finally, frequency decompositions of the Bailard suspended transport terms (following Thornton *et al.* (1996)), indicated that wave and low-frequency components did not balance each other in the surf zone. Undertow and low-frequency terms also dominated in regions offshore of the bar. This is different from the suspended sediment flux balance observed in the flume (see Section 2.4.2). These findings suggest that the Bailard model did not accurately reproduce the details of sediment transport, even though it reproduced the bulk sediment flux quite well.

2.6.2 Results of Wave-Resolved Model

We used the wave boundary layer model developed by Henderson *et al.* (2004) to obtain velocity time series in a computational domain defined between 25 and 0.8 cmab. Model outputs were used to model observed suspended sediment transport and bedload. Roughness height was fixed at 2 times the mean sediment diameter. Following Henderson *et al.* (2004), the model was driven with a velocity signal measured at 25 cmab; when signals at 25cmab are too noisy, velocity measured at 10cmab was used instead, but domain height remained at 25 cm.

Boundary Layer Model: Hydrodynamic Module

Henderson *et al.* (2004) assumed that waves were in a constant stress layer in the computational domain. Our observations contradicted this assumption, which indicated strong mean velocities from 25 to 1 cmab (see error bars in Figure 2.5). Our modification of the model involved the addition of a depth uniform pressure gradient to the expression of the second order pressure gradient (term between brackets on the RHS of Equation 2.13, or see Equation 10 of Henderson et al.(2004)). To perform this calibration, we made sure that model and measured mass flux matched over the same portion of the water column: $\int_{z_1}^{z_2} U_{meas}\, dz = \int_{z_1}^{z_2} U_{model}\, dz$, where U_{meas} and U_{model} represent measured and modeled undertow values. To improve our estimates, measured undertow values were fit to a parabolic profile between z_1 and z_2, an elevation range where valid measurements of the undertow were obtained. We could not justify pressure gradient values added to the model. However, they generally increased with distance along the flume towards the shoreline, which is physically reasonable. Alternatively, one can assume that undertow is uniform throughout the water column and simply add a depth-averaged value of the undertow (e.g., obtained from a wave driver) to the model. Conclusions presented herein hold under these circumstances as well.

After calibrating the user-defined pressure gradient, percent rms error between mea-

sured and modeled undertow was on the order of 20% in the surf zone. This value is comparable to error reported elsewhere between estimates and modeled depth-averaged undertow values (Dally & Brown (1995)). In offshore regions (at approximately 10 meters offshore of the crests of offshore and middle bars), the percent rms error was greater, on the order of 70%. We noticed also that estimates of undertow closer to the bed tended to be worse than higher up in the water column.

For each run simulated in the model, we evaluated how well measured and modeled velocity compared. We estimated rms error, R^2 and best fit slope β between modeled and measured velocity at 15, 10, 5 and 1 cmab. We show cross-shore averaged values of these statistics in Table 2.3. In general, error increased closer to the bed, but the model performed relatively well, given the strong assumptions that were made during its development. For each phase of bed evolution considered, rms error values were on the order of 0.1 m/s higher in the surf zones than in shoaling regions. Similarly, R^2 values decreased by approximately 0.1 between shoaling region and surf zone. In addition, the model was generally accurate at reproducing measured low-frequency and wave variance σ^2_{Wave} and σ^2_{LF}. R^2 values were on the order of 0.7, with lower values at 1cmab than at 15 cmab. Also, rms error was on the order to $7.10^{-}3$ at 15 cmab and increased to 12.10^{-2} m^2/s at 1 cmab. Best-fit slope was on the order of 1.1 from 15 to 10 cmab, and decreased to approximately 0.7 at 1cmab. This result indicates that, modeled velocities should reproduce the observed balance between undertow, wave and low-frequency suspended sediment fluxes.

Table 2.3: Statistics between Measured and Modeled Velocities

Inst. Elev. [cmab]	R^2	Error (rms) [m/s]	β
15	0.97	0.08	1
10	0.95	0.1	0.94
5	0.88	0.13	1
1	0.72	0.2	0.65

In summary, a weakly nonlinear, shallow water boundary layer model approximated

closely the velocities in the lower portion of the water column. Error increased closer to the bed and in higher energetic regions but, given the strong assumptions that were used in the development of these equations, the model performed relatively well. We do not expect this model to be a major source of error in the modeling of suspended sediment transport.

Boundary Layer Model: Sediment Module

The sediment module estimates reference concentration at each time step at the lower boundary of the model by assuming a Shield's law parametrization (see Section 2.5). As shown in Equation 2.15, the sediment reference concentration is a function of the excess shear stress estimated at the bed. This shear stress is strongly dependent on wave motions. After the model determines that excess shear stress is positive, sediment is advected/diffused following the classical advection/diffusion equation and using eddy viscosity as sediment eddy diffusivity (see Equation 2.16).

In our dataset, sediment concentration signals were correlated in the water column. Specifically, in regions of high suspended load, the correlation coefficient between adjacent sensors was around 0.55 at the 95% confidence level. Correlation coefficients between sensors in the water column and the sensor at 0.8 cmab was around 0.45 at the 95% confidence level. However, sediment concentration spectra did not show any significant peak at the frequencies of wave or low-frequency cyclic motions. Sediment suspension signals were highly intermittent. Although some datasets of nearshore sediment concentration exhibited a direct correspondence between sediment suspension and wave forcing (Ruessink *et al.* (1998), Jaffe *et al.* (1984), Conley & Beach (2003)), measurements of intermittent suspended sediment signals have been reported (Smith & Mocke (1993); Jaffe & Rubin (1996); Kobayashi *et al.* (2005); Wang *et al.* (2002); among others). Such intermitence could be associated with wave-induced dissipation (Smith & Mocke (1993); Hsu & Liu (2004)). This is in line with findings of Cox & Kobayashi (2000), who showed that surface

generated turbulence often reaches the bed. Consequently, a parametrization of sediment reference concentration based on excess shear stress (Smith & McLean (1977)) might not be appropriate for our study. The inadequacy of such models has also been showed by Nielsen *et al.* (2002). Instead, we evaluated sediment advection/diffusion in our model domain by using measured sediment concentration time series at 0.8 cmab as the concentration at the first grid point.

Finally, although eddy viscosity and eddy diffusivity are often assumed to be equal (van Rijn (1984)), we found it necessary to increase the eddy-viscosity values computed by the $k-\epsilon$ model. Few publications have evaluated the ratio β between eddy diffusivity and eddy viscosity. From measurements on the continental shelf, values of the coefficient β were above and below unity, but in general less than 1.5 (Lees (1981); Dyer & Soulsby (1988); Ogston & Sternberg (2002)). van Rijn (2006) proposed a value of less than 1.5 for nearshore regions. Thorne *et al.* (2009) indicated that this ratio might be much greater than 4 over rippled beds in the surf zone, and Nielsen (1982) recommended a value of $\beta = 4$. For each bed phase considered herein, calibration values were around 10 in the shoaling region of the waves. In the surf zone, calibration coefficient β was approximately 5 (for an heuristic justification of these calibration numbers, see Appendix B.1).

After this calibration, the correlation between measured and modeled time series of sediment concentration averaged 0.5 for all phases considered, throughout the flume. Visual inspection of measured and modeled time series of sediment concentration indicated that the model reproduced the same sediment suspension events that were detected throughout the water column, but the model underestimated the peak values of sediment concentrations. The agreement improved in the surf zone, where correlation values sometimes reached 0.7.

For all phases of bed evolution, the model correctly estimated the observed suspended sediment flux (Figure 2.19). R^2 between measured and modeled total suspended sedi-

ment flux was 0.88 during generation of bar O, 0.6 during generation of bar M, and 0.7 during stagnation of bar M. Except in regions far offshore ($X \approx 55\,m$) where suspended sediment transport was small, the model predicted the correct direction and magnitude of transport in the flume. Additionally, transport due to low- and wave-frequencies were balanced, even though the model under-estimated the strength of the wave-only transport.

Bed Load and Total Load Model Results

As indicated in Section 2.5.2, bedload was estimated from the MPM formula. Shear stress was estimated as the sum of wave and current shear stress, from Equations 2.21 and 2.22. For each phase of bar evolution, shear stress was calibrated by using cross-shore uniform roughness height k_s and friction coefficient f_c (see Equations 2.21 and 2.22). The cross-shore uniformity of the calibration coefficient, though practical, is probably slightly erroneous. Roughness can vary in the cross-shore region and increase in the surf zone (Feddersen *et al.* (2003)). However, for our study, k_s and f_c serve as calibration factors.

We first applied the bed load model to the offshore bar generation case. Bed roughness k_s was set at $1d$, where d represents sediment median grain size. This value is representative of relatively flat beds, where sheet flow is likely to occur. The friction factor f_c was set at 0.035, within the range of standard values but an order of magnitude larger than the expression proposed by Soulsby (1997).

Overall, the model correctly predicted the strength of bed load in regions closer to shore ($X > 70\,m$), but underestimated transport closer to the offshore bar trough, where highest sediment flux was observed (Figure 2.19), $X \approx 63\,m$). Analysis of model results with and without mean currents indicated that total bed transport during generation of bar O was dominated by the undertow, with wave transport moving sediment shoreward. R^2 between measured and modeled bed transport was 0.1. This low R^2 value can be attributed to the model inability to reproduce the strong undertow that occurred at

$X \approx 63\,m$. When we used measured mean velocity instead of modeled velocity, the R^2 was 0.5.

To model shoreward transport during middle bar generation, roughness height k_s was increased to *8d*. This value is higher than during offshore bar generation. However, if we had used the dimension of the ripples observed in the flume, we would have obtained a roughness of approximately *30d*, following Nielsen (1982). Although k_s is here a calibration coefficient, the lower value of *8d* that we obtained is, once again, an indication that our assumption of flat bed (sheet flow conditions) is sensible. We used $f_c = 0.005$, which is 30% higher than the value obtained using the expression proposed by Soulsby (1997). Overall, the model correctly predicted the shoreward transport of sediment that we observed in the shoaling region (Figure 2.19, $X < 70\,m$), but over-estimated the strength of transport in the surf zone. For the whole profile, R^2 values were negative. Omitting the surf zone, R^2 value increased to 0.8. Comparison between model resuls with and without mean current indicated that most of the bedload was due to the action of wave orbital velocity.

During middle bar stagnation, k_s was changed to $6d$, and f_c was set to 0.025, which an order of magnitude larger than the expression proposed by Soulsby (1997). Similar to the middle bar generation phase, the model predicted the correct suspended sediment flux magnitude in the shoaling region, but overestimated the strength of the flux in the surf zone (Figure 2.19). Overall R^2 value was negative, but, omitting surf zone region ($X > 70\,m$), R^2 value increased to 0.7.

Finally, Figure 2.19 shows our modeled values of total flux, obtained by summing bed and suspended fluxes. For the generation of bar O, the R^2 value was estimated to be approximately 0.6. It increased to 0.7 when we used measured mean velocities. For the generation and stagnation phases of bar M, the R^2 value was negative when we considered the whole profile. It increased to 0.6 for bar M generation, and 0.4 for bar M stagnation,

when we only considered regions offshore of the breakpoint, at $X \approx 70\,m$. Despite some errors in the surf zone during the generation and degeneration of bar M, our model reproduced total transport in regions of maximum sediment fluxes relatively well, for all cases considered.

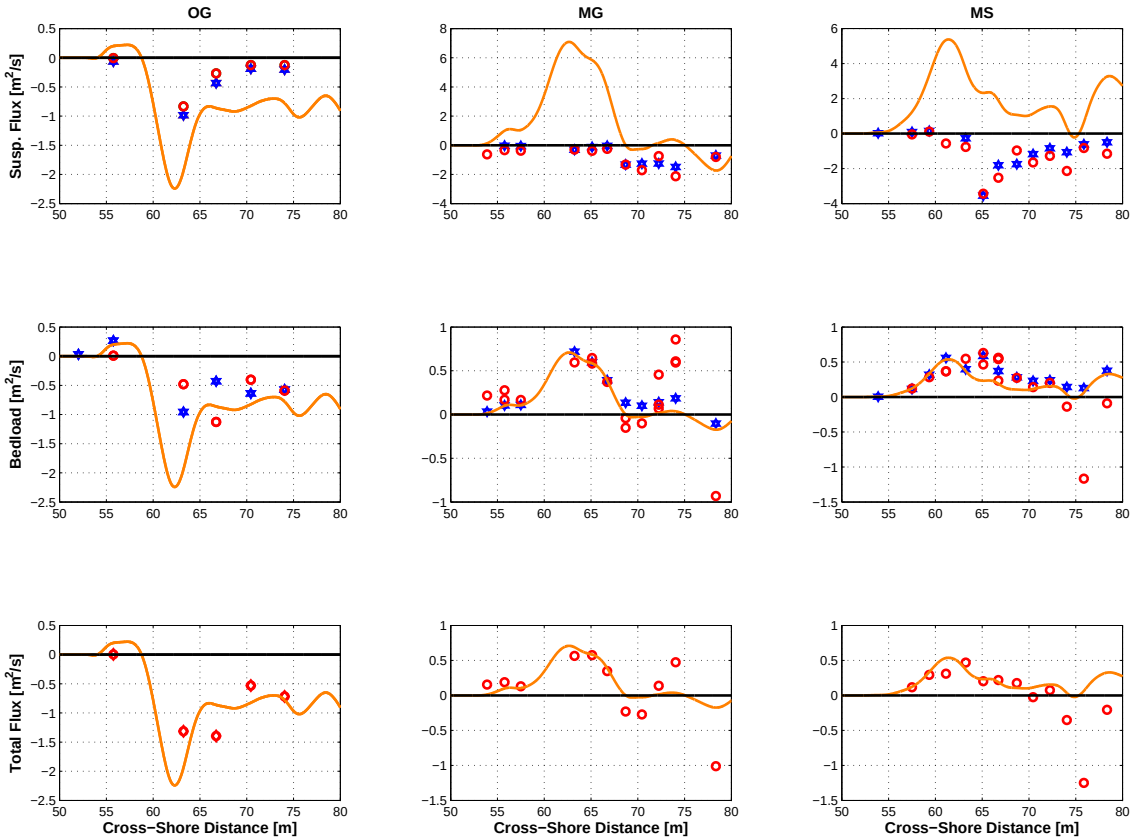

Fig. 2.19: Suspended, bedload and total sediment fluxes obtained with the wave-resolving model. Top panels: Comparison between measured total (orange curve), measured suspended (blue stars) and modeled suspended (red circles) sediment flux, during offshore bar generation ('OG'), left column, middle bar generation ('MG'), middle column, and middle bar degeneration ('MS'), right column. Middle panel: Comparison between measured total sediment flux(orange curve), measured bedload (blue stars) and modeled bedload (red circles). Bottom panel: Comparison between measured total (orange curve), and modeled total (red circles) sediment flux

2.7 Conclusion

We successfully modeled the generation and degeneration of two sandbars under laboratory settings. A sandbar, which we named offshore bar, or bar O, was formed under storm conditions. It was generated by the offshore transport of sediment from nearshore regions. Both bedload and suspended sediment transport played an important role in the formation of the bar. Under milder conditions, sediment originating from the offshore bar moved shoreward to form another sandbar, which we named middle bar or bar M. Such shoreward movement is likely due to effects of acceleration skewness. The final position of the middle bar during these conditions was close to the breakpoint. In the surf zone, we observed little total transport. After slight changes in wave conditions, undertow increased and acceleration skewness decreased. The stagnation of the sand bar resulted, but shoreward movement of sand was observed offshore of the bar, in regions where undertow was weak.

Sediment moved offshore mostly as suspended load, and we hypothesized that most shoreward transport occurred as bedload. Suspended load was dominated by the undertow throughout the water column. Fluxes due to wave and low-frequency motions were non-negligible and balanced each other. As observed at other studies, sediment suspension signals were episodic and did not respond to the cyclic wave or low-frequency forcing. These results show that both modes of transport have to be taken into account when modeling sediment transport in nearshore regions, and that bed load and suspended sediment flux can sometimes move in opposite direction. Also, they confirm the non-negligible role of wave and low-frequency suspended sediment transport.

Finally, the energetics model of Hoefel & Elgar (2003) reproduced observed transport of sediment with a high accuracy. It also modeled observed suspended sediment flux fairly well during offshore bar generation and stagnation, which would indicate that effects of acceleration skewness induce bedload transport. However, the model does not reproduce the observed balance between wave and low-frequency fluxes. We also successfully mod-

eled the observed sediment transport by combining a suspended load model and a bed load model, using velocity time series modeled with an eddy-diffusive boundary layer model. We were unable to model observed profiles of sediment concentration time series using a wave-dependent shear stress. This indicates that intermittent sediment concentration time series can not be modeled using pickup functions that are directly proportional to wave shear stress. An advection/diffusion model reproduced observed profiles of sediment concentration if turbulent eddy viscosity, computed from a $k - \epsilon$ model, is multiplied by a factor of approximately 4-5 in the surf zone. The bedload model that we used assumed sheet flow condition, and was able to reproduce the observed shoreward sediment transport that occurred in the shoaling regions, during middle bar generation and stagnation. We used different calibration factors for each phase of bed evolution, which highlights the delicate balance between wave and undertow forcing. Our study showed that wave-resolved model can be used reproduce detailed observations of sediment movement in the surf zone.

3. 3. MODELING OF THE UNDERTOW

3.1 Introduction

The undertow is a weak wave-induced current, generated to compensate for the shoreward mass flux due to waves (Dyhr-Nielsen & Sørensen (1970); Dally (1980)). This current plays a major role in controlling cross-shore bathymetric variability, and more precisely offshore/shoreward sandbar migration (Dyhr-Nielsen & Sørensen (1970); Dally (1980); Thornton *et al.* (1996); Gallagher *et al.* (1998)). Near the bed, the undertow interacts with wave motion in the wave boundary layer, to generate a bottom shear stress. The shear stress, in turn, plays a key role in determining the amount of sediment that is resuspended in the water column (Fredsøe & Deigaard (1992); Nielsen (1982); van Rijn (1993); Soulsby (1997)).

In the water column, the undertow moves sediment offshore, counteracting effects of suspended flux due to waves (see e.g. Hanes & Huntley (1986); Conley & Beach (2003); Osborne & Greenwood (1992b), among others). Hence, this current is a key player in determining not only the amount of sediment that is suspended, but also the strength and direction of the suspended transport. It is therefore crucial for the success of cross-shore sediment transport models to determine accurately the vertical profile of undertow as well as its value in the proximity of the bed.

Steady state, wave-averaged undertow models are the most widely used in the mathematical modeling of coastal hydrodynamics (Christensen *et al.* (2002)). These models have achieved good results in reproducing observed undertow profiles both laboratory and field settings (Svendsen (1984b), Stive & Wind (1986), Smith & Putrevu (1992), Deigaard *et al.* (1991); Haines & Sallenger (1994); Garcez-Faria *et al.* (2000); Newberger & Allen

(2007b), among others). Such models solve the steady state, wave-averaged momentum equations to obtain the depth variation of the undertow $U(x,z)$ They are generally of the form (Dally (1980); Svendsen (1984b)):

$$\frac{\partial \bar{\tau}}{\partial z} = \frac{\partial}{\partial z}\left(\rho \nu_t \frac{\partial U(x,z)}{\partial x}\right) = F \tag{3.1}$$

where ν_t is the turbulent eddy viscosity, and F a forcing function.

Three boundary conditions are available to solve this equation for U:

1. a shear stress at the top of the domain (referred to as surface shear stress herein), which has been defined as the wave trough level (Stive & Wind (1986); Deigaard & Fredsøe (1989)), or the mean water level (Dally (1980); Stive & De Vriend (1994))
2. a shear stress at the bed (Svendsen (1984a))
3. the continuity equation, which dictates that the depth-averaged undertow is compensated by the shoreward mass flux due to waves and rollers

So, *a priori*, there should only be one solution to Equation 3.1, assuming that the eddy viscosity ν_t is known. However, a wide range of solutions exist in the literature, and they have not been reconciled.

To obtain an expression for the undertow $U(x,z)$, Equation 3.1 must be integrated twice in the vertical dimension. Whereas most models compute the forcing F from wave models (Borecki (1982); Dally & Dean (1984); Svendsen (1984b); Stive & Wind (1986)), others express F by invoking surface or bottom shear stress boundary conditions (Apostos *et al.* (2007); Tajima & Madsen (2006); Cox & Kobayashi (1997)) or the continuity equation (Apostos *et al.* (2007); Reniers *et al.* (2004)). Furthermore, most of these models assume that F is uniform with depth, and justify this depth uniformity based on the experimental evidence (for example, Nadaoka & Kondoh (1982); Stive & Wind (1982, 1986); Cox & Kobayashi (1996)), or linear long-wave theory (Svendsen (1984b); Stive & Wind

(1986); Garcez-Faria *et al.* (2000); Tajima & Madsen (2006), among others).

Once F has been defined, Equation 3.1 is integrated once, and an expression for the depth variation of the mean shear stress is obtained. To solve this equation, some models use a bottom shear stress boundary condition (e.g., Borecki (1982); Dally & Dean (1984); Svendsen (1984b)), while others use a surface shear stress (Stive & Wind (1986); Deigaard & Fredsøe (1989); Apostos *et al.* (2007)). Although Svendsen (1986) argued that bottom or surface shear stress boundary conditions should yield identical results, numerical solutions still show differences (see e.g., Garcez-Faria *et al.* (2000); Spielmann *et al.* (2004)). Moreover, among models that use the surface shear stress as a boundary condition, the exact formulation of this stress varies. For example, Garcez-Faria *et al.* (2000) used the expression of Stive & Wind (1986); Apostos *et al.* (2007) used the expression of Stive & De Vriend (1994); Rakha (1998) used the expression of Deigaard & Fredsøe (1989); Tajima & Madsen (2006) derived a new expression. These surface shear stress expressions all yielded good results of undertow profiles when each was applied to a particular dataset. However, when compared to a same set of data, the profiles of surface shear stress differ, and some of them (Stive & Wind (1986); Tajima & Madsen (2006) have erroneous physical implications (Dingemans *et al.* (1987); de Vriend & Kitou (1990)). The wide variety of solutions to Equation 3.1 might seem puzzling, considering there should be only one solution. Thus, it is important to reconcile these solutions.

In addition to the formulation of the forcing F and of the surface shear stress, another obstacle to find a solution to Equation 3.1 is the issue of turbulence closure. The eddy viscosity ν_t has been expressed using turbulence closure schemes based on wave-resolving (Rakha (1998)) or wave-averaged models (Deigaard *et al.* (1991); Newberger & Allen (2007b)). However, in general, ν_t is expressed using a parametrization based on bathymetric or wave variables (Stive & Wind (1986); Svendsen (1987); Haines & Sallenger (1994); Reniers *et al.* (2004)). Most of the parametrizations of the eddy viscosity that have been proposed in the literature have each been developed based on only one dataset,

obtained at a particular site. For example, Svendsen *et al.* (2004) used the dataset of Nadaoka & Kondoh (1982) to justify their formula, Haines & Sallenger (1994) used a dataset obtained at Duck, N.C., in 1982, and Reniers *et al.* (2004) calibrated their expression using different dataset obtained at Duck, N.C., in 1997 (even though Reniers *et al.* (2004) claim that they are developing a predictive model, they use measurements to find their forcing F_i). Such site-specific formulations have been used to estimate undertow profiles at entirely different sites (Apostos *et al.* (2007)). Existing eddy viscosity parametrizations have not been tested using a wide range of datasets to evaluate their generality.

In this paper, our purpose is to highlight discrepancies in the existing formulations of the undertow that have been developed using Linear Wave Theory (LWT) and phase-averaged models. We will explain their differences and reconcile them when possible. This paper is organized as follows. In Section 3.2, we will show that the forcing of the undertow is constant over depth. We will also arrive at the expression of surface shear stress derived by Deigaard & Fredsøe (1989). We will conduct our derivations by assuming LWT, but we will relax the assumption of shallow water waves, or linear long waves. Because recent publications have recognized the role played by mean current advective terms and bed shear stress in the forcing of the undertow (Garcez-Faria *et al.* (2000); Newberger & Allen (2007a); Apostos *et al.* (2007)), we will keep these terms in our derivation but we will assume a weak vertical variation of the undertow. In Section 3.3, we will present the measured profiles of wave height, mean water level and undertow that will be used to solve the equations presented in Section 3.2. We will show that, among all possible parametrizations of the eddy viscosity that we found in the literature, a depth-independent formulation matches our dataset the best. In Section 3.4, we will evaluate the performance of our undertow model on the datasets presented in the previous section. In Section 3.5 we will discuss our results and look at the relative importance of each term in the momentum equations that we presented. Finally, we conclude this paper in Section 3.6.

3.2 General Formulation

3.2.1 General Properties

We formulate the problem in a 2D vertical Eulerian reference system, where horizontal and vertical position (*x,z*) and velocity (*u(x,z,t),w(x,z,t)*) of water particles are described with x pointing shoreward, and z pointing upwards. Vertical origin is at the still water level (SWL), and $\eta(x,t)$ is the free water surface elevation. Partial differentiation with respect to any variable α (where α represents, for example, time or position) will sometimes be denoted by ∂_α.

We decompose horizontal and vertical velocities *u(x,z,t)* and *w(x,z,t)* into mean, wave and turbulent parts, e.g. for the horizontal velocity: $u(x,z,t) = U(x,z,t) + \widetilde{u}(x,z,t) + u'(x,z,t)$. These quantities satisfy $\overline{u} = U$, $\overline{\widetilde{u}} = 0$ and $\overline{u'} = 0$, where the overbar represents wave averaging of any function $\psi(z,x,t)$: $\overline{\psi(x,z,t)} = \frac{1}{T}\int_0^T \psi(x,z,t)\,dt$, with T the wave period. We assume that the mean velocity U is defined from the Mean Water Level (MWL) elevation, $z = \overline{\eta}$ to the bed, $z = -d$. Total water depth is represented by $h = d+\overline{\eta}$. Finally, we assume that turbulent and wave velocities are uncorrelated: $\overline{\widetilde{u}u'} = 0$.

The governing equations for inviscid unidirectional flows between $z = \eta(x,t)$, and $z = -d$ are:

$$\frac{\partial u}{\partial x} + \frac{\partial w}{\partial z} = 0 \tag{3.2}$$

$$\frac{\partial u}{\partial t} + \frac{\partial u^2}{\partial x} + \frac{\partial uw}{\partial z} = -\frac{1}{\rho}\frac{\partial p}{\partial x} \tag{3.3}$$

$$\frac{\partial w}{\partial t} + \frac{\partial uw}{\partial x} + \frac{\partial w^2}{\partial z} = -\frac{1}{\rho}\frac{\partial p}{\partial z} - g \tag{3.4}$$

where *p(x,z,t)* represents the pressure. Equation 3.2 is the continuity equation, or the conservation of mass combined with incompressibility. Equations 3.3 and 3.4 are the horizontal and vertical momentum equations. Additionally, we need free surface and

bottom kinematic boundary conditions for a sloping bottom (Dean & Dalrymple (1984)):

$$\frac{\partial \eta}{\partial t} + u\frac{\partial \eta}{\partial x} - w = 0 \text{ at } z = \eta \tag{3.5}$$

$$u\frac{\partial d}{\partial x} + w = 0 \text{ at } z = -d \tag{3.6}$$

The depth integration of the fluid density ρ multiplied by the horizontal velocity u yields an expression for the mass flux (or momentum) M^T:

$$M^T = \overline{\int_{-h}^{\eta} \rho u \, dz} = \int_{-h}^{\overline{\eta}} \rho U \, dz + \overline{\int_{\overline{\eta}}^{\eta} \rho \widetilde{u} \, dz} + \overline{\int_{\overline{\eta}}^{\eta} \rho u' \, dz} \tag{3.7}$$

or

$$M^T = M^m + M^w + M^t \tag{3.8}$$

where M^m is the mass flux (momentum) due to mean current, which, per our definition, is confined to a region between bed and MWL. M^w is the net mass flux (momentum) due to waves, and is confined to a region between MWL and free surface. Finally, M^t is the mass flux due to turbulent motion, and is also confined to a region between MWL and free surface. We will assume that this term is zero for the remainder of this paper.

To relate the mean current momentum to wave momentum, we first integrate from bed to free surface elevation the continuity equation (Equation 3.2). Next, we average it over a wave period. After invoking the kinematic free surface and bottom boundary conditions (Equations 3.5 and 3.6) we obtain another expression for the total momentum M^T:

$$\rho\frac{\partial \overline{\eta}}{\partial t} + \frac{\partial M^T}{\partial x} = 0 \tag{3.9}$$

Under steady state conditions, this last equation becomes $\partial_x M^T = 0$. Because the beach is a fixed boundary that can be considered impermeable, we write Equation 3.9 as: $M^T = Constant = 0$, which means that $M^m + M^w = 0$.

This last equation indicates that, under 2DV conditions, the net shoreward mass flux due to the waves must be returned in its entirety. In other words, from Equation 3.8, an offshore-directed current U is generated from the shoreward mass flux due to the waves (Svendsen (2006)):

$$M^w = -M^m = -\int_{-h}^{\overline{\eta}} \rho U \, dz = -\rho h U_r \tag{3.10}$$

where U_r is the depth averaged value of the undertow (defined between MWL and bed).

3.2.2 Forcing of the Undertow

General Solution

To derive an equation for the forcing of the mean current, we decompose the velocity into mean and fluctuating parts, and wave-average the horizontal momentum equation (Equation 3.3) neglecting horizontal turbulent mixing terms $\overline{u'^2}$:

$$\frac{\partial U}{\partial t} + \frac{\partial \overline{\widetilde{u}^2}}{\partial x} + \frac{\partial U^2}{\partial x} + \frac{\partial \overline{\widetilde{u}\widetilde{w}}}{\partial z} + \frac{\partial UW}{\partial z} = -\frac{1}{\rho}\frac{\partial \overline{p}}{\partial x} - \frac{\partial \overline{u'w'}}{\partial z} \tag{3.11}$$

The vertical gradient of mean turbulent shear stress ($\overline{\tau}(z) = -\partial_z \overline{u'w'}$) is expressed by the vertical mixing of horizontal mean momentum $\overline{\tau}(z) = \partial_z(\nu_t \partial_z U)$, where ν_t is an eddy viscosity coefficient representative of the turbulence level in the water column.

We also express the wave-averaged pressure by wave-averaging the vertical momentum equation (Equation 3.4), and neglecting the mixing term $\overline{w'^2}$ (Stive & Wind (1982), Svendsen (2006) Ch. 11):

$$\overline{p} = -\rho \overline{\widetilde{w}^2} - \rho W^2 + \rho g(\overline{\eta} - z) \tag{3.12}$$

Contrary to our references, this expression includes mean vertical velocity W.

Finally, following Garcez-Faria *et al.* (2000), we simplify the expression of the wave

shear stress, $\partial_z \overline{\widetilde{u}\widetilde{w}}$, by using the decomposition presented by Rivero & Arcilla (1995):

$$\frac{\partial \overline{\widetilde{u}\widetilde{w}}}{\partial z} = -\frac{1}{2}\frac{\partial}{\partial x}\left(\overline{\widetilde{u^2}} - \overline{\widetilde{w^2}}\right) + \overline{\widetilde{\omega}\widetilde{w}} \tag{3.13}$$

where $\widetilde{\omega}$ represents wave-induced vorticity. We have thus transformed Equation 3.11 into:

$$\rho\frac{\partial U}{\partial t} + \underbrace{\frac{1}{2}\frac{\partial}{\partial x}\rho\left(\overline{\widetilde{u^2}} - \overline{\widetilde{w^2}}\right) + \rho\overline{\widetilde{\omega}\widetilde{w}}}_{\text{F}} + \underbrace{\rho g\frac{\partial \overline{\eta}}{\partial x}}_{\text{P}} + \underbrace{\rho\frac{\partial U^2}{\partial x} - \rho\frac{\partial W^2}{\partial x} + \rho\frac{\partial UW}{\partial z}}_{\text{G}} = \frac{\partial \overline{\tau}}{\partial z} \tag{3.14}$$

where F is a force due to action of waves only, P is a pressure force induced by gradients in MWL, and G is a force induced by advection of mean currents. This expression is exact and can be solved with any wave theory. It necessitates two boundary conditions. In general, they consist of a mean bottom or surface shear stress, $\overline{\tau_b}$ or $\overline{\tau_s}$, and the continuity equation, Equation 3.10.

Solution Using Linear Wave Theory

To solve Equation 3.14, we will use Linear Wave Theory (LWT), but we will keep horizontal and vertical mean velocities. We first simplify the wave stress terms in Equation 3.14 to obtain (see Appendix C.2 for details):

$$\rho\frac{1}{2}\frac{\partial}{\partial x}(\overline{\widetilde{u^2}} - \overline{\widetilde{w^2}}) = \frac{\partial}{\partial x}\left(\frac{S_{xx} - E_w/2}{h}\right) \tag{3.15}$$

where, under the confines of LWT, the energy density of a Rayleigh distributed wave field is represented by $E_w = 1/8\rho g H_{rms}^2$, where $H_{rms} = \sqrt{8\overline{\eta^2}}$. S_{xx} represents the radiation stress due to waves only. The vorticity term in Equation 3.14 disappears under the assumptions of LWT.

Equation 3.15 shows that, in Equation 3.14, the combination of the wave velocity advective term $\widetilde{u}^2$, the dynamic pressure term $\widetilde{w}^2$ and the wave-induced shear stress $\overline{\widetilde{u}\widetilde{w}}$ generated a depth uniform forcing term for the undertow. This result is in line with pre-

vious experimental observations (Nadaoka & Kondoh (1982); Stive & Wind (1982, 1986)), but is valid only if one uses LWT. Using a weakly nonlinear wave theory, Zou *et al.* (2006) expressed the wave-induced vertical shear stress $\overline{\widetilde{u}\widetilde{w}}$ as a function of the bed shear stress. Such dependence on the bed shear stress causes its vertical derivative ($\partial_z \overline{\widetilde{u}\widetilde{w}}$) to become non-depth uniform.

Finally, we assume that second-order terms in W are negligible (see Appendix C.3), and rewrite Equation 3.14 as:

$$\rho\frac{\partial U}{\partial t} + \frac{\partial}{\partial x}\left(\frac{S_{xx} - E_w/2}{2h}\right) + \rho g\frac{\partial \overline{\eta}}{\partial x} + \rho\frac{\partial U^2}{\partial x} + \rho\frac{\partial UW}{\partial z} = \frac{\partial \overline{\tau}}{\partial z} \tag{3.16}$$

Equation 3.16, which reduces to the one derived by Newberger & Allen (2007a) in shallow water (see Equation B3 in Newberger & Allen (2007a)), shows that, in shoaling regions as well as in the surf zone, the undertow is forced by two depth uniform forces, F and P, and a depth-varying force G:

$$Force = \underbrace{\frac{\partial}{\partial x}\left(\frac{S_{xx} - E/2}{2h}\right)}_{\mathrm{F(x)}} + \underbrace{\rho g\frac{\partial \overline{\eta}}{\partial x}}_{\mathrm{P(x)}} + \underbrace{\left[\rho\frac{\partial U^2}{\partial x} + \rho\frac{\partial UW}{\partial z}\right]}_{\mathrm{G(x,z)}} \tag{3.17}$$

The depth uniform force F, first term on the right hand side (RHS), is due to the wave momentum flux; we will see in Section 3.2.3 that it can be expressed as a function of the total radiation stress gradient, as Newberger & Allen (2007a) also showed. The second part of the forcing P, the middle term on the RHS, is a depth uniform pressure gradient due to wave setup/setdown ($\partial_x \overline{\eta}$). The third part of the forcing G, the last term between brackets on the RHS, is a depth-varying force caused by the horizontal and vertical advection of the mean current, $U(x, z)$.

3.2.3 Boundary Conditions

To solve the wave-averaged mean current equation, Equation 3.16, two boundary conditions are necessary. The first condition is the depth-averaged continuity equation, Equation 3.10. The second condition is a boundary condition, which can either be a mean bottom shear stress condition $\overline{\tau_b}$ (Svendsen (1984b); Cox & Kobayashi (1997); Garcez-Faria *et al.* (2000)), or a mean shear stress at the MWL or at the trough level (Dally (1980); Stive & Wind (1986); Deigaard *et al.* (1991); Reniers *et al.* (2004); among others). In this section, we will first present expressions for bottom and surface shear stress that have been proposed in the literature. Next, we will use the equations presented in Section 3.2 to show that the expression of surface shear stress originally derived by Deigaard & Fredsøe (1989) can be arrived at by relaxing assumptions of shallow water linear waves.

Existing Expressions for Mean Bottom and Surface Shear Stress, $\overline{\tau_b}$ and $\overline{\tau_s}$

The mean bottom shear stress, $\overline{\tau_b} = \rho\nu_t\partial_z U_{|z_o}$, where z_o represents the bed level, is usually expressed empirically by using a friction factor (Jonsson (1966)) f_{wc}. For example, such an expression takes the form (see Nielsen (1982), or Fredsøe & Deigaard (1992), or Soulsby (1997),or Svendsen (2006) for example):

$$\overline{\tau_b} = \frac{2}{\pi}\rho f_{wc}\widetilde{u}_b U_\delta \tag{3.18}$$

where $\widetilde{u}_b$ represents the wave orbital velocity at the bed, and U_δ is the mean velocity right above the WBBL. In practice, $U_\delta = U(z = -d)$, for models which assume a slip boundary condition. The friction factor f_{wc} is a function of wave and mean current strength at the bed.

Similarly, various expressions for the surface shear stress have been suggested. One of

the first expressions of the surface shear stress was developed by Dally (1980):

$$\overline{\tau_s} = -\frac{1}{2}\frac{\partial E}{\partial x} \tag{3.19}$$

Dally (1980) derived this expression by integrating the wave-averaged horizontal momentum equation (Equation 3.14) between a level z in the water column, ($z < \overline{\eta}$), and the free water surface η. He neglected wave stress terms between MWL and free surface and assumed vertical velocity was negligible. He also assumed that all stress terms between MWL and free surface can be averaged at the MWL.

Later, Stive & Wind (1986), following Svendsen (1985) (see also Svendsen (2006), p. 613), derived an identical expression for the surface shear stress at the trough level. They integrated the momentum equation between trough level and free surface assuming shallow water conditions and a locally horizontal flat bottom. More recently, Tajima & Madsen (2006) re-evaluated the same integral that Dally (1980) evaluated, by assuming that LWT theory holds from trough to crest, and that the mean velocity is constant in that region. They arrived at an expression that differs from Equation 3.19, because it includes wave and mean current variables (for details, see Tajima & Madsen (2006)).

The expressions presented by Dally (1980), Stive & Wind (1986) and Tajima & Madsen (2006) generate a surface shear stress in regions where no occurs at the MWL. As Dingemans *et al.* (1987) and de Vriend & Kitou (1990) have argued, this outcome is physically unrealistic because, if a shear stress exists, the work done by this internal force has to generate dissipation. In the absence of wave breaking no dissipation exists and no surface shear stress.

Deigaard (1993), following the work of Deigaard & Fredsøe (1989), heuristically developed an expression for $\overline{\tau_s}$ by equating work done by the shear stress at the trough level to

wave and roller dissipation:

$$\overline{\tau_s} = \frac{D_w}{C} - \frac{\partial 2E_r}{\partial x} \tag{3.20}$$

where D_w is wave dissipation and E_r is the average roller kinetic energy (Svendsen (1984b)). Stive & De Vriend (1994) arrived at the same expression of the surface shear stress by depth-integrating the linearized momentum equation from bed to the mean water level (Stive & De Vriend (1994)). They assumed linear shallow water wave theory to express wave-induced radiation stress and neglected bottom shear stress in the depth-integrated, depth-averaged total momentum equation (see Section 3.2.3). Newberger & Allen (2007a) also arrived at the same expression by integrating the full horizontal momentum equations, nonlinear terms included, from the mean water level to the free surface. They expressed the mean surface shear stress by expanding M^w at the MWL using a Taylor expansion of the horizontal momentum equation (Equation 3.3). They also assumed linear shallow water wave theory, as well as depth uniform horizontal currents. They added the roller contribution ad-hoc.

Finally, Stive & De Vriend (1994), following the work of Nairn *et al.* (1990), argued that:

$$\overline{\tau_s} = \frac{1}{C} D_w - \frac{1}{C} \frac{\partial 2E_r C}{\partial x} \tag{3.21}$$

In this expression, Stive & De Vriend (1994) assumed that $\partial_x C << 1$ (which is consistent with the assumption of a flat bottom), and included in Equation 3.20 the dissipation that occurs between wave and roller. Deigaard (1993) (see also the Appendix of Stive & De Vriend (1994)) explained that the extra term in $\overline{\tau_s}$ in Equation 3.21, represents the exchange of mass (momentum) between wave and roller during the roller growth and decay phases. Deigaard (1993) excluded that term in his derivation of the surface shear stress.

Reniers & Battjes (1997) assumed that the equation of the surface shear stress presented by Stive & De Vriend (1994) could be used to express the dissipation of roller energy and expressed it as $D_r = C\overline{\tau_t}$, where now $\overline{\tau_t}$ represents the shear stress between

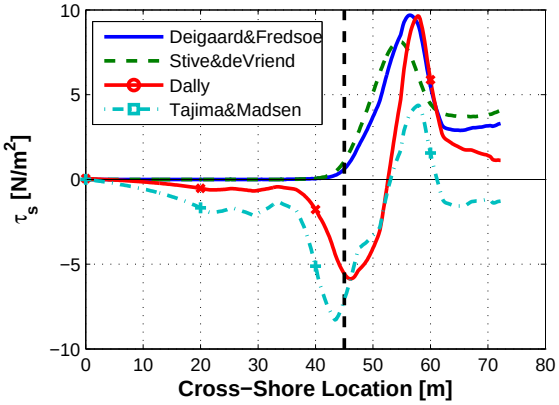

Fig. 3.1: Comparison between the various formulation of shear stress at the MWL presented in Section 3.2.3 for the SCOMAL dataset (see Section 3.3). Formulations of Deigaard (1993) and Stive & De Vriend (1994) correctly predict a relatively small, if not zero, shear stress offshore of the breaking point, a region where wave and roller dissipation should also relatively small, if not zero.

wave and roller. We have found that all expressions of surface shear stress presented so far in this section have been used to model the undertow. For example, Garcez-Faria *et al.* (2000) and Spielmann *et al.* (2004) referred to Stive & Wind (1986), Deigaard (1993) and Rakha (1998) used Equation 3.20, and Apostos *et al.* (2007) used Equation 3.21. Although the difference between Equations 3.20 and 3.21 can be considered to be relatively minor (Rakha (1998)), these expressions are not identical, and they are based on different assumptions.

For completeness, we show in Figure 3.1 comparison of surface shear stress computed from the various formulas presented in this section. This figure has been created with the SCOMAL dataset, which will be presented in Section 3.3. Only the expressions of Deigaard & Fredsøe (1989) and Stive & De Vriend (1994) generate zero shear stress in regions where dissipation does not occur. Differences between these two formulations are small.

Derivation of Surface Shear Stress

All the derivations of surface shear stress that were reviewed by us were derived assuming shallow water LWT, negligible bottom shear stress and, with the exception of Newberger and Allen (2007a), neglected the nonlinear advection terms. On the other hand, most undertow profiles that will be analyzed in this paper (see Section 3.3) were measured in intermediate waters (i.e. $kh > \pi/10$, according to LWT); waves were, in general, in shallow water for only approximately 30% of the surf zones.

To demonstrate the generality of Equation 3.20, we express the surface shear stress in this section by evaluating the time evolution of the total momentum equation (Equation 3.8), advection terms included. We do not make any assumptions about the relative water depth and do not neglect bottom shear stress in the momentum equations (Equations 3.3 and 3.4). We assume that waves are described by LWT, and we assume that higher-order horizontal currents terms are depth-uniform. This assumption is necessary in order to obtain an evolution equation for the wave momentum evolution, $\partial_t M^w$. In the remainder of this paper, we will drop the tilde over wave velocities ($\widetilde{u} = u$) and the overbar over mean shear stress ($\overline{\tau} = \tau$).

To obtain an equation for the surface shear stress, we will first obtain an evolution equation for M^T by depth-integrating the horizontal momentum equation from the bed to the free water surface. Second, we will obtain an evolution equation for M^m by depth-integrating the wave-averaged mean momentum equation (Equation 3.16), from the bed to the mean water surface. In the process, the shear stress at the MWL, τ_s, will explicitly appear. Third, we will obtain an expression for the evolution of M^w by re-arranging the various terms of the wave action equation, following the work of Smith (2006). Finally, we will use the time derivative of the depth-integrated momentum equation to equate the evolution equations of total, mean and wave momentum, $\partial_t M^T = \partial_t M^m + \partial_t M^w$, and obtain an expression for τ_s in the absence of rollers. We finally include the roller terms in the momentum equations following Svendsen (1984a) and obtain the same equation for

the surface shear stress shown in the previous section, Equation 3.20.

In the remainder of this paper, wave height will be represented by H, and wave period by T. Wave period is related to wavelength (L) and associated wavenumber ($k = 2\pi/L$), by the linear dispersion relationship, which reads, in the presence of a depth-uniform current U_o: $\sigma = U_o k + \sigma_r$, where $\sigma_r^2 = gk \tanh kh$ is the relative frequency of the wave. The wave energy density travels at the wave group velocity C_{ga}:

$$C_{ga} = nC + U_o = C_g + U_o = \frac{1}{2}\left(\frac{2kh}{\sinh 2kh} + 1\right) C + U_o \tag{3.22}$$

where the relative celerity C of the wave is:

$$C = \frac{\sqrt{gk \tanh kh}}{k} = \frac{2\pi/T - U_o k}{k} \tag{3.23}$$

.

We obtain an expression for the evolution of total momentum, $\partial_t M^T$, by wave-averaging the depth-integrated horizontal momentum equation, Equation 3.3, from $z = -d$ to $z = \overline{\eta}$ (Svendsen (2006), p.544), and by neglecting wind stress and atmospheric pressure:

$$\frac{\partial M^T}{\partial t} + \frac{\partial S_{xx}}{\partial x} + \rho g h \frac{\partial \overline{\eta}}{\partial x} + \rho \frac{\partial h U_r^2}{\partial x} + 2\frac{\partial U_r M^w}{\partial x} + \tau_b = 0 \tag{3.24}$$

Although Svendsen (2006) neglected mean vertical currents in his derivation, this assumption is not necessary to obtain Equation 3.24. In the depth integration of the horizontal momentum equation (Equation 3.3), we combine the nonlinear term containing vertical current (third term on the RHS of Equation 3.3) with the first and second terms on the RHS of the same equation. Next, after applying the Leibniz rule on the intregral, terms containing the *total* vertical velocity vanish because of the surface and bed surface boundary conditions, Equations 3.5 and 3.6 (for details, see Svendsen (2006), Equations 11.4.6 and 11.4.7). Furthermore, terms containing pressure at the free surface and at the bottom appear in the depth integration of the horizontal momentum equation.

The expression for the vertical variation of pressure is obtained from the depth integration of the vertical momentum equation, Equation 3.4. Vertical velocity appears in the expression of the pressure at the free surface, but we neglect atmospheric pressure. Vertical velocity also appears in the expression of the pressure at the bed as a shear stress term. However, we assume that neighboring water columns do not carry the weight of a column of water (see Svendsen (2006), p. 539), and the pressure at the bottom is assumed to be hydrostatic. Consequently, Equation 3.24 is consistent with our assumption that first order mean vertical currents are not neglected. We show in Appendix C.3 that second order mean vertical currents can be neglected.

To obtain an evolution equation for the mean current momentum, $\partial_t M^m$, we first integrate the wave-averaged mean momentum equation, Equation 3.16, between the bed -d and MWL $\overline{\eta}$, and invoke the Leibniz rule:

$$\frac{\partial}{\partial t}\int_{-d}^{\overline{\eta}} \rho U \, dz + h\frac{\partial}{\partial x}\left(\frac{S_{xx} - E/2}{2h}\right) + \rho g h \frac{\partial \overline{\eta}}{\partial x} + \frac{\partial}{\partial x}\int_{-d}^{\overline{\eta}} \rho U^2 \, dz + \rho U^2_{|-d}\frac{\partial d}{\partial x} - \rho \left(UW\right)_{|-d} - \rho U^2_{|\overline{\eta}}\frac{\partial \overline{\eta}}{\partial x} + \rho \left(UW\right)_{|\overline{\eta}} + \tau_b - \tau_s = 0 \tag{3.25}$$

To simplify this expression, we wave-average the kinematic boundary conditions, Equations 3.5 and 3.6, and obtain (see Hasselmann (1971), Smith (2006) and also Appendix A of Newberger & Allen (2007a)):

$$\frac{\partial \overline{\eta}}{\partial t} + U\frac{\partial \overline{\eta}}{\partial x} - W + \frac{1}{\rho}\frac{\partial M^w}{\partial x} = 0 \text{ at } z = \overline{\eta} \tag{3.26}$$

$$U\frac{\partial d}{\partial x} + W = 0 \text{ at } z = -d \tag{3.27}$$

where $M^w = E_w/C$ (Starr (1947)).

Combining Equations 3.25, 3.26 and 3.27, and assuming depth uniform currents in the

second order current terms, we obtain an equation for the mean momentum equation:

$$\frac{\partial M^m}{\partial t} + h\frac{\partial}{\partial x}\left(\frac{S_{xx} - E/2}{2h}\right) + \rho g h \frac{\partial \overline{\eta}}{\partial x} + \rho \frac{\partial h U_r^2}{\partial x} + U_r\left(\frac{\partial M^w}{\partial x} + \rho\frac{\partial \overline{\eta}}{\partial t}\right) + \tau_b - \tau_s = 0 \quad (3.28)$$

Finally, we derive the evolution equation of net wave momentum $\partial_t M^w$ from the wave action equation (Bretherton & Garrett (1968); Christoffersen & Jonsson (1980); Christoffersen (1982)), which is expressed as:

$$\frac{\partial}{\partial t}\frac{E_w}{\sigma_r} + \frac{\partial}{\partial x}\frac{E_w(C_g + U_r)}{\sigma_r} = -\frac{D_w}{\sigma_r} \quad (3.29)$$

where $\sigma_r = \sqrt{gk\tanh kh}$. In this equation, the dissipation term D_w represents the dissipation of wave energy, neglecting effects of bottom friction. Following the work of Smith (2006) (Section 2.c) and, after a few manipulations summarized in Appendix C.4, we obtain an evolution equation for the wave momentum:

$$\frac{\partial M^w}{\partial t} + \frac{\partial S_{xx}}{\partial x} - h\frac{\partial}{\partial x}\left(\frac{S_{xx} - E/2}{2h}\right) + \frac{D_w}{C} + \frac{\partial U_r M^w}{\partial x} + M^w\frac{\partial U_r}{\partial x} = 0 \quad (3.30)$$

This equation was first derived by Longuet-Higgins (1973) for waves in the absence of mean currents. It shows that the radiation stress gradient can be expressed as (1) a portion of the depth uniform forcing of the undertow F (see Equation 3.17), (2) wave dissipation, which only exists when waves are breaking, and (3) wave-current interaction terms.

We combine the evolution equations total, mean and wave momentum to generate an expression for the surface shear stress τ_s:

$$\frac{\partial M^T}{\partial t} - \frac{\partial M^w}{\partial t} - \frac{\partial M^m}{\partial t} = \rho U_r\frac{\partial \overline{\eta}}{\partial t} + \frac{D_w}{C} - \tau_s = 0 \quad (3.31)$$

which, for steady state, becomes:

$$\tau_s = D_w/C \quad (3.32)$$

where C is the relative speed of the wave with respect to the current U_r, given by Equation

3.23.

This expression is identical to the one derived by Deigaard & Fredsøe (1989), Stive & De Vriend (1994) and Newberger & Allen (2007a), in shallow water and in the absence of a roller. It shows that the dissipation of wave energy exerts a stress at the MWL. Under our assumption of depth-uniform second-order horizontal current, all non-linear terms vanish exactly, and thus have no influence on the surface stress. This finding, which differs from Tajima & Madsen (2006), is consistent with physical reasoning (Deigaard & Fredsøe (1989); de Vriend & Kitou (1990)). It shows that the work of an internal force, i.e. $\tau_s C$, only generates dissipation. Finally, this stress was derived at the MWL, and not at the trough level. The same result could not be found at the trough level following our method.

Wave dissipation is characterized by the formation of a roller, which absorbs some of the excess momentum of the waves. Hence, to complete Equation 3.32, it is necessary to account for the roller momentum flux, which we will refer to as M^r. In the absence of a formal derivation for roller momentum evolution, we used the heuristic expressions for roller momentum and roller radiation stress derived by Svendsen (1984a).

The total momentum equation thus becomes (see Svendsen (1984b) and Svendsen (2006), p.279):

$$\frac{\partial M^T}{\partial t} + \frac{\partial S_{xx}}{\partial x} + \frac{\partial R_{xx}}{\partial x} + \rho g h \frac{\partial \overline{\eta}}{\partial x} + \rho \frac{\partial h U_r^2}{\partial x} + 2\frac{\partial U_r M^w}{\partial x} + \tau_b = 0 \tag{3.33}$$

where $R_{xx} = 2E_r$. Furthermore, following Svendsen (1984a), the depth-averaged return current U_r becomes:

$$\rho h U_r = -M_T^w = -(M^w + M^r) = -(\frac{E}{C} + 2\frac{E_r}{C}) \tag{3.34}$$

where $M^r = 2E_r/C$ is the momentum of the roller, and E_r the roller energy. With this definition of U_r, we once again evaluate the time derivative of Equation 3.8, but writ-

ten as: $\partial_t M^T = \partial_t M^m + \partial_t M^w_T$. We obtain Equation 3.20 for the surface shear stress: $\tau_s = D_w/C - \partial_x 2E_r$.

Our expression for the surface shear stress exerted by breaking waves on the water column is the same as reported by Deigaard (1993). We relaxed the shallow water wave approximation, and we included bottom shear stress and mean currents. From our approach, the mean surface shear stress is expressed at the MWL, similarly to Stive & De Vriend (1994) and Newberger & Allen (2007a).

3.2.4 Solutions

We obtain the solution to the mean momentum equation and for the profile of undertow in the water column, Equation 3.16, by integrating it twice in z, and by applying either one of the boundary conditions presented in the previous section. This solution requires knowledge of the wave variables as well as eddy viscosity in the fluid. In previous publications, researchers compared the merits of applying a surface versus a bottom shear stress condition, in addition to using mass conservation (see,e.g., Spielmann *et al.* (2004); Garcez-Faria *et al.* (2000); Dally & Dean (1986)). More recently, Tajima & Madsen (2006) presented a formulation of the undertow based on the difference between surface and bottom shear stresses (i.e., $\partial_z(\tau(z)) = f(\tau_s - \tau_b)$). In this section, we examine the various possible solutions to Equation 3.16, and we show that they are all equivalent. Specifically, we show that there is no difference in a solution computed using surface shear stress or bottom shear stress as a boundary condition. We also show that the solution is similar whether one takes the difference between surface and bottom shear stress or uses the depth uniform forces F and P presented in Equation 3.16 to express the vertical variation of undertow.

First, we integrate Equation 3.16 once in z, and use the bottom shear stress boundary

condition. We obtain:

$$\tau(z) = (F+P)(z+d) + \rho\frac{\partial}{\partial x}\int_{-d}^{z} U^2\,dz - \rho U^2\frac{\partial z}{\partial x} + \rho UW + \tau_b \tag{3.35}$$

where we invoked the wave-averaged kinematic bottom boundary condition, Equation 3.27. Alternatively, when we use a mean shear stress at the MWL, the expression of the undertow reads:

$$\tau(z) = (F+P)(z-\overline{\eta}) - \rho\frac{\partial}{\partial x}\int_{z}^{\overline{\eta}} U^2\,dz - \rho U^2\frac{\partial z}{\partial x} + \rho UW - \rho U_{|\overline{\eta}}\frac{\partial M^w}{\partial x} + \tau_s \tag{3.36}$$

where we invoked the wave-averaged free surface kinematic boundary condition, Equation 3.26.

To show that these two expressions are similar, we subtract both equations, and obtain:

$$hF + hP + \rho\frac{\partial}{\partial x}\int_{-d}^{\overline{\eta}} U^2\,dz + \rho U_{|\overline{\eta}}\frac{\partial M^w}{\partial x} = \tau_s - \tau_b \tag{3.37}$$

which is the steady-state mean momentum equation for depth-varying mean currents, Equation 3.25. After we express $(F+P)$ from this equation, and insert it in Equation 3.36, we obtain a third expression for the solution to Equation 3.16:

$$\begin{aligned}\tau(z) = {} & \frac{\tau_s - \tau_b}{h}(z+d) + \tau_b - \\ & \left(\rho\frac{\partial}{\partial x}\int_{-d}^{\overline{\eta}} U^2\,dz + \rho U_{|\overline{\eta}}\frac{\partial M^w}{\partial x}\right)\frac{z+d}{h} + \rho\frac{\partial}{\partial x}\int_{-d}^{z} U^2\,dz - \rho U^2\frac{\partial z}{\partial x} + \rho UW\end{aligned} \tag{3.38}$$

Thus, the solution to the mean current equation, Equation 3.16, is the same whether one imposes a surface or a bottom shear stress boundary condition. Equations 3.35 and 3.36 yield the same expression for the mean shear stress $\tau(x,z)$, as was argued by Svendsen (1986). Additionally, comparison of Equations 3.35 3.36, and 3.38 shows that the solution is also the same if one expresses it using the depth-uniform forcing $F+P$ (Equations 3.35

and 3.36) or a difference of surface and bottom shear stresses $\tau_s - \tau_b$ (Equation 3.38).

We simplify these equations in order to compare them with the ones shown in, for example, Garcez-Faria *et al.* (2000), Spielmann *et al.* (2004) or Tajima & Madsen (2006). We once again assume that the vertical variation of second order nonlinear terms is negligible, which means that terms on the RHS of Equations 3.35, 3.36, and 3.38 are depth uniform. Under this assumption, these equations become (see Appendix C.5 for details):

$$\rho\nu_t\frac{\partial U}{\partial z} = \left[\frac{\partial}{\partial x}\left(\frac{S_{xx} - E/2}{2h}\right) + \rho g\frac{\partial\overline{\eta}}{\partial x} + \rho U_r\frac{\partial U_r}{\partial x}\right](z+d) + \tau_b \tag{3.39}$$

and

$$\rho\nu_t\frac{\partial U}{\partial z} = \left[\frac{\partial}{\partial x}\left(\frac{S_{xx} - E/2}{2h}\right) + \rho g\frac{\partial\overline{\eta}}{\partial x} + \rho U_r\frac{\partial U_r}{\partial x}\right](z-\overline{\eta}) + \tau_s \tag{3.40}$$

and

$$\rho\nu_t\frac{\partial U}{\partial z} = \frac{\tau_s - \tau_b}{h}(z+d) + \tau_b \tag{3.41}$$

The nonlinear term in Equation 3.39 or 3.40 is half the term in Garcez-Faria *et al.* (2000) because our derivation included mean vertical velocity. All non-linear terms vanished from Equation 3.41.

To summarize this section, we re-write the mean momentum equation (Equation 3.28) as (see e.g., Dingemans *et al.* (1987)):

$$\frac{\partial U_r}{\partial t} + U_r\frac{\partial U_r}{\partial x} = \underset{I}{-g\frac{\partial\overline{\eta}}{\partial x}} \underset{II}{-\left[\frac{1}{\rho}\frac{\partial}{\partial x}\left(\frac{S_{xx} - E/2}{2h}\right) - \frac{\tau_s}{\rho h}\right]} \underset{III}{-\frac{2}{h}U_r\frac{\partial M^w}{\partial x}} \underset{IV}{-\frac{\tau_b}{\rho h}} \tag{3.42}$$

Our expression for the forcing of the undertow validates the conceptual explanation presented by Dyhr-Nielsen & Sørensen (1970). The mean current is forced by four processes. The first process (term I on the RHS) is the pressure gradient induced by wave setup/setdown. The second process is a wave-induced force (term II on the RHS), which is decomposed into a portion of the depth uniform force in Equation 3.16, and another stress term which is related to the shoreward directed surface shear stress. This term is

only present when wave dissipation occurs. The third process is a wave-current interaction force (term III on the RHS), which is also a mass source/sink at the surface caused by the change in wave momentum, as pointed out by Smith (2006) and Newberger & Allen (2007a). The fourth process is caused by the bottom shear stress (term IV on the RHS).

3.3 Dataset and Wave Models

3.3.1 Dataset

To apply the undertow equations presented in Section 3.2, we used four datasets obtained under random waves. Three datasets were obtained in the laboratory (Sultan (1995), Okayasu & Katayama (1992) and Scott *et al.* (2005)) and one dataset was obtained in the field (Garcez-Faria *et al.* (1998)). Undertow profiles measured by Sultan (1995), Okayasu & Katayama (1992) and Scott *et al.* (2005) spanned the shoaling and surf regions of the flume. Undertow profiles measured by Garcez-Faria *et al.* (2000) were confined to the surf zone.

The undertow profiles collected by Sultan (1995) (referred to herein as the Sultan dataset, see Figure 3.2) were generated in a two-dimensional wave tank with glass sidewalls. The flume was 0.91 m wide and 36 m long, equipped with a hinged flap wavemaker. Water depth at the wavemaker was 0.46 m. The beach was simulated by a painted plywood 1:35 sloping surface, which occupied half of the tank. We used experimental results obtained from Sultan's spilling wave test, for which deep water wave conditions were $H_{rms} = 0.0829\,m$ and $T_p = 1.5\,s$. This random wave field was simulated using a TMA spectrum (Bouws *et al.* (1985)) with a peak enhancement factor γ of 7. Water velocity was measured using a Argon-Ion Laser Doppler Velocimeter (LDV).

The dataset collected by Okayasu & Katayama (1992) (referred to herein as the OKA dataset, see Figure 3.3) was generated in a 17 m long, 0.5 m wide and 35 cm deep wave flume. In this paper we only considered data collected during their case 3, where the beach

profile was barred, with offshore and surf zone slopes of 1/20. Random waves followed the Bretshneider-Mitsuyasu spectrum, with $H_{rms} = 3.97\,cm$ and T = 0.945 s. Water velocity was measured using an Helium-Neon LDV.

The dataset collected by Scott *et al.* (2005) (referred to herein as the SCOMAL dataset, see Figure 3.4) was generated in a 104 m long, 3.7 m wide and 4.6 m deep wave flume. Random waves ($H_o = 0.59\,m$ and $T_p = 4\,s$) were generated by a flap wavemaker using a TMA spectrum (Bouws *et al.* (1985)) with a peak enhancement factor γ of 20. Velocity was measured by three parallel stacks of Acoustic Doppler Velocimeter.

Finally, we examined the undertow profiles measured at the U.S. Army Corps of Engineers Field Research Facility at Duck, N.C., during the DUCK94 experiment (Garcez-Faria *et al.* (1998)). During this field experiment, wave height was measured at fixed cross-shore positions across the beach profile with bottom-mounted pressure sensors. Vertical profiles of total velocity were measured at a fixed cross-shore position, for approximately 1 hour at a time (1 run), by a stack electromagnetic current meters mounted on a mobile sled. Bathymetry was collected daily, and the overall area was found to be fairly longhshore uniform. For more information on wave conditions during these runs (i.e wave height and period, wave angle, tide elevations, etc.), the reader is referred to Garcez-Faria *et al.* (2000). In this paper, we will use the 8 vertical profiles of undertow (8 runs) measured on October 11, 1994 (see Figure 3.5).

3.3.2 Wave Models

To model the wave field observed during the collection of the flume dataset, we calibrated the breaking dissipation model presented by Baldock *et al.* (1998):

$$D_w = \frac{1}{4} B \rho g T \exp\left[-\left(\frac{H_b}{H} \right)^2 \right] \left(H_b^2 + H^2 \right) \tag{3.43}$$

where B is a calibration factor, and H_b was determined from the breaking parameter proposed by Ruessink *et al.* (2003a):

$$H_b = \frac{0.88}{k} \tanh\left(\frac{\gamma kh}{0.88}\right) \tag{3.44}$$

where $\gamma = 0.76kh + 0.29$. We modeled wave evolution observed at Duck with the model of Thornton & Whitford (1990) (see Church & Thornton (1993)); average values of the calibration coefficient for this model for all 8 runs were $\gamma \approx 0.35$ and $B \approx 0.05$. The model of Thornton & Whitford (1990) was chosen because it yielded smaller rms error than the model of Thornton & Guza (1983).

Roller energy was modeled according to Reniers & Battjes (1997). For the flume datasets, we calibrated the roller angle β to yield the smallest rms error between modeled and measured U_r. Depth-averaged return current U_r was estimated from measurements by fitting measured undertow profiles with a parabolic shape, and integrating the profile from the bed to the measured MWL $\overline{\eta}$. (We found percent rms errors of the order of 10% when we used cubic splines or some of the other shapes presented in Section 3.4 compared to using a parabolic shape).

We performed the calibration of the roller model by letting the roller angle β vary between 0.05 and 0.5. This sometimes led to higher errors in the estimate of the MWL elevation $\overline{\eta}$ (estimated from Equation 3.33, without bottom shear stress). For the Duck dataset, we first tried to obtain the best agreement of U_r for each run, and found that the roller angle had to vary between 0.02 and 0.8 rads. However, we could not confidently use these values, because they were found by optimizing the model based on only one value of U_r for each run. Instead, we used a fixed roller angle of $\beta = 0.1$ for all runs. Calibration coefficients B and β for the flume dataset are presented in Table 3.1.

For all datasets, we first calibrated wave and roller models from Equation 3.29 without

Table 3.1: Calibration Coefficients B and β

Dataset	B	β
Sultan	0.6	0.12
OKA	0.45	0.8
SCOMAL	1.0	0.06

Table 3.2: Percent rms error and R^2 values between modeled and measured profiles of U_r

Dataset	%rms Error	R^2
Sultan	39	0.5
OKA	40	< 0
SCOMAL	20	0.6
Duck94	31	0.5

the wave-current interaction term. We subsequently re-ran these models including wave-current interaction, but we did not change the calibration coefficients previously obtained. Comparison between profiles of wave heights, MWL and U_r, as well as profiles of measured undertow for the four dataset are presented in Figures 3.2 to 3.5. Percent rms error as well as R^2 values between measured and modeled profiles of U_r are presented in Table 3.2

3.3.3 Characteristics of Undertow Profiles

Undertow profiles exhibited a fair amount of 2DV structure for all four datasets. As shown in Figure 3.6, the undertow was strongest in the surf zone, approximately 20% shoreward of the breakpoint, near the bed. In this region, the undertow profile was convex ($\partial_z^2 U > 0$, Figures 3.2 to 3.5), i.e. stronger offshore-directed velocities (which are negative in the reference frame used throughout this paper) were observed in the lower portion of the water column. Velocities in the water column deviated from the depth-averaged value by approximately 25%, in general. One exception is the OKA dataset, for which the variation was around 50%. In the shoaling region, the undertow profile was straight or concave ($\partial_z^2 U < 0$; Figures 3.2 to 3.5). Contrary to the surf zone region, velocity at the trough level was offshore-directed and generally exceeded velocities near the bottom. In these

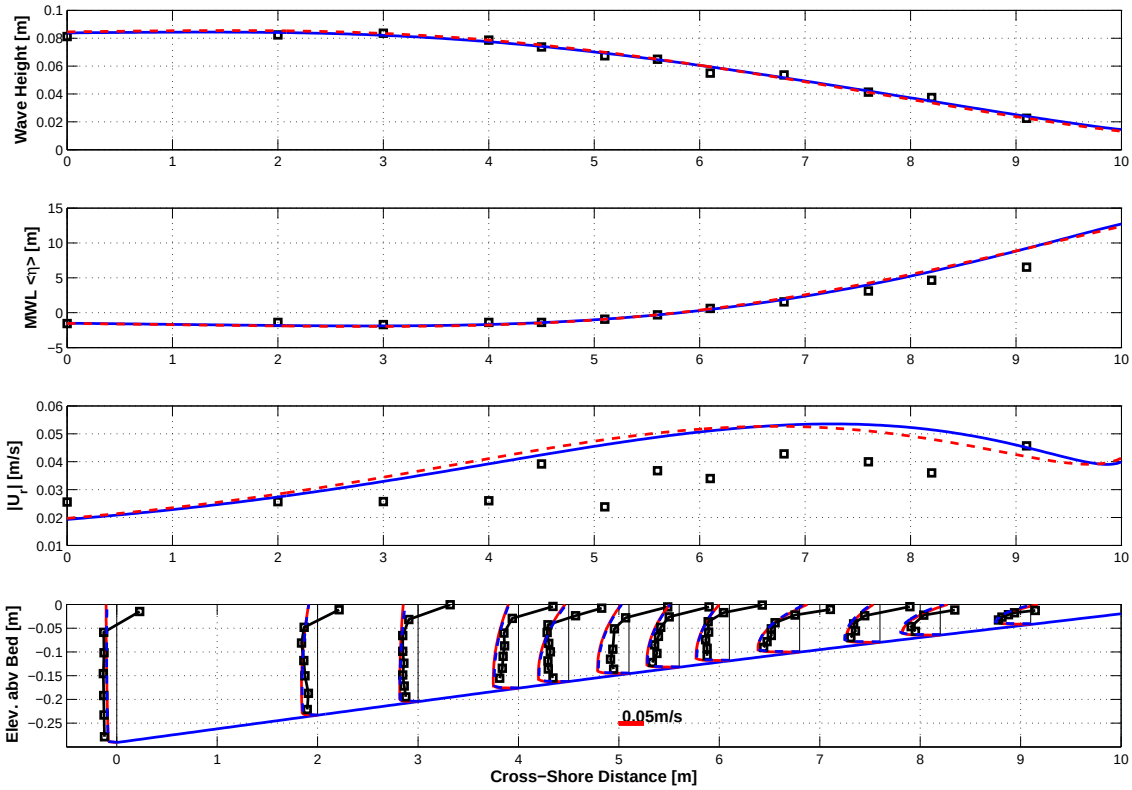

Fig. 3.2: Wave and undertow profiles for Sultan dataset. Wave height(top panel), MWL (second panel),depth-averaged return current U_r (third panel) and undertow profiles measured (squares) and modeled with the no-slip model (see Section 3.4.1), with and without wave-current interaction (dashed and solid lines)

regions, the return current measured near the trough level was sometimes as strong as the highest velocity measured in the surf zone. Closer to the bed, weak shoreward velocities (due to streaming, see Longuet-Higgins (1953)) were observed in the SCOMAL and OKA dataset.

In previous publications, undertow profiles have been found to fit parabolic shapes best (Svendsen & Hansen (1988); Stive & Wind (1986); Garcez-Faria *et al.* (2000)). Consequently, some models have been developed assuming a parabolic shape (see e.g., Cox & Kobayashi (1997); Apostos *et al.* (2007)). Such a shape is generated by assuming a constant eddy viscosity ν_t in Equation 3.16. However, other formulations for the eddy viscosity have been proposed, and each formulation yields different shapes of undertow profiles.

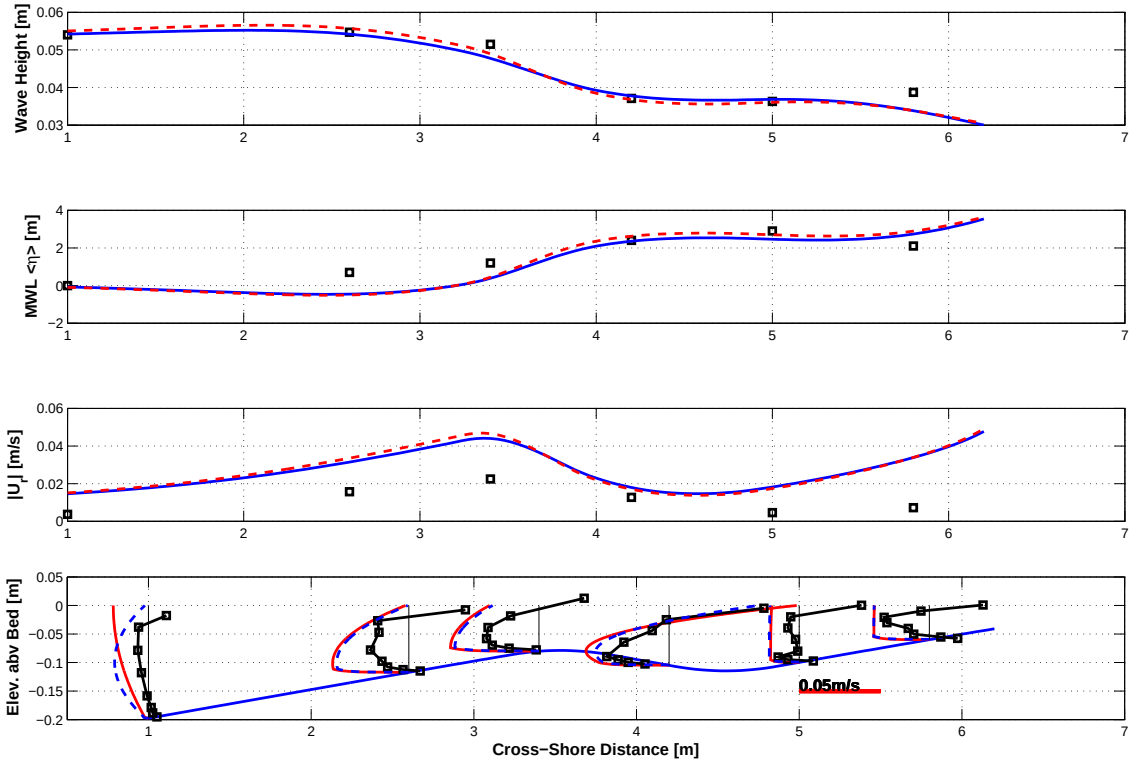

Fig. 3.3: Wave and undertow profiles for OKA dataset. Wave height(top panel), MWL (second panel),depth-averaged return current U_r (third panel) and undertow profiles measured (squares) and modeled with the no-slip model (see Section 3.4.1), with and without wave-current interaction (dashed and solid lines)

Eddy viscosity has been assumed to take multiple forms: constant (see, e.g., Stive & Wind (1986); Svendsen & Hansen (1988); Reniers *et al.* (2004)), linear (see, e.g., Okayasu *et al.* (1988); Grant & Madsen (1979)), quadratic (see e.g., Roelvink & Reniers (1994)), exponential (Svendsen (1984b)), or a function of $\sqrt{z}$ (see, e.g.,Tajima & Madsen (2006)). We analyzed which shape fits our dataset best. This exercise is important for the development of a deterministic model based on a parametric representation of the eddy viscosity. It also provides some insight into the nature of the solutions that we developed, as well as to the relevance of parametric representations.

In order to determine which formulation of eddy viscosity fits most datasets, we first developed a set of solutions to Equation 3.40 based on the various profiles of eddy viscos-

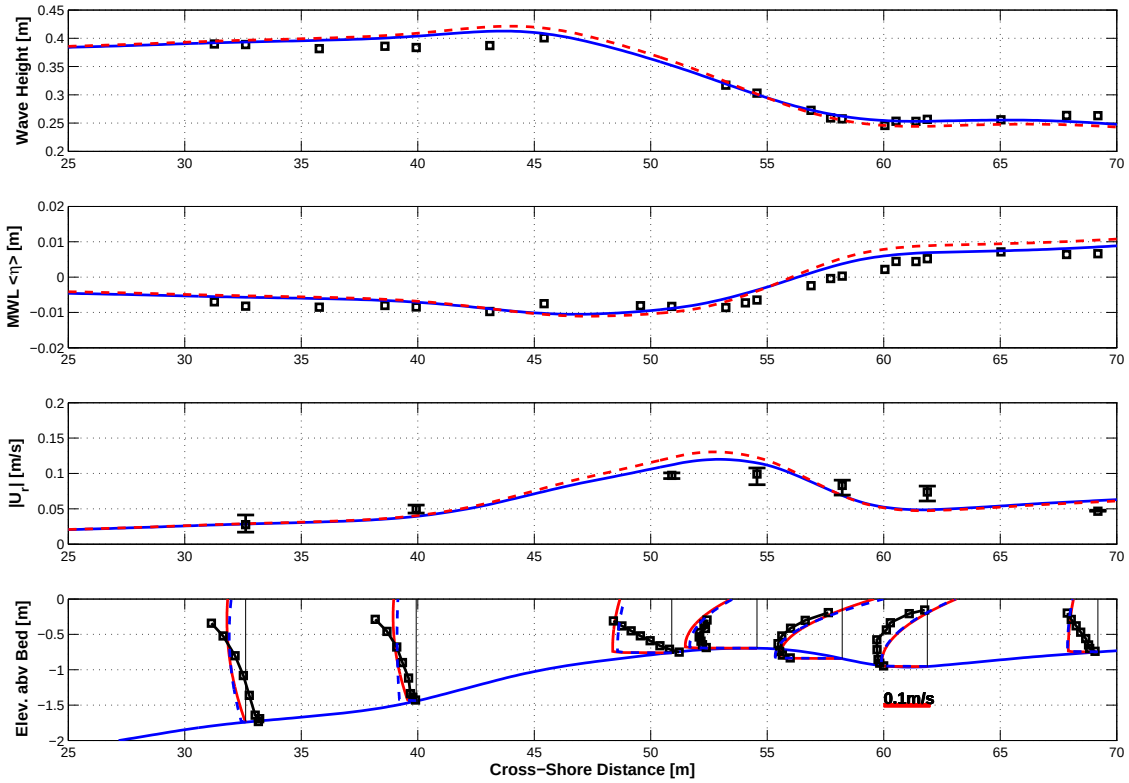

Fig. 3.4: Wave and undertow profiles for SCOMAL dataset. Wave height(top panel), MWL (second panel),depth-averaged return current U_r (third panel) and undertow profiles measured (squares) and modeled with the no-slip model (see Section 3.4.1), with and without wave-current interaction (dashed and solid lines)

ity presented above. A list of solutions is presented in Appendix C.6. Next, we used a least-square fitting technique between observed values of undertow profiles and the various theoretical solutions presented in Appendix C.6. We excluded from the dataset any measured undertow velocity above the trough level.

To estimate the goodness of fit of the least-square regression, we computed the coefficient of variation R^2 between measured and fitted undertow profiles at each cross-section:

$$R^2 = 1 - \frac{\sum_{n=1}^{N} \left(U_i^{meas} - U_i^{fit} \right)^2}{\sum_{n=1}^{N} (U_i^{meas} - < U_i >^{meas})^2} \tag{3.45}$$

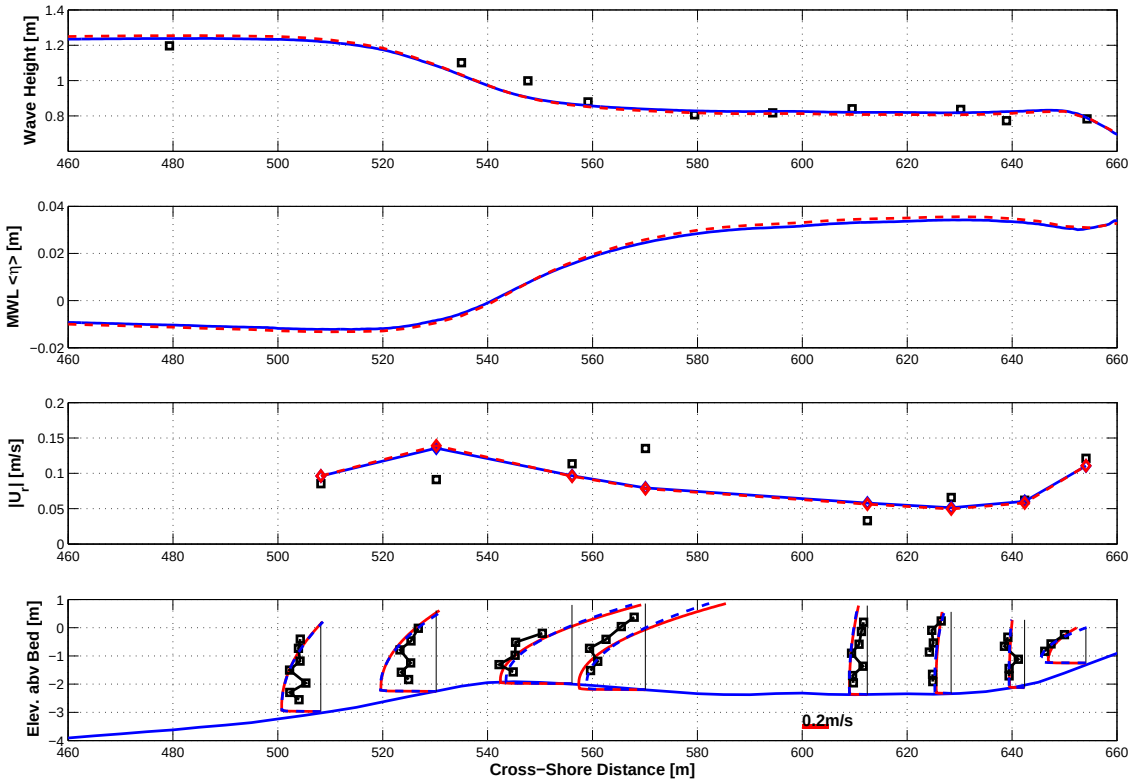

Fig. 3.5: Wave and undertow profiles for , for Run 3 of Duck dataset. Wave height(top panel), MWL (second panel),depth-averaged return current U_r (third panel) and undertow profiles measured (squares) and modeled with the no-slip model (see Section 3.4.1), with and without wave-current interaction (dashed and solid lines). MWL measurements were not available; undertow profiles plotted on top of bathymetry measured during Run 8, tide included.

where U_i^{meas} represents the discrete measurements of vertical velocity at the i^{th} cross-shore position, $< U_i >^{meas}$ is the mean value of U_i^{meas}. U_i^{fit} represents the values of fitted profile *U(z)*, for the various expressions of ν_t, at the same elevation as the measured undertow U_i^{meas}. An R^2 value of 1 represents a perfect fit. A negative R^2 value indicates that the mean value $< U_i >^{meas}$ represents the data vertical variation better than the theoretical formulation.

We performed the least-square fitting of the measured undertow profiles by imposing physically realistic values on possible combinations of ν_t and bed velocity values such that $10^{-6} \leq \nu_t \leq 0.1$, and $U_o - 0.1 \leq C \leq U_o + 0.1$. U_o is the measured at about 1 cm above the

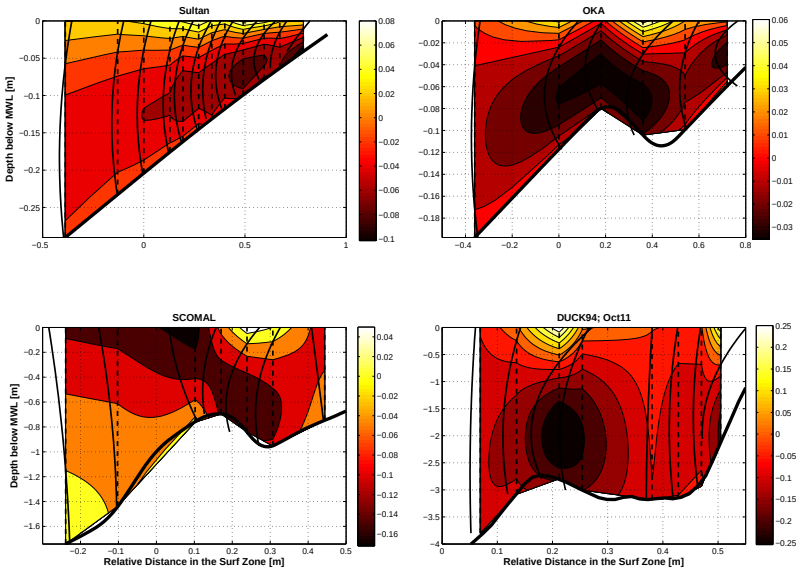

Fig. 3.6: Profiles and contour plots of undertow for the dataset of Sultan (top left panel), OKA (top right panel), SCOMAL (bottom left panel) and the data collected on October 11, during DUCK94 (bottom right panel). Warm (cool panel) colors indicate negative (positive) velocities. Undertow profiles are indicated by solid black lines, and positions of measurement (U=0) are indicated by black dashed lines. On X-axis, zero represents location of maximum wave height (breaking), and +1 represents position of the shoreline (water depth = 0).

bed, for all laboratory datasets, and at 0.4 m for the Duck dataset. Cross-shore profiles of R^2 for the three expressions of ν_t that yielded highest R^2 values are presented in Figure 3.3.3. When R^2 values were negative (i.e. analytical fit was worse than taking the vertical mean), we imposed $R^2 = 0$.

Generally, R^2 was zero in regions offshore of the breaking point. This result is expected because the forcing F is positive and cannot generate a concave profile. The solution can be linear at best, and our model represents them by taking $U(z) \approx U_r$, which means that calibrated values of ν_t might be unrealistically high. The shape of the profiles in offshore regions cannot be explained by the equations presented in this paper. Although explanations have been attempted to justify these shapes (e.g., Monismith *et al.* (2007), Lentz *et al.* (2008)), no unifying theory has been proposed. In the remainder of this paper, we

will model profiles of undertow for all observations. We will gage the relative success of our model by its performance in the surf zone.

Indeed, according to our theoretical work, formulations performed better in the surf zone, where the forcing F is positive and generates convex profiles. However, R^2 values vary widely for a given dataset, and they vary from one dataset to another. For example, a constant eddy viscosity parametrization for the Sultan dataset yielded a high R^2 value ($R^2 \approx 0.7$) at cross-shore position $X = 4$ m, and a negative R^2 value ($R^2 \approx -0.01$) at $X = 4.5$ m. This difference of R^2 values points to the fact that some profiles in a same dataset fit a certain shape, e.g. a parabola, better than other profiles. Thus, for a certain parametrization of eddy viscosity, errors will vary in the cross-shore direction. In any case, we found that, overall, the best fit were obtained by taking $\nu_t = Constant = \alpha$. This is in line with the findings others (e.g., Svendsen & Hansen (1988) or Garcez-Faria *et al.* (2000)), who tested their model on only one dataset.

3.4 Modeling Results

3.4.1 Solution for Depth-Uniform Eddy-Viscosity ν_t

We solved the equation of the undertow, Equation 3.41, by calibrating it for a constant eddy viscosity ν_t to observed values of undertow. Cross-shore variation of wave parameters (wave height, MWL, radiation stress etc.) were obtained from the wave models presented in Section 3.3. Surface shear stress was obtained from Equation 3.20, and bottom shear stress was obtained from Equation 3.18. The constant of integration was defined by solving the depth-integrated continuity equation, Equation 3.34.

We solved all momentum evolution equations, Equations 3.28, 3.29, and, 3.33 in a consistent manner, as follows. First, we solved the total momentum equation, Equation 3.33, for $\overline{\eta}$, neglecting bottom shear stress. Next, we calibrated one of the mean current

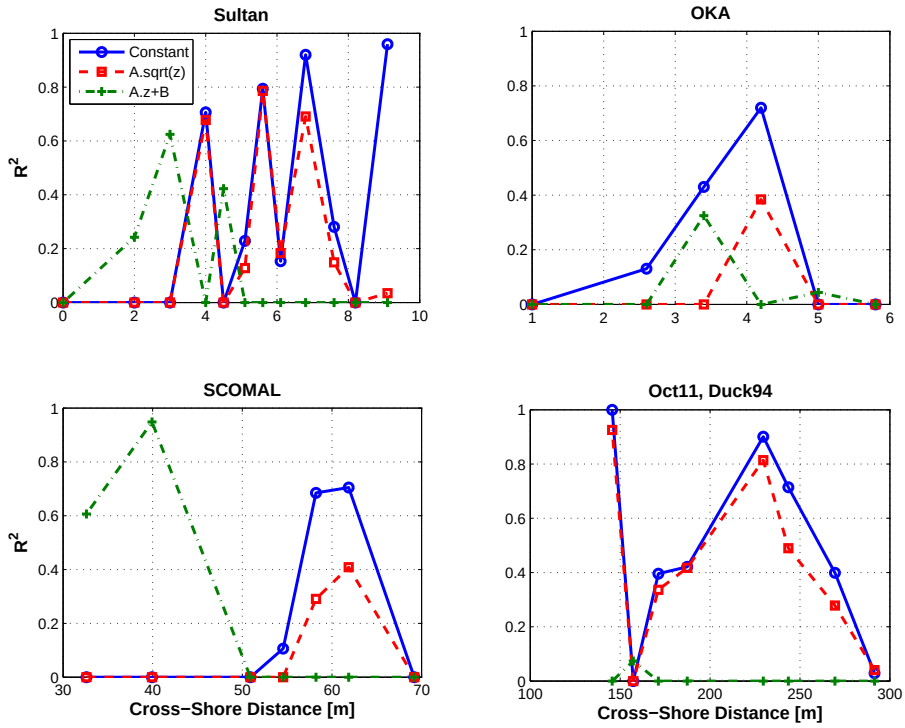

Fig. 3.7: Coefficient of determination R^2 versus relative cross-shore distance (where 0 represents location of wave breaking and 1 represents the shoreline) for three formulations of constant eddy viscosity that yielded highest R^2 values for the Sultan dataset (top left panel), OKA dataset (top right panel), SCOMAL dataset (bottom left dataset) and Duck94 dataset (bottom right panel).

equations, Equation 3.38, to find the depth-uniform eddy viscosity values that yielded lowest rms error between modeled and measured undertow profiles. During calibration, we allowed ν_t to vary between 10^{-6} and 0.1. We linearly interpolated best-fit values of eddy viscosity over the computational domain, and we iterated total momentum and mean current equations, Equations 3.38 and 3.33, to find the cross-shore distribution of *U(x,z)*, $U_\delta(x)$, and bed shear stress $\tau_b(x)$. To estimate the friction factor f_{wc} in Equation 3.18, we used the wave-current friction factor presented by Soulsby (1997). We conducted our iteration until bottom shear stress and mean velocity converged. Finally, when advection of mean currents was included (neglected) in Equations 3.38 and 3.33, we included (neglected) it in Equation 3.29.

We modeled profiles of undertow by first assuming a slip bottom boundary con-

dition (i.e., $U(z = -h) \neq 0$), and then a no-slip bottom boundary condition (i.e., $U(z = -h) = 0$). We will refer to these two models as the slip and no-slip model, respectively. For the slip model, we evaluated the bed shear stress from Equation 3.18, where U_δ is the theoretical mean velocity at the bed. For the the no-slip model, we assumed that the velocity followed a logarithmic velocity profile in the wave bottom boundary layer (WBBL), following observations by Cox *et al.* (1996). We estimated the thickness of the WBBL following Madsen (1994) and Madsen & Salles (1998) (initial values of bottom shear stress in their method were estimated by using Equation 3.18, with $f_w = 0.01$, and $U_\delta = U_r$). We computed the bottom shear stress in the no-slip model from the depth-averaged total momentum equation, Equation 3.8, following the method proposed by Tajima (1990):

$$\int_{-d}^{\overline{\eta}} \left(\int_{-d}^{z} \left[\frac{\tau_s - \tau_b}{\nu_t h}(z + d) + \frac{\tau_b}{\nu_t} \right] dz \right) dz = -M^w \tag{3.46}$$

The solution to Equation 3.38 in the no-slip model was iterated until convergence of undertow and bed shear stress is achieved.

We first solved Equations 3.28, 3.29, and, 3.33 with the slip and no-slip models, neglecting mean current advection terms. Both models yielded almost identical eddy viscosity values and undertow profiles above the BBL (Figure 3.4.1). This is in line with findings of Svendsen *et al.* (1987)). In addition, we found a 20% rms error between bottom shear stress estimated from the slip and no-slip bottom models. Bottom shear stress was strongest when estimated from the no-slip condition model (Figure 3.4.1). This indicates that the model of Madsen & Salles (1998) and Equation 3.18, with friction factors formulations of Soulsby (1997) or Nielsen (1982), permit acceptable estimations of bed shear stress. In the remainder of this paper, we will use the no-slip model.

To evaluate the importance of advective terms, we did not recalibrate the equations for wave dissipation and roller energy, but recomputed best-fit values of ν_t for each un-

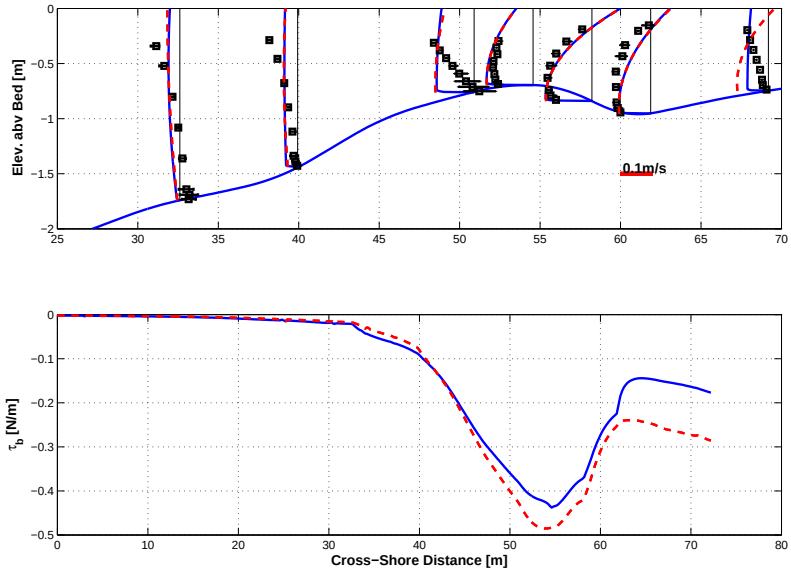

Fig. 3.8: Comparison between slip and no-slip undertow models. Top panel: Undertow profiles measured (black squares), and modeled with the no-slip model (blue solid line) and slip model (red dashed line). Profiles are plotted above the bathymetry measured during the SCOMAL experiment. Error bars in measurement indicate largest and lowest value of undertow measured accross the flume. Bottom panel: bed shear stress computed using the no-slip (solid blue line) and slip model (dashed red line).

dertow profile. Comparison between velocity profiles, with and without nonlinear terms, are presented in Figures 3.2 through 3.5. RMS error and calibration coefficient for each dataset are summarized in Table 3.3. Neither best fit ν_t values, nor modeled profiles differed greatly between the two approaches. Percent rms difference in profiles of radiation stress gradient, MWL and bed shear stress was approximately 15%. This difference is mainly reflective of the role of advection, although some of the error resulted from the the solutions to the wave-action and depth-averaged mean momentum equations.

The model performed relatively well in the surf zone, but it performed poorly in the offshore (especially for the SCOMAL dataset). This finding was expected from the results presented in Section 3.3.3. Our derivation of the forcing yields convex profiles, and the best approximation of a concave profile is a depth-uniform one, was achieved by using a high eddy viscosity. Neglecting offshore profiles, we obtained negative R^2 values for most profiles in our database. The SCOMAL dataset is an exception, where R^2 values were on average 0.6 for the convex profiles in the surf zone. If we used measured depth-average currents instead of model results, we obtained R^2 values that were on the order of 0.4 for most profiles. This indicates that the model has some skill if estimates of U_r are accurate.

Table 3.3: Best-Fit Eddy Viscosity and RMS Error for Modeled Undertow Profiles

Profile # [1]	OKA		Sultan		SCOMAL		Duck94	
	ν_t	error [cm/s]	ν_t	error [cm/s]	ν_t	error [cm/s]	ν_t	error [cm/s]
1	3.10^{-5}	1.2	9.10^{-4}	2.25	4.10^{-5}	3.14	0.1	4.2
2	1.10^{-3}	2.4	1.10^{-3}	2.1	$2.5.10^{-4}$	3	0.1	6.2
3	3.10^{-3}	2	$5.6.10^{-3}$	6.2	0.1	6.1	$5.2.10^{-2}$	4.4
4	1.10^{-4}	1.3	$2.4.10^{-3}$	1.3	$3.5.10^{-2}$	2.4	3.10^{-2}	0.1
5	9.10^{-3}	2.2	$1.6.10^{-3}$	3	2.10^{-2}	1.8	$9.6.10^{-2}$	2.5
6	0.1	3	$2.2.10^{-3}$	2	$9.8.10^{-3}$	2.7	$5.46.10^{-2}$	2.2
7	-	-	$2.4.10^{-3}$	1.1	0.1	2.8	$8.3.10^{-2}$	3
8	-	-	$2.4.10^{-3}$	3.1	-	-	$2.5.10^{-2}$	1.9
9	-	-	1.10^{-3}	2.6	-	-	-	-
10	-	-	$1.4.10^{-4}$	3.6	-	-	-	-
11	-	-	6.10^{-4}	1.9	-	-	-	-
12	-	-	3.10^{-4}	2.2.	-	-	-	-

[1]Profiles are counted from offshore to nearshore regions.

Table 3.4: R^2 values and best-fit slopes between measured and estimates of bed velocities

Estimate of U_δ^{meas}	R^2	β
U_δ^{mod}	0.20 (0.50)	1.20 (1.30)
U_r^{mod}	0.52 (0.55)	0.74 (0.75)
U_r^{meas}	0.88 (0.90)	0.87 (0.88)

Finally, we evaluated the model performance at reproducing observed velocity U_δ^{meas} on top of the boundary layer, which is used to estimate bed shear stress, Equation 3.18. The mean velocity obtained from the no-slip model, U_δ^{mod}, was compared to the observed velocity, U_δ^{meas}. We estimated U_δ^{meas} by fitting measured profiles of undertow with a parabolic formulation, and extracted the velocity at the top of the modeled boundary layer, $z = \delta$, from the fitted profile. These U_δ^{meas} values were also compared to the modeled and measured depth-averaged velocity, U_r^{mod} and U_r^{meas}. Results are presented in Figure 3.9. In general, the modeled bed velocity, U_δ^{mod} is largest for the Duck dataset, where U_δ^{meas} is strongest. R^2 and best-fit slopes β values between measured bed velocity and modeled bed velocity, U_δ^{mod}, modeled depth-averaged current, U_r^{mod} , and measured depth-average current, U_r^{meas}, are presented in Table 3.4. In this table, we also show in parenthesis the same parameters for laboratory dataset only.

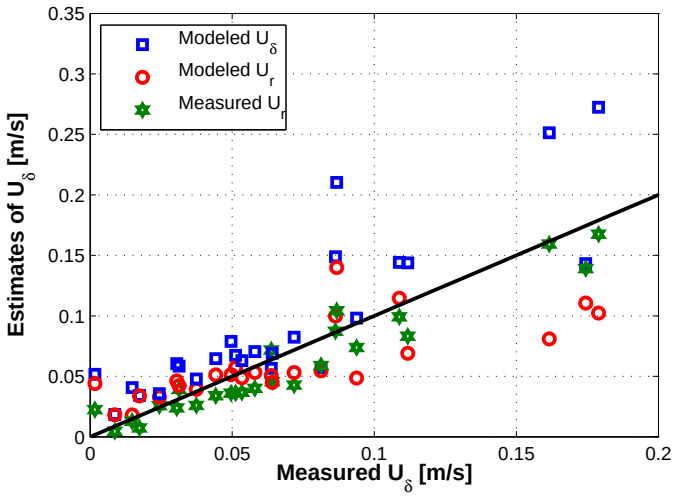

Fig. 3.9: Estimates versus measured bed velocity U_δ for all four dataset.

3.4.2 Deterministic Undertow Model

In this section, we explore the possibility of a deterministic formulation of the undertow. Such a formulation would require a specification of eddy viscosity, ν_t, which would give the same level of accuracy as the one we obtained through calibration, and thus reasonable results for many datasets. We hypothesized that, given various parametric expressions, a depth-independent eddy viscosity yields optimum modeling results. Therefore, we evaluated existing formulations of constant ν_t against our dataset. Various expressions for constant eddy viscosity are reported in the literature, including:

1. $\nu_t = A_1 h\sqrt{gh}$ (Svendsen (1987), who recommended $A_1 \approx 0.01$)
2. $\nu_t = A_1(kh)^2/\sigma(D_w/\rho)^{2/3}$ (Haines & Sallenger (1994) who recommended $A_1 = 1$)
3. $\nu_t = A_1\kappa u_o h\sqrt{f_w/2} + A_2 h(D_w/\rho)^{1/3}$, where $\kappa = 0.4$, and u_o is the wave orbital velocity at the bed (Svendsen *et al.* (2004), who recommended $A_1 \approx 0.2$, and $0.05 \leq A_2 \leq 0.1$)
4. $\nu_t = A_1\kappa h u_b^* + A_2\kappa h(D_w/\rho)^{1/3}$, where $u_b^* = \sqrt{|\tau_b|/\rho}$ (de Vriend & Stive (1987), who recommended $A_1 = A_2 = 1$)
5. $\nu_t = A_1\kappa h u_b^* + A_2\kappa h u_s^*$, where $u_s^* = \sqrt{|\tau_s|/\rho} + (D_w/\rho)^{1/3}$ (adapted from Tajima & Madsen (2006))

In all above equations, A_1 and A_2 are calibration coefficients. Ideally, these coefficients should lie in the range recommended by the authors.

To determine which of the above formulations is most appropriate for a parametric representation of eddy viscosity, we first solved the mean current equation expressed by using the difference between surface and bottom shear stress, Equation 3.41, for a wide range of eddy viscosity values: $10^{-6} \leq \nu_t \leq 0.1$. Next, we estimated the rms error between modeled and measured profiles of undertow in the surf zone for each eddy viscosity value:

$$\text{Error} = \sqrt{\frac{\sum (U_{mod} - U_{meas})^2}{\sum U_{meas}^2}} \tag{3.47}$$

where U_{mod} is the modeled undertow profile and U_{meas} is the measured profile. Lowest rms error yielded the value of the best-fit eddy viscosity.

For each formulation of ν_t listed above, we performed a least-square regression analysis to determine coefficients A_1 and/or A_2. This analysis minimized the difference between theoretical formulation and best-fit ν_t values in the surf zone, keeping A_1 and/or A_2 between 0 and 1. To improve our prediction of the calibration coefficients A_1 and A_2, we also included values of ν_t that were $\pm 10\%$ around the optimal ν_t, for each profile. The inclusion of additional points was designed to account for sources of error in our procedure, permitting us to find the optimal calibration values for eddy viscosity.

The least square fit analysis yielded negative R^2 values. Moreover, values of A_1 and A_2 proposed by Haines & Sallenger (1994), Svendsen *et al.* (2004), and de Vriend & Stive (1987) were different from the values obtained, except for the formulation of Svendsen (1987) (e.g., $\nu_t \approx 0.01h\sqrt{gh}$). Hence, although undertow profiles best fit parabolic profiles, the suggested cross-shore distributions of eddy viscosity cannot be considered to be universal.

3.5 Discussion

We have shown in this paper that, using LWT, nearly all of the formulations of undertow published are similar. Throughout our derivations, we relied on the evolution equations of total momentum (Equation 3.24), mean momentum(Equation 3.28), and wave momentum (Equation 3.29). These equations are all linked by the equation of mass conservation (Equation 3.8). Errors between solutions occur if one is not consistent in the methodology used to solve the three evolution equations. Specifically, three common types of inconsistencies have been identified:

1. Inclusion of advective terms in the depth-averaged cross-shore momentum equation (Equation 3.24) and in the mean current equation (Equation 3.16), but not in the

wave action equation, Equation 3.29.

2. Omission of the wave stress $\overline{\widetilde{u}\widetilde{w}}$ in the mean current equation (Equation 3.16), but inclusion of surface shear stress terms τ_s (Equation 3.20) in the solution.

3. Omission of bottom shear stress in wave-averaged total momentum equation.

Based on our calculations, these errors are relatively small, but they do explain some of the discrepancies between solutions found in the literature (Rakha (1998); Garcez-Faria *et al.* (2000); Spielmann *et al.* (2004)).

To evaluate the relative importance of bed shear stress and advective terms on the solution, we examined the balance of terms in the total and mean momentum equations (Equations 3.33 and 3.28) in Figures 3.10 through 3.13. These equations yielded the undertow profiles presented in Section 3.4.1. The figures also show the decomposition of radiation stress which was obtained from the wave momentum equation (Equation 3.30), and the decomposition of the surface shear stress (Equation 3.20). For convenience, we rewrite the equations of momentum evolution:

$$\frac{\partial M^T}{\partial t} + \frac{\partial S_{xx}}{\partial x} + \frac{\partial R_{xx}}{\partial x} + \rho g h \frac{\partial \overline{\eta}}{\partial x} + \rho \frac{\partial h U_r^2}{\partial x} + 2\frac{\partial U_r M^w}{\partial x} + \tau_b = 0 \tag{3.48}$$

$$\frac{\partial M^m}{\partial t} + h\frac{\partial}{\partial x}\left(\frac{S_{xx} - E/2}{2h}\right) + \rho g h \frac{\partial \overline{\eta}}{\partial x} + \rho \frac{\partial h U_r^2}{\partial x} + U_r\left(\frac{\partial M^w}{\partial x} + \rho \frac{\partial \overline{\eta}}{\partial t}\right) + \tau_b - \tau_s = 0 \tag{3.49}$$

$$\frac{\partial M^w}{\partial t} + \frac{\partial S_{xx}}{\partial x} - h\frac{\partial}{\partial x}\left(\frac{S_{xx} - E/2}{2h}\right) + \frac{D_w}{C} + \frac{\partial U_r M^w}{\partial x} + M^w \frac{\partial U_r}{\partial x} = 0 \tag{3.50}$$

We will refer to the depth-uniform force generated be radiation stress gradients in Equation 3.49, $(S_{xx} - E/2)/(2h)$, as hF or $dS_{xx}\,Unif.$

For all cases (Figures 3.10 through 3.13), analysis of balance of terms in the total momentum equation indicates that gradients in MWL ($\partial_x \overline{\eta}$) are generally counteracted by gradients in wave-induced radiation stress (dS_{xx}). Gradients in roller momentum flux (dR_{xx}) initially opposed the wave radiation stress gradient, before counteracting the pressure gradient due to $\overline{\eta}$ inside the surf zone. As expected, the action of the roller moves the point where the pressure gradient changes sign shoreward, thereby the point of maximum setdown. Furthermore, advection and bottom shear stress terms have, in general, the same relative strength, and their influence is small compared to gradients in MWL, wave- and roller-induced radiation stress. This finding was also reported by Newberger & Allen (2007b). Even though bed shear stresses are small, their effect can sometimes be important in the calculation of wave setup. Apostos *et al.* (2007) estimated that, for their dataset, neglecting bottom shear stress yielded an increase in rms error of 27% between modeled and measured setup. However it is unclear how much of the error was caused by the omission of advective terms in their model.

Analysis of the terms in the mean momentum equation indicated that the force generated by gradients in MWL, $\partial_x \overline{\eta}$ is balanced by the combined action of surface shear stress (τ_s) and the depth-uniform force hF ($dS_{xx}\,Unif$ in the figures). The relative role of the surface shear stress varies between datasets. For the Sultan dataset hF is relatively small and overwhelmed by the wave dissipation, as shown in Figure 3.10. On the other hand, for the three barred beach profiles (OKA, SCOMAL and Duck94), surface shear stress is twice as important as the depth uniform force hF. Bed shear stress and advective have the same relative strength and are relatively weak.

Finally, decomposition of the radiation stress gradient indicates that, wave dissipation is more important than hF. Also wave dissipation opposed hF right after initiation of wave breaking. Advective terms played a relatively minor role in the decomposition of the radiation stress gradient, but, in all cases, strengthened it in the surf zone. Decomposition of surface shear stress shows that roller growth ($dR_{xx} < 0$) counteracts the effects of wave

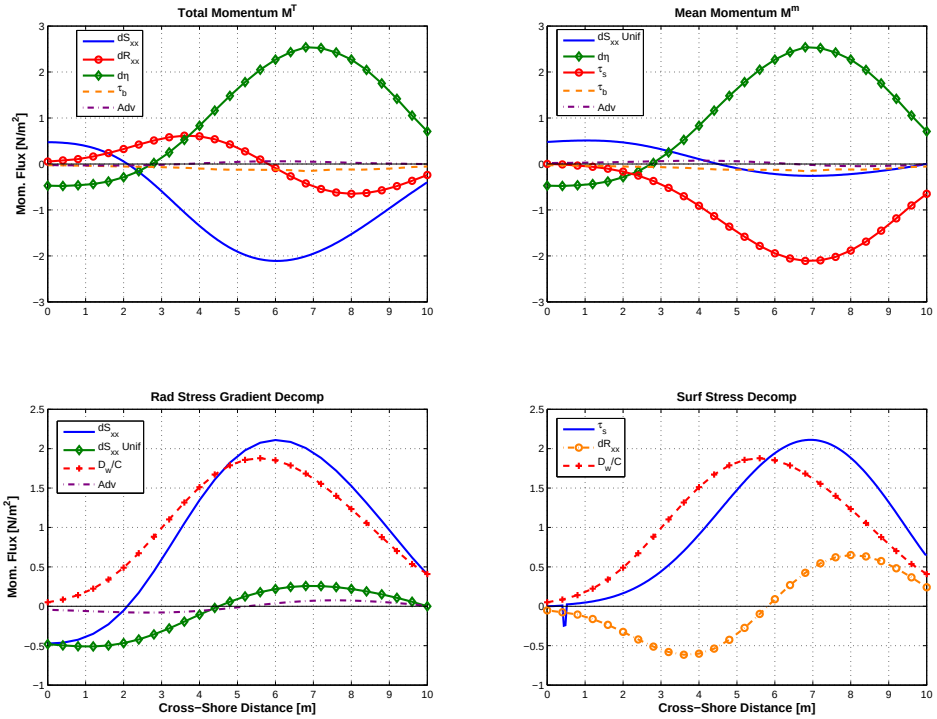

Fig. 3.10: Balance of momentum equations for Sultan dataset. Balance of terms in total momentum balance Equation 3.33(top left subplot) and in Equation 3.28 (top right subplot) versus cross-shore position; terms in the decomposition of radiation stress gradient according to Equation 3.29 (bottom left subplot) and in the decomposition of the surface shear stress according to Equation 3.20 (bottom right subplot) versus cross-shore position

dissipation, and reduces the strength of the surface shear stress. When the roller decays ($dR_{xx} > 0$), it acts in conjunction with wave dissipation to push water shoreward at the MWL. In all cases, the effect of the roller is to push the location of maximum surface shear stress shoreward and sustain the surface shear stress when wave dissipation weakens.

3.6 Conclusion

In this paper, we presented various formulations of the undertow based on LWT and obtained the expression for surface shear stress originally presented by Deigaard & Fredsøe (1989). The derivations are valid for all relative water depths, and included effects of bot-

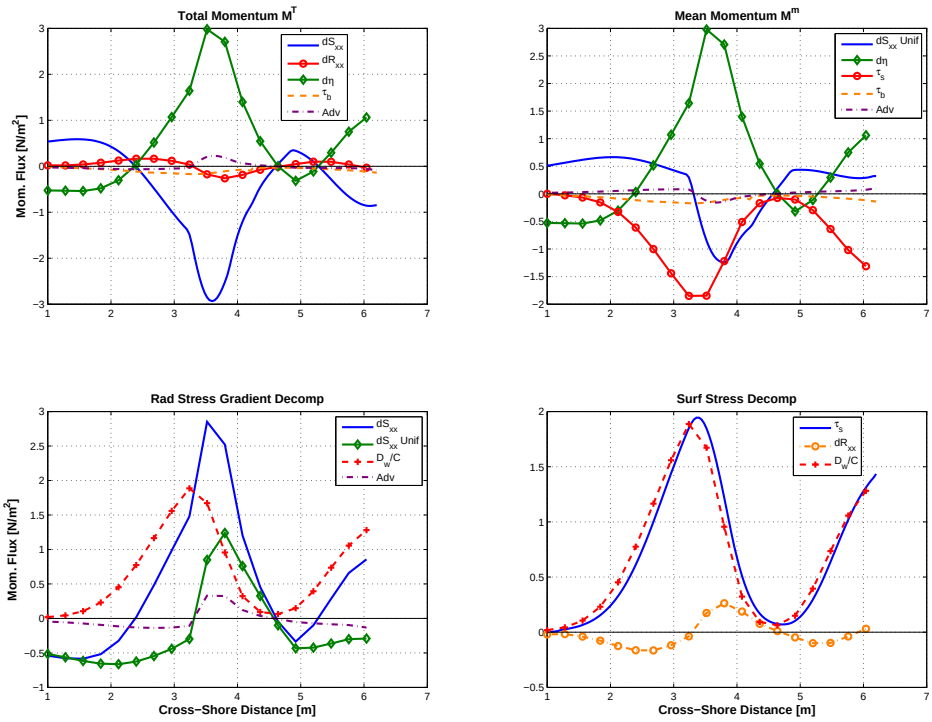

Fig. 3.11: Balance of momentum equations for OKA dataset. Balance of terms in total momentum balance Equation 3.33(top left subplot) and in Equation 3.28 (top right subplot) versus cross-shore position; terms in the decomposition of radiation stress gradient according to Equation 3.29 (bottom left subplot) and in the decomposition of the surface shear stress according to Equation 3.20 (bottom right subplot) versus cross-shore position

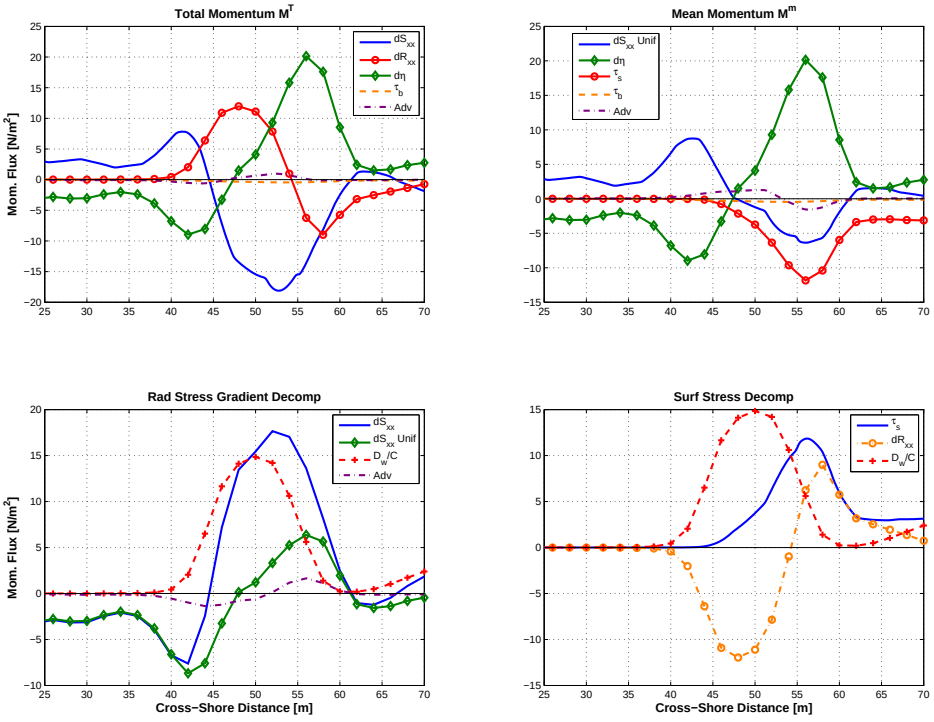

Fig. 3.12: Balance of momentum equations for SCOMAL dataset. Balance of terms in total momentum balance Equation 3.33(top left subplot) and in Equation 3.28 (top right subplot) versus cross-shore position; terms in the decomposition of radiation stress gradient according to Equation 3.29 (bottom left subplot) and in the decomposition of the surface shear stress according to Equation 3.20 (bottom right subplot) versus cross-shore position

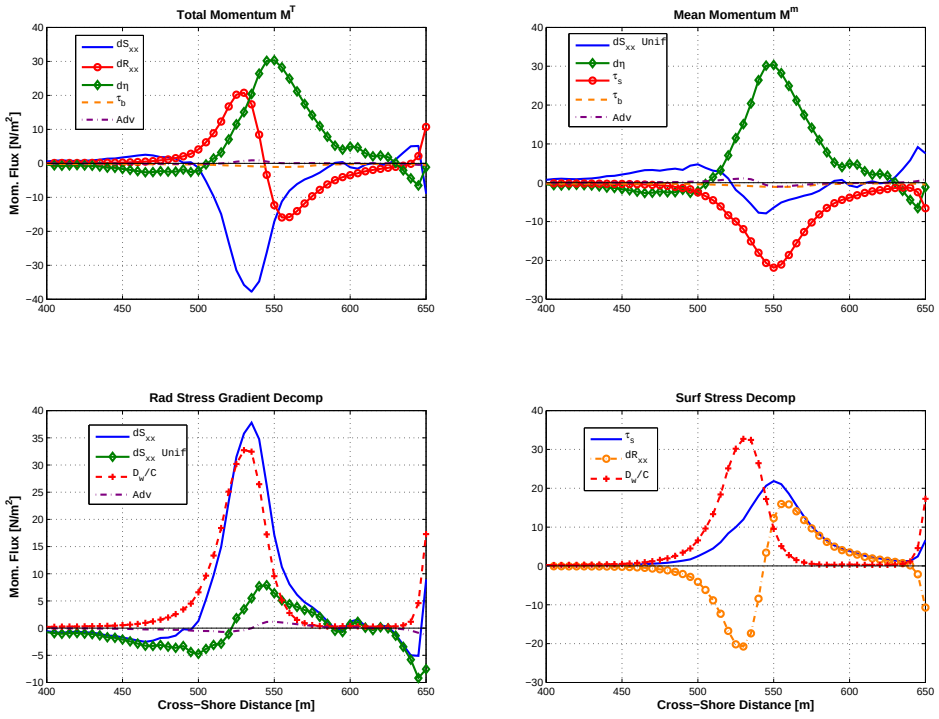

Fig. 3.13: Balance of momentum equations for Duck dataset. Balance of terms in total momentum balance Equation 3.33(top left subplot) and in Equation 3.28 (top right subplot) versus cross-shore position; terms in the decomposition of radiation stress gradient according to Equation 3.29 (bottom left subplot) and in the decomposition of the surface shear stress according to Equation 3.20 (bottom right subplot) versus cross-shore position

tom shear stress as well as mean currents. Second order mean current terms were assumed to be negligible. Under these conditions, the forcing of the mean shear stress ($\tau = \nu_t \partial_z U$) is depth-uniform, and the mean shear stress is linear. The forcing can be expressed as a function of gradients in wave velocity and MWL, or by taking the difference between surface and bottom shear stresses.

The formulations were used on four datasets (3 laboratory and 1 field dataset). After establishing that measured undertow profiles best fit a parabolic shape, and thus that using a constant eddy-viscosity would yield lowest rms error, slip and no-slip models were tested. Little difference was found in modeling results. Similarly, little difference was found when advective terms were incorporated in the model. A universal formulation for eddy viscosity could not be obtained. Future work might involve the use of turbulence closure models.

Analysis of the balance of terms in the momentum evolution equation confirmed that pressure gradient induced by variation in MWL is mainly balanced by gradients in radiation stress. Advection terms and bed shear stress are relatively weak, but have the same magnitude. Also, the surface shear stress dominates the depth-uniform force generated by wave radiation stress gradients by a factor of approximately two. Similarly, wave dissipation dominates the depth-uniform force generated by wave radiation stress gradients. Finally, the surface stress is controlled equally by wave dissipation and gradients in roller momentum flux. During their growth phase, rollers decrease the strength of the surface shear stress. During their decay phase, they increase the strength of the surface shear stress.

4. 4. GENERAL CONCLUSION

The objectives of this dissertation were to analyze in detail the modes of transport of sediment during the offshore and shoreward migration of sandbars. These observations were used to evaluate the performance of two process-based sediment transport models. Finally, based on the finding that undertow current was one of the major factors responsible for sand transport, we reconciled most formulations of undertow based on linear water wave theory, for all relative water depths.

During CrossTex, we successfully observed the generation and degeneration of two sandbars under laboratory setting. Under the action of strong undertow currents, a sandbar, which we called the offshore sandbar, was generated by the offshore movement of sediment originating from the surf zone that accumulated at or near the breakpoint. This sediment moved as suspended load, although bedload was as important. Under milder conditions, the offshore sandbar moved shoreward and degenerated. Sediment from that offshore bar moved shoreward to form another bar, which we called the middle bar. We found a strong similarity between shoreward sediment flux signal and profile of velocity asymmetry, which is closely related acceleration skewness. Sediment moved shoreward mainly as bedload, which was in the opposite direction of suspended sediment flux.

We modeled the observed transport using two process-based models. The EEM had some skill in reproducing observed sediment flux. However, this model is difficult to calibrate to match all observed phases of bed evolution. Further, the model did not represent the observed balance between low- and wave-frequency suspended sediment fluxes. Based on this finding, questions arise as to the usability of the EEM in all engineering applications. We also tested the combination of a wave-resolved eddy-diffusive suspended sediment model and a sheet-flow model on our dataset. The velocity field for these two

models was obtained through an eddy-diffusive boundary layer model. Once calibrated for the undertow, the hydrodynamic model had some skill in reproducing the velocity field in the flume. Suspended sediment flux proved difficult to model because of the inadequacy of pickup functions to represent the observed intermittent sediment concentration signal. Once calibrated with observed values of sediment concentration, and after we increased modeled values of eddy viscosity, observed and suspended sediment fluxes were similar. The bed load model reproduced the offshore and shoreward transport of sediment fairly well. Results from this effort demonstrate that detailed modeling of sediment transport is possible. However, robust models for sediment suspension and undertow are still lacking.

We investigated existing formulations of the undertow, and showed that most of these formulations are similar, regardless of the relative water depth. Assuming linear wave theory and depth-uniform mean current advection terms, the forcing of the undertow is depth-uniform. The forcing can be expressed as a function of gradients in wave radiation stress and MWL, or as the difference between surface and bottom shear stress. Further, we highlighted the generality of the expression for surface shear stress that Deigaard & Fredsøe (1989) originally derived. To investigate the possibility of a simple, robust deterministic model, we applied our model to four observed profiles of undertow. Most profiles were parabolic in shape, which would imply that a constant eddy viscosity parametrization is a sensible choice. However, none of the existing formulations for constant eddy viscosity is universal.

In summary, we have demonstrated that existing process-based models can reproduce details of observed movement of sediment in the nearshore. Also, formulations for the undertow, which is one of the main forcing responsible for sediment movement, have been presented. This research has created many opportunities for future work. First, the results of the CrossTex experiments have highlighted the need to better understand the forcing mechanism behind sediment mobilization and suspension. Furthermore, mechanisms of sediment diffusion in the water column are still unclear, and few studies looked at the re-

lationship between sediment eddy diffusivity and turbulent eddy viscosity in the surf zone. Another avenue for future work involves the formulation of an hydrodynamic model that correctly reproduces observed mean current profiles in the water column and in the wave bottom boundary layer, in a deterministic way. A possible starting point might be the deterministic 3D circulation model developed by Newberger & Allen (2007a), which achieves good results when applied to a field dataset (Newberger & Allen (2007b)). Applying this model to various datasets can yield great insights into the nature of the undertow.

BIBLIOGRAPHY

Aagaard, T., Nielsen, J. & Greenwood, B. (1998). Suspended sediment transport and nearshore bar formation on a shallow intermediate-state beach. *Marine Geology*, **148**, 203 – 225.

Apostos, A., Raubenheimer, B., Elgar, S., Guza, R. & Smith, J. (2007). Effects of wave rollers and bottom stress on wave setup. *Journal of Geophysical Research*, **112**, C02003.

Bagnold, R. (1966). An approach to the sediment transport problem from general physics. *U.S. Geological Survey Professional Paper*, **422-I**, 1–39.

Bagnold, R.A. (1963). *The Sea: Ideas and Observations, Vol. 3*, chap. Mechanics of Marine Sedimentation, 507–528. Interscience.

Bailard, J.A. (1981). An energetics total load sediment transport model for a plane sloping beach. *Journal of Geophysical Research*, **86**, 10938–10954.

Baldock, T.E., , Holmes, P., Bunker, S. & Weert, P.V. (1998). Cross-shore hydrodynamics within an unsaturated surf zone. *Coastal Engineering*, **34**, 173–196.

Bascom, W. (1953). Characteristics of natural beaches. In *Proceedings, 4th Coastal Engineering Conference*.

Beach, R. & Sternberg, R. (1991). Infragravity driven suspended sediment transport in the swash , inner and outer surf zone. In *Coastal Sediments 91*.

Beach, R.A. & Sternberg, R.W. (1988). Suspended sediment transport in the surf zone - response to cross-shore infragravity motion. *Marine Geology*, **80**, 61–79.

Beach, R.A., Sternberg, R.W. & Johnson, R. (1992). A fiber optic sensor for monitoring suspended sediment. *Marine Geology*, **103**, 513–520.

Birkemeier, W.A. (1984). Time scales of profile change. In *Proceedings, 19th International Coastal Engineering Conference*, 1507–1521, ASCE.

Black, K., Gorman, R. & Symonds, G. (1995). Sediment transport near the break point associated with cross-shore gradients in vertical eddy diffusivity. *Coastal Engineering*, **26**, 153–175.

Borecki, O. (1982). *Distribution of wave-induced momentum fluxes over depth and application within the surf-zone*. Ph.D. thesis, University of Delaware.

Bouws, E., Gunther, H., Rosenthal, W. & Vincent, C. (1985). Similarity of the wind wave spectrum in finite water depth. *Journal of Geophysical Research*, **90**, 975–986.

Bowen, A.J. (1980). Simple models of nearshore sedimentation; beach profiles and longshore bars. In S. McCann, ed., *The coastline of Canada*, 1–11, Geological Survey of Canada.

Bretherton, F.P. & Garrett, C.J.R. (1968). Wavetrains in inhomogeneous moving media. *Proceedings of the Royal Society of London. Series A, Mathematical and Physical Sciences*, **302**, 529–554.

Caálan, P.A. & Haller, M.C. (2008). Remote sensing of breaking wave phase speeds with application to non-linear depth inversions. *Coastal Engineering*, **55**, 93 – 111.

Catalán, P.A. (2005). *Hybrid approach to estimating bathymetry using remote sensing*. M.Oc.E thesis, Oregon State University.

Christensen, E.D., Walstra, D. & Emerat, N. (2002). Vertical variation of the flow accross the surf zone. *Coastal Engineering*, **45**, 169–198.

Christoffersen, J. (1982). Current depth refraction of dissipative water waves. Ser. Paper 30, Institute of Hydrodynamics and Hydraulic Engineering, Technical University of Denmark.

Christoffersen, J. & Jonsson, I. (1980). A note on wave action conservation in a dissipative current wave motion. *Appl. Ocean Res.*, **2**, 179182.

Chung, D., Grassmeijer, B. & van Rijn, L. (2000). Wave-related suspended sand transport in the ripple regime. In *Proceedings, 27th Internation Conference on Coastal Engineering*, 2836–2849, ASCE.

Church, J.C. & Thornton, E.B. (1993). Effects of breaking wave induced turbulence within a longshore current model. *Coastal Engineering*, **20**, 1–28.

Conley, D.C. & Beach, R.A. (2003). Cross-shore sediment transport partitioning in the nearshore during a storm event. *J. Geophys. Res.*, **108**, –.

Cox, D. & Kobayashi, N. (1997). Kinematic undertow model with logarithmic boundary layer. *Journal of Waterway, Port, Coastal and Ocean Engineering*, **123**, 354–360.

Cox, D.T. & Kobayashi, N. (1996). Undertow profiles in the bottom boundary layer under breaking waves. In *Proceedings, 25th International Conference on Coastal Engineering*, 3194–3206, ASCE.

Cox, D.T. & Kobayashi, N. (2000). Identification of intense, intermittent coherent motions under shoaling breaking waves. *Journal of Geophysical Research*, **105**, 14223–14236.

Cox, D.T., Kobayashi, N. & Okayasu, A. (1996). Bottom shear stress in the surf zone. *Journal of Geophysical Research*, **101(C6)**, 14,33714,348.

Dally, W. (1980). *A numerical model for beach profile evolution*. Master's thesis, Dept. of Civil Eng., University of Delaware, Newark, DE.

Dally, W. & Dean, R. (1984). Suspended sediment transport and beach profile evolution. *Journal of Waterways, Port , and Coastal Ocean Eng.*, **110**, 1533.

Dally, W. & Dean, R. (1986). Mass flux and undertow in a surf zone, by i.a. svendsen – discussion. *Coastal Engineering*, **10**, 289 – 299.

Dally, W.R. & Brown, C.A. (1995). A modeling investigation of the breaking wave roller with application to cross-shore currents. *Journal of Geophysical Research*, **100**, 24873–24883.

de Vriend, H. & Stive, M. (1987). Quasi-3d modelling of nearshore currents. *Coastal Engineering*, **11**, 565601.

de Vriend, H.J. & Kitou, N. (1990). Incorporation of wave effects in a 3d hydrostatic mean current model. In *22nd International Conference on Coastal Engineering*, ASCE, Reston, Va.

Dean, R. (1977). Equilibrium beach profiles: U.s. atlantic and gulf coasts. Ocean Engineering Report 12, University of Delaware, Department of Civil Engineering, Newark, DE.

Dean, R. & Dalrymple, R. (1984). *Water wave mechanics for engineers and scientists*, vol. 2 of *Advanced Series on Ocean Engineering*. World Sci., River Edge, N.J.

Deigaard, R. (1993). A note on the three-dimensional shear stress distribution in a surf zone. *Coastal Engineering*, **20**, 157 – 171.

Deigaard, R. & Fredsøe, J. (1989). Shear stress distribution in dissipative water waves. *Coastal Engineering*, **13**, 357–378.

Deigaard, R., P., J. & Fredse, J. (1991). Modelling of undertow by a one-equation turbulence model. *Coastal Engineering*, **15**, 431 – 458.

Dingemans, M., Radder, A. & Vriend, H.D. (1987). Computation of the driving forces of wave-induced currents. *Coastal Engineering*, **11**, 539 – 563.

Dohmen-Janssen, C. & Hanes, D. (2002). Sheet flow dynamics under monochromatic nonbreaking waves. *Journal of Geophysical Research*, **107**, 3149.

Dohmen-Janssen, C.M., Kroekenstoel, D.F., Hassan, W.N. & Ribberink, J.S. (2002). Phase lags in oscillatory sheet flow: experiments and bed load modelling. *Coastal Engineering*, **46**, 61–87.

Drake, T.G. & Calantoni, J. (2001). Discrete particle model for sheet flow sediment transport in the nearshore. *Journal of Geophysical Research*, **106**, 19859–19868.

Dyer, K. & Soulsby, R. (1988). Sand transport on the continental shelf. *Annual Review of Fluid Mechanics*, **20**, 295324.

Dyhr-Nielsen, M. & Sørensen, T. (1970). Sand transport phenomena on coasts with bars. In *12th International Conference on Coasta Engineering*, ASCE, Washington, D. C.

Elgar, S. (1987). Relationships involving third moments and bispectra of harmonic process. *IEEE Transactions on acoustics, speech and signal processing*, **ASSP-35**, 1725–1726.

Elgar, S. & Guza, R. (1985). Observation of bispectra of shoaling surface gravity waves. *Journal of Fluid Mechanics*, **167**, 425448.

Elgar, S., Guza, R.T. & Freilich, M.H. (1988). Eulerian measurements of horizontal accelerations in shoaling gravity-waves. *Journal Of Geophysical Research-Oceans*, **93**, 9261–9269.

Elgar, S., Gallagher, E.L. & Guza, R.T. (2001). Nearshore sandbar migration. *Journal of Geophysical Research*, **106**, 11623–11627.

Feddersen, F. (2007). Breaking wave induced cross-shore tracer dispersion in the surf zone: Model results and scalings. *Journal Of Geophysical Research-Oceans*, **112**.

Feddersen, F., Gallagher, E., Guza, R.T. & Elgar, S. (2003). The drag coefficient, bottom roughness and wave breaking in the nearshore. *Coastal Engineering*, **48**, 189–195.

Foster, D.L., Bowen, A.J., Holman, R.A. & Natoo, P. (2006). Field evidence of pressure gradient induced incipient motion. *Journal of Geophysical Research*, **111**.

Fredsøe, J. & Deigaard, R. (1992). *Mechanics of Coastal Sediment Transport*. World Sci.

Gallagher, E.L., Elgar, S. & Guza, R.T. (1998). Observations of sand bar evolution on a natural beach. *Journal Of Geophysical Research-Oceans*, **103**, 3203–3215.

Garcez-Faria, F., A., Thornton, E.B., Stanton, T.P., Soares, C.V. & Lippmann, T.C. (1998). Vertical profiles of longshore currents and related bed shear stress and bottom roughness. *Journal of Geophysical Research*, **103**, 3217 3232.

Garcez-Faria, A.F., Thornton, E.B., Lippmann, T.C. & Stanton, T.P. (2000). Undertow over a barred beach. *Journal of Geophysical Research*, **105**, 16999–17010.

Glenn, S. & Grant, W. (1987). A suspended sediment stratification correction for combined wave and current flows. *Journal of Geophysical Research*, **92**, 82448264.

Goring, D.G. & Nikora, V.I. (2002). Despiking acoustic doppler velocimeter data. *Journal Of Hydraulic Engineering-Asce*, **128**, 117–126.

Grant, W. & Madsen, O. (1979). Combined wave and current interaction with a rough bottom. *Journal Of Geophysical Research-Oceans*, **84**, 17971808.

Green, M. & Vincent, C. (1990). Wave entrainment of sand from a rippled bed. In *Proceedings, 22nd Conference on Coastal Engineering*, 22002212, ASCE.

Haines, J.H. & Sallenger, A. (1994). Vertical structure of mean cross-shore currents across a barred surf zone. *Journal of Geophysical Research*, **99**, 14223–14242.

Hanes, D. & Huntley, D. (1986). Continuous measurements of suspended sand concentration in a wave dominated nearshre environment. *Continental Shelf Research*, **6**, 585–596.

Hasselmann, K. (1971). On the mass and momentum transfer between short gravity waves and larger-scale-motions. *Journal of Fluid Mechanics*, **50**, 189–205.

Henderson, S.M., Allen, J. & Newberger, P. (2004). Nearshore sandbar migration predicted by and eddy-diffusieve boundary layer method. *Journal of Geophysical Research*, **109**, C06024.

Hoefel, F. & Elgar, S. (2003). Wave induced sediment transport and sandbar migration. *Science*, **299**, 1885–1887.

Holman, R., Bowen, T., Dalrymple, T., Dean, B., Elgar, S., Flick, R., Freilich, M., Guza, B., Hanes, D., Kirby, J., Madsen, O., Sternberg, R. & Svendsen, I. (1989). Nearshore processes research. In *Status Report: Nearshore Processes Workshop*.

Holman, R.A. & Stanley, J. (2007). The history and technical capabilities of argus. *Coastal Engineering*, **54**, 477–491.

Hsu, T. & Liu, P. (2004). Toward modeling turbulent suspension of sand in the nearshore. *Journal Of Geophysical Research-Oceans*, **109**, doi:10.1029/2003JC002240.

Hsu, T.J. & Hanes, D.M. (2004). Effects of wave shape on sheet flow sediment transport. *Journal Of Geophysical Research-Oceans*, **109**, C05025.

Hsu, T.J., Elgar, S. & Guza, R. (2006). Wave-induced sediment transport and onshore sandbar migration. *Coastal Engineering*, **53**, 817–824.

Huntley, D. & Hanes, D. (1987). Direct measurement of suspended sediment transport. In *Coastal Sediment 87*, 723 737, ASCE.

Jaffe, B. & Rubin, D. (1996). Using nonlinear forecasting to learn the magnitude and phasing of time-varying sediment suspension in the surf-zone. *Journal Of Geophysical Research-Oceans*, **101**, 14283–14296.

Jaffe, B., Sternberg, R. & Sallenger, A. (1984). The role of suspended sediment in shore-normal beach profile changes. In *Proceedings, 19th International Conference on Coastal Engineering*, 19831996, ASCE.

Janssen, C.M., W. N., H., R. V. D., W. & J. S., R. (1997). Grain-size influence on sand transport mechanisms. In *Proceedings, Coastal Dynamics97*, 58 67, Am. Soc. Civ. Eng., Reston, Va.

Jonsson, I. (1966). Wave boundary layers and friction factors. In *Proceedings, 10th International Conference on Coastal Engineering*, 109–152, ASCE.

Keulegan, ., G.H. (1945). Depths of offshore bars. Engineering Notes 8, Beach Erosion Board,, U.S. Army Engineer Waterways Experiment Station, Vicksburg, Mississippi, USA.

Keulegan, G. (1948). An experimental study of submarine sand bars. Technical Report 8, Beach Erosion Board, U.S. Army Engineer Waterways Experiment Station, Vicksburg, Mississippi, USA.

King, D.B. (1990). *Studies in oscillatory flow bed load sediment transport*. Ph.D. thesis, Univ. of Calif., San Diego.

Kobayashi, N., Zhao, H. & Tega, Y. (2005). Suspended sand transport in surf zones. *Journal of Geophysical Research*, **110**.

Komar, P. (1998). *Beach processes and sedimentation*. Prentice Hall, second edition edn.

Kraus, N.C. & Smith, J.M. (1994). Supertank laboratory data collection, volumes 1 and 2. Technical Report CERC-94-3, US Army Corps of Engineers, Vicksburg, MS.

Lee, G., Dade, W.B., Friedricks, C.T. & Vincent, C.E. (2004). Examination of reference concentration under waves and currents on the inner shelf. *Journal Of Geophysical Research-Oceans*, **109**, C02021.

Lees, B. (1981). Relationship between eddy viscosity of seawater and eddy diffusivity of suspended particles. *Geo-Marine Letters*, **1 (34)**, 249254.

Lentz, S.J., Fewings, M., Howd, P., Fredericks, J. & Hathaway, K. (2008). Observations and a model of undertow over the inner continental shelf. *Journal of Physical Oceanography*, **38**, 2341–2357.

Lippmann, T.C. & Holman, R.A. (1990). The spatial and temporal variability of sand bar morphology. *Journal of Geophysical Research*, **95**, 11575–11590.

Longuet-Higgins, M.S. (1953). Mass transport in water waves. *Proc. R. Soc. London A*, **245**, 535–581.

Longuet-Higgins, M.S. (1973). The mechanics of the surf zone. In E. Becker & G.K. Mikhilov, eds., *Proc., 13th Int. Congress of Theor. & Appl. Mech.*, Springer-Verlag.

Longuet-Higgins, M.S. & Stewart, R. (1962). Radiation stress and mass transport in gravity waves, with application to surf beats. *Journal of Fluid Mechanics*, **13**, 481–503.

Longuet-Higgins, M.S. & Stewart, R. (1964). Radiation stresses in water waves; a physical discussion with applications. *Deep Sea Research*, **11**, 529–562.

Madsen, O.S. (1994). Spectral wave-current bottom boundary layer flows. In V. ASCE Reston, ed., *Proc., 24th Int. Conf. on Coastal Engineering*, 384398.

Madsen, O.S. & Salles, P. (1998). Eddy viscosity models for wave boundary layers. In *Proceedings of the 26th International Conference on Coastal Engineering*, 26152627, ASCE.

Magalen, J. (2006). *A laboratory experiment of sandbar migration with comparison to recent models*. Master's thesis, Oregon State University.

Marino-Tapia, I.J., Russell, P.E., OHare, T.J., Davidson, M.A. & Huntley, D.A. (2007). Cross-shore sediment transport on natural beaches and its relation to sandbar migration patterns: 1. field observations and derivation of a transport parameterization. *Journal Of Geophysical Research-Oceans*, **223**.

McLachlan, A., Jaramillo, E., Donn, T.E. & Wessels, F. (1993). Sandy beach macrofauna communities and their control by the physical environment: A geographical comparison. *Journal of Coastal Research*, **15**, 27 38.

Mei, C.C. (1989). *The Applied Dynamics of Ocean Surface Waves*, vol. 1 of *Advanced Series on Ocean Engineering*. World Scientific.

Meyer-Peter, E. & Müller, R. (1948). Formulas for bed-load transport. In *Proc., IAHR, Stockholm*.

Miller, J., Haller, M. & Magalen, J. (2006). Design of large scale experiments on onshore bar migration. In *Ocean-Sciences*, Am. Geoph. Union, Hawaii, poster Presentation.

Monismith, S.G., Cowen, E.A., Nepf, H.M., Magnaudet, J. & Thais, L. (2007). Laboratory observations of mean flows under surface gravity waves. *Journal of Fluid Mechanics*, **573**, 131147.

Nadaoka, K. & Kondoh, T. (1982). Laboratory measurements of velocity field structure in the surf zone by ldv. In *Coastal Engineering in Japan*, vol. 25, 125145.

Nairn, R.B., Roelvink, J. & Southgate, H.N. (1990). Transition zone with and implications for modelling surfzone hydrodynamics. In *Proceedings, 22th International Conference on Coastal Engr.*, 68–81, ASCE.

Newberger, P. & Allen, J. (2007a). Forcing a three-dimensional, hydrostatic, primitive-equation model for application in the surf zone: 1. formulation. *Journal of Geophysical Research*, **112**.

Newberger, P. & Allen, J. (2007b). Forcing a three-dimensional, hydrostatic, primitive-equation model for application in the surf zone: 2. application to duck94. *Journal of Geophysical Research*, **112**.

Nielsen, P. (1982). *Coastal Bottom Boundary Layers and Sediment Transport*, vol. 4 of *Advanced Series on Ocean Engineering*. World Sci.

Nielsen, P. & Callaghan, D. (2003). Shear stress and sediment transport calculations for sheet flow under waves. *Coastal Engineering*, **47 (3)**, 347354.

Nielsen, P., van der Wal, K. & Gillan, L. (2002). Vertical fluxes of sediment in oscillatory sheet flow. *Coastal Engineering*, **45**, 61 – 68.

Ogston, A. & Sternberg, R. (2002). Effect of wave breaking on sediment eddy diffusivity, suspended-sediment and longshore sediment flux profiles in the surf zone. *Continental Shelf Research*, **22**, 633655.

Okayasu, A. & Katayama, H. (1992). Distribution of undertow and long-wave component velocity due to random waves. In *Proc., 23rd International Conference on Coastal Engineering*, ASCE.

Okayasu, A., Shibayama, T. & Horikawa, K. (1988). Vertical variation of undertow in surf zone. In *Proceedings, 21st international Conference on Coastal Engineering*, ASCE.

Osborne, P. & Greenwood, B. (1992a). Frequency dependent cross-shore suspended sediment transport. 2. a non-barred shoreface. *Marine Geology*, **106**, 25–51.

Osborne, P.D. & Greenwood, B. (1992b). Frequency dependent cross-shore suspended sediment transport. 2. a barred shoreface. *Marine Geology*, **106**, 25 – 51.

Phillips, O. (1977). *The dynamics of the upper ocean (2nd ed.)*. Cambridge University Press.

Plant, N.G., Frielich, M.H. & Holman, R. (2001). Role of morphologic feedback in surf zone sandbar response. *Journal of Geophysical Research*, **106**, 973–989.

Pope, S.B. (2000). *Turbulent Flows*. Cambridge Univ. Press, New York.

Rakha, K.A. (1998). A quasi-3d phase-resolving hydrodynamic and sediment transport model. *Coastal Engineering*, **34**, 277 – 311.

Reniers, A. & Battjes, J. (1997). A laboratory study of longshore currents over barred and non-barred beaches. *Coastal Engineering*, **30**, 1–22.

Reniers, A.J.H.M., Thornton, E.B., Stanton, T.P. & Roelvink, J.A. (2004). Vertical flow structure during Sandy Duck: observations and modeling. *Coastal Engineering*, **51**, 237–260.

Ribberink, J. & Al-Salem, A. (1995). Sheet flow and suspension of sand in oscillatory boundary layers. *Coastal Engineering*, **25**, 205 – 225.

Ribberink, J.S. (1998). Bed-load transport for steady flows and unsteady oscillatory flows. *Coastal Engineering*, **34**, 59 – 82.

Ribberink, J.S. & Al-Salem, A.A. (1994). Sediment transport in oscillatory boundary layers in cases of rippled beds and sheet flow. *Journal Of Geophysical Research-Oceans*, **99**, 707 12,727.

Ribberink, J.S., Dohmen-Janssen, C.M., Hanes, D.M., McLean, S.R. & Vincent, C. (2000). Near-bed sand transport mechanisms under waves: a large scale flume experiment (sistex99). In *Proceedings, 27th International Conference on Coastal Engineering*, ASCE.

Rivero, F.J. & Arcilla, A.S. (1995). On the vertical distribution of ¡uw¿. *Coastal Engineering*, **25**, 137 – 152.

Roelvink, J.A. & Brøker, I. (1993). Cross-shore profile models. *Coastal Engineering*, **21**, 163–191.

Roelvink, J.A. & Reniers, A.J.H.M. (1994). Upgrading of a quasi-3d hydrodynamic model. In *Mast-II Overall Workshop*, Gregynog, Wales, U. K.

Roelvink, J.A. & Reniers, A.J.H.M. (1995). Lip 11d delta ume experiments: a dataset for prole evolution model validation. Technical Report H2130, Delft University of Hydraulics.

Ross, W. (2003). Sandbar presents deadly challenge. *The Register Guard (Eugene, OR)*.

Ruessink, B. & Kroon, A. (1994). The behaviour of a multiple bar system in the nearshore zone of terschelling, the netherlands: 1965-1993. *Marine Geology*, **121**, 187 – 197.

Ruessink, B., Houwman, K. & Hoekstra, P. (1998). The systematic contribution of transporting mechanisms to the cross-shore sediment transport in water depths of 3 to 9 m. *Marine Geology*, **152**, 295324.

Ruessink, B.G. & Kuriyama, Y. (2008). Numerical predictability experiments of cross-shore sandbar migration. *Geophysical Reseach Letters*, **35**.

Ruessink, B.G., Walstra, D.J.R. & Southgate, H.N. (2003a). Calibration and verification of a parametric wave model on barred beaches. *Coastal Engineering*, **48**, 139–149.

Ruessink, B.G., Wijnberg, K.M., Holman, R.A., Kuriyama, Y. & van Enckevort, I.M.J. (2003b). Intersite comparison of interanual nearshore bar behavior. *Journal of Geophysical Research*, **108**, 3249.

Scott, C.P., Cox, D.T., Maddux, T.B. & Long, J.W. (2005). Large-scale laboratory observations of turbulence on a fixed barred beach. *Measurement Science and Technology*, **16**, 1903–1912.

Sheng, J. & Hay, A. (1995). Sediment eddy diffusivities in the nearshore zone, from multifrequency acoustic backscatter. *Continental Shelf Research*, **15**, 129–147.

Shepard, F. (1950). Beach cycles in southern california. Tech. Rep. 20, Beach Erosion Board, U.S. Army Corps of Engineers.

Smith, G. & Mocke, G. (1993). Sediment suspension by turbulence in the surf zone. In M. Belorgey, R. Rajaona & J. Sleath, eds., *Sediment Transport Mechanisms in Coastal Environments and Rivers, Euromech 310*, 375 387, World Scientific.

Smith, I.S., J.K. & Putrevu, U. (1992). Vertical structure of the nearshore current at delilah: Measured and modeled. In *Proceedings, 23rd Internation Conference on Coastal Engineering*, ASCE.

Smith, J.A. (2006). Wavecurrent interactions in finite depth. *Journal of Physical Oceanography*, **36**, 14031419.

Smith, J.D. (1977). Modeling of sediment transport on continental shelves. In *The Sea*, vol. 6, 539577, Wiley-Interscience, New York.

Smith, J.D. & McLean, S. (1977). Spatially averaged flow over a wavy surface. *Journal Of Geophysical Research-Oceans*, **82**, 1735 1746.

Soulsby, R. (1997). *Dynamics of Marine Sands*. Thomas Telford.

Soulsby, R.L. & Damgaard, J.S. (2005a). Bedload sediment transport in coastal waters. *Coastal Engineering*, **52**, 673 – 689.

Soulsby, R.L. & Damgaard, J.S. (2005b). Bedload sediment transport in coastal waters. *Coastal Engineering*, **52**, 673–689.

Spielmann, K., Astruc, D. & Thual, O. (2004). Analysis of some key parametrizations in a beach profile morphodynamical model. *Coastal Engineering*, **51**, 1021 – 1049.

Starr, V. (1947). A momentum integral for surface waves in deep water. *Journal of Marine Research*, **6**.

Stive, M.J. & De Vriend, H.J. (1994). Shear stresses and mean flow in shoaling and breaking waves. In *Proceedings, 24th International Conference on Coastal Engr.*, 594–608, ASCE.

Stive, M.J.F. & Wind, H. (1986). Cross-shore mean flow in the surf zone. *Coastal Engineering*, **10**, 325–340.

Stive, M.J.F. & Wind, H.G. (1982). A study of radiation stress and set-up in the nearshore region. *Coastal Engineering*, **6**, 125.

Sultan, N.J. (1995). *Irregular Wave Kinematic in the Surf Zone*. Ph.D. thesis, Texas A&M University.

Sumer, B.M., Kozakiewicz, A., Fredsoe, J. & Deigaard, R. (1996). Velocity and concentration profiles in sheet-flow layer of movable bed. *Journal of Hydraulic Engineering*, **122**, 549–558.

Svendsen, I. (1985). On the formulation of the cross-shore wave-current problem. In *Proc., European Workshop on Coastal Zone*, Greece.

Svendsen, I. (1986). Mass flux and undertow in a surf zone, by i.a. svendsen – reply. *Coastal Engineering*, **10**, 299 – 307.

Svendsen, I., Haas, K. & Zhao, Q. (2004). *Quasi-3D Nearshore Circulation Model SHORECIRC, Version 2.0*. Research Report, Center for Applied Coastal Research, University of Delaware, Newark, DE 19716 U.S.A.

Svendsen, I.A. (1984a). Mass flux and undertow in the surf zone. *Coastal Engineering*, **8**, 347–365.

Svendsen, I.A. (1984b). Wave heights and set-up in a surf zone. *Coastal Engineering*, **8**, 303–329.

Svendsen, I.A. (1987). Analysis of surf zone turbulence. *Journal of Geophysical Research*, **92**, 5115–5124.

Svendsen, I.A. (2006). *Introduction to nearshore hydrodynamics*, vol. 24 of *Advanced Series on Ocean Engineering*. World Sci., River Edge, N.J.

Svendsen, I.A. & Hansen, J.B. (1988). Cross-shore currents in surf-zone modelling. *Coastal Engineering*, **12**, 2342.

Svendsen, I.A., Schäffer, H.A. & Hansen, J.B. (1987). The interaction between the undertow and the boundary layer flow on a beach. *Journal of Geophysical Research*, **92**, 11845–11856.

Tajima, Y. (1990). *Waves, Currents, and sediment transport in the surf zone along long, straight beaches*. Ph.D. thesis, Massachussets Institute of Technology and Woods Hole Oceanographic Institution.

Tajima, Y. & Madsen, O.S. (2006). Modeling near-shore waves, surface rollers, and undertow velocity profiles. *Journal of Waterway, Port, Coastal, and Ocean Engineering*, **132**, 429–438.

Thorne, P., Williams, J. & Davies, A. (2002). Suspended sediments under waves measured in a large-scale flume facility. *Journal of Geophysical Research*, **107**, 3178.

Thorne, P., Davies, A. & Bell, P. (2009). Observations and analysis of sediment diffusivity profiles over sandy rippled beds under waves. *Journal of Geophysical Research*, **114**, 1–16.

Thornton, E.B. & Guza, R.T. (1983). Transformation of wave height distribution. *Journal of Geophysical Research*, **88**, 5925–5938.

Thornton, E.B. & Whitford, D.J. (1990). Longshore currents over a barred beach: Part ii, model. Tech. rep., Nav. Postgrad. School, Monterey, Calif.

Thornton, E.B., Humiston, R.T. & Birkemeier, W. (1996). Bar/trough generation on a natural beach. *Journal Of Geophysical Research-Oceans*, **101**, 12097–12110.

Trowbridge, J. & Young, D. (1989). Sand transport by unbroken water waves under sheet flow conditions. *Journal of Geophysical Research*, **94**, 10,971–10,991.

van der Werf, J.J., Schretlen, J., Ribberink, J. & O'Donoghue, T. (2009). Database of full-scale laboratory experiments on wave-driven sand transport processes. *Coastal Engineering*, **56**, 726732.

van Rijn, L. (1984). Sediment pick-up functions. *J. Hydraul. Eng.*, **110**, 1494 1502.

van Rijn, L. (1993). *Principles of sediment transport in rivers, estuaries and coastal seas*. Aqua Publications.

van Rijn, L. (2006). Unified view of sediment transport by currents and waves ii: Suspended transport. *Journal of Hydraulic Engineering*, **133**, 668–689.

Wang, P., Ebersole, B.A., Smith, E. & Johnson, B. (2002). Temporal and spatial variations of surf-zone currents and suspended sediment concentration. *Coastal Engineering*, **46**, 175211.

Watanabe, A. & Sato, S. (2004). A sheet flow transport rate formula asymmetric forward leaning waves and currents. In *Proceedings, 29th International Conference on Coastal Engineering*, 17031714, ASCE, World Scientific.

Wright, L., Boon, J., Kim, S. & List, J. (1991). Modes of cross-shore sediment transport on the shoreface of the middle atlantic bight. *Marine Geology*, **96**, 1951.

Wright, L.D. & Short, A.D. (1984). Morphodynamic variability of surf zones and beaches: A synthesis. *Marine Geology*, **56**, 93–118.

Zala Flores, N. & Sleath, J. (1998). Mobile layer in oscillatory sheet flow. *Journal of Geophysical Research*, **103 (C6)**, 12783 12793.

Zou, Q., Bowen, A.J. & Hay, A.E. (2006). Vertical distribution of wave shear stress in variable water depth: Theory and field observations. *Journal of Geophysical Research*, **111**.

APPENDIX

B.1 Mobilization and Advection/Diffusion of Suspended Sediment

Sediment that is activated at a certain depth can move as bedload, or can be put in suspension if conditions are dynamic enough (van Rijn (2006). Once ejected from the bed by the action of waves and currents, suspended sediment can follow many paths in the water column. It can fall due to the action of gravity, or be advected vertically or horizontally by fluid motions. It can also be diffused upward because of the presence of a concentration gradient (Nielsen (1982)). In general, sediment concentration is modeled by the advection/diffusion equation presented in Section 2.5.2, Equation 2.13. In this equation, ϵ_f represents sediment eddy diffusivity, which is controlled by wave-induced, bed- or surface-generated turbulence (Nielsen (1982); Smith & Mocke (1993); van Rijn (1993)), or vortex motions originating from vortex ripples (when they are present, Chung *et al.* (2000)).

In the absence of horizontal advection, sediment is mainly advected/diffused upwards. This translates into a high correlation between concentration values measured by vertically adjacent sensors. Therefore, we computed the correlation between signals measured by adjacent FOBS sensors from 0.8 to 17 cmab (i.e., correlation between 1st and 2nd, 2nd and 3rd sensors, etc.). We also computed the correlation between sensor at 0.8 cmab and all other sensors above (i.e., correlation between 1st sensor and 2nd, 1st and 3rd, etc.) to assess how much of the sediment suspended above the bed made its way up the water column.

Profiles of correlation between FOBS sensors are presented in Figure B.1. We created these profiles by averaging all correlation values above the 95% significance level at the same cross-shore location, for a certain phase of bar evolution. We also show in this figure the average slope of the correlation profiles computed at fixed cross-shore locations. A high (low) slope value indicates that correlation values were fairly variable (constant) between time series along the stack of FOBS sensors, and variable (constant) correlation values between times series of sediment concentration indicates that signals are (are not) affected by external sources, such as a plume of sediment horizontally advected within a small or large portion of the water column.

During offshore bar generation, all signals were correlated with adjacent records, and with the signal measured at 0.8 cmab, above the 95% significance level. Correlation profiles peak near the trough, where strongest suspended sediment flux and sediment load were observed. They decreased in the surf zone. From this, we infer that sediment concentration time series exhibited the same characteristics from the bed up to at least 17 cmab. This is confirmed by the low slope of correlation profiles, which also reaches a minimum at the trough.

During middle bar generation and stagnation, 98% of adjacent signals were correlated above the significance level. Correlation levels are, in general, smaller than during offshore bar generation, but they increase steadily in the surf zone. In the surf zone, the relatively high correlation between adjacent sensors, and the low slope of correlation profiles, suggests that sediment concentration signals were fairly similar in the water column. The lower correlation and higher slope values observed in the shoaling regions implies that, al-

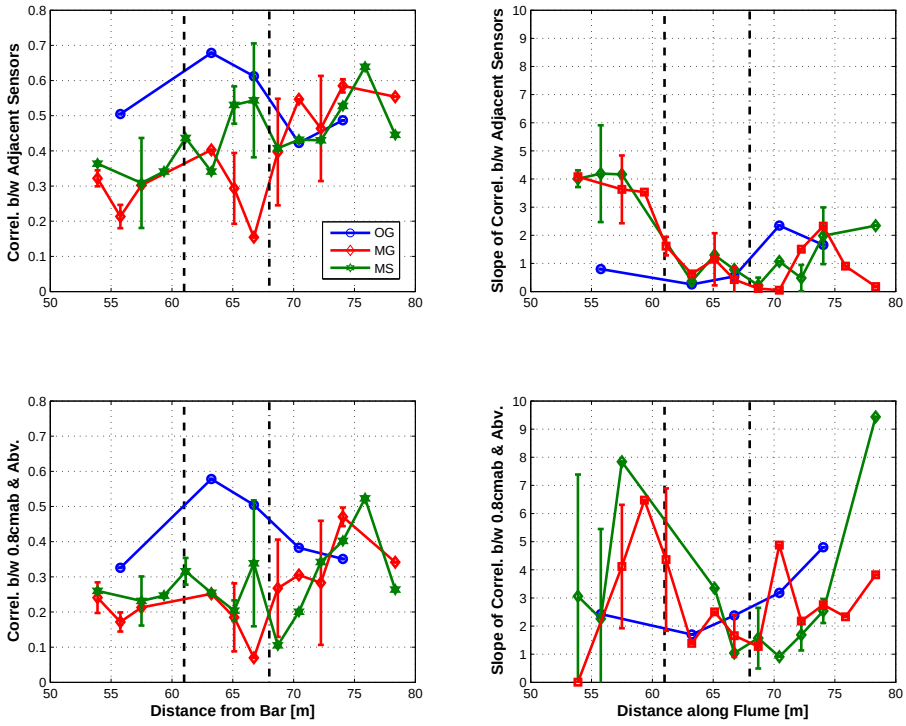

Fig. B.1: Top left panel:mean correlation between signals measured by adjacent sensors. Top right panel:average slope of vertical profile of correlation between signals measured by adjacent sensors. Bottom left panel: Mean correlation between signals measured at 0.8 cmab and sensors above. Bottom right panel:average slope of vertical profile of correlation between signals measured at 0.8 cmab and sensors above. Values computed for offshore bar generation are in blue, values for middle bar generation are in red, and for middle bar stagnation in green. Dashed and dashed dotted lines represent average location of offshore and middle bars, respectively.

though sediment suspension signals had some commonality, there was also a fair amount of variability in sediment concentration in the water column.

Also during middle bar generation and stagnation, correlation levels between sensors in the water column and the one at 0.8 cmab are lower than correlation level between adjacent sensors,and the slope of correlation level is also higher. Additionally, less than 50% of the signals measured offshore of the middle bar were correlated with the signal measured at 0.8 cmab above the 95% significance level. However, the correlation level increases in the surf zone, and more than 60% of the signals measured in in the surf zone were correlated with the signal measured at 0.8 cmab above the 95% significance level. This suggest that, as observed in Section 2.4.1, some of the sediment suspended in the lower portion of the water column did not get advected/diffused upwards, especially in offshore regions. However, more sediment suspended at 0.8 cmab made its way up the water column in regions of highest total suspended sediment tranport, i.e. in the surf zone, than in regions where suspended sediment transport was low.

Overall, offshore of the bars, signals at two different sensors sometimes did not see the same event, or were affected by the presence of sediment coming from another location. On the other hand, in the surf zone and close to the bars (in the breaking region), resuspension events were measured by most sensors in the water column, and there was little pollution from sediment coming from other regions. Additionally, for middle bar generation and stagnation, correlation between sensor at 0.8 cmab and those above was weaker than correlation between adjacent sensors. This indicates that some of the suspended sediment remained in the lower portion of the water column, and was not diffused/advected as far up as during offshore bar generation. This is further illustrated by the fact that the slope of correlation between sensors at 0.8cmab and those above is higher than the slope of correlation between adjacent sensors.

Based on these observations, it is reasonable to assume that, in the surf zone, the bed responded to wave and current action by ejecting plumes of sediment that were diffused/advected vertically fairly high up into the water column. This is especially the case for region where suspended sediment load and transport are highest. Also, it is reasonable to assume that horizontal advection of sand was probably important in offshore regions, but can be neglected in surf zone and breaking regions. Consequently, we will neglect horizontal advection in the remainder of this section.

To evaluate the role of vertical advection, we time-average Equation 2.16 and rewrite it as:

$$\overline{W_w C_w} - w_o \overline{C} = \epsilon_f \frac{\partial \overline{C}}{\partial z} \tag{B.1}$$

where W_w and C_w represent the demeaned and low-passed filtered (turbulence excluded) vertical velocity and sediment concentration time series. We will solve this equation for ϵ_f, with and without the vertical advection terms $\overline{W_w C_w}$. If estimates of eddy diffusivity after both calculation, it means that vertical advection plays a relatively small role.

Because the quality of vertical velocity measurements was often poor, W_w time series

were approximated using linear water wave theory (Sheng & Hay (1995)):

$$W_w = \frac{1}{C}\frac{\partial U_w}{\partial t} z \tag{B.2}$$

where U_w represents measured wave velocity measured by ADV, and C represents the phase velocity of the waves.

Observed profiles are not smooth, especially in regions of highest suspended load, where vertical advection/diffusion is more important. To obtain an expression for sediment concentration C, we fitted observed mean sediment concentration profiles to various existing theoretical expressions (see Soulsby (1997), p.131), namely, after dropping the bar over C:

$$C(z) = \begin{cases} C_o e^{-z/l} & \text{(Exponential profile)} \\ C_o \left[\frac{z}{z_o}\frac{h-z_o}{h-z}\right]^{-b} & \text{(Rouse profile)} \\ C_o \left(\frac{z}{z_o}\right)^{-b} & \text{(Power profile)} \end{cases}$$

In the exponential profile, l is a decay length scale (Nielsen (1982); Soulsby (1997)). In the Rouse and power profiles, h is the water depth, z_o a reference height above the seabed where the reference concentration C_o is defined (we take $z_o = 0.8$ cmab herein), and b is a suspension parameter (Soulsby (1997)):

$$b = \frac{w_o}{\kappa u_*} \tag{B.3}$$

with u_* the friction velocity, and $\kappa = 0.4$ the von Karman constant.

The exponential profile was observed when sediment was being resuspended by vortex shedding over rippled beds (Nielsen (1982); Ribberink & Al-Salem (1994)). The Rouse profile was originally derived for flows in rivers or channels, but has been used to explain profiles of suspended sediment measured under waves (Soulsby (1997)). The power-law profile was derived by Smith (1977) has been observed in the field and in the laboratory (Dohmen-Janssen & Hanes (2002); Sumer *et al.* (1996); Ribberink & Al-Salem (1995); Lee *et al.* (2004), and is indicative of sheet flow conditions (Soulsby (1997)). Under the assumption of a pure diffusive process, Rouse profiles yield a parabolic eddy diffusivity variation, and a power profile yield a linear one. We note that other formulations exist, but they tend to describe the mean sediment concentration profile as a sum of various profiles in the water column (see e.g., van Rijn (1984); Glenn & Grant (1987), Soulsby (1997)).

We fitted our measured profiles with the distributions presented in Equation B.3, computed values of the coefficient of determination R^2 for each profile:

$$R^2 = 1 - \frac{\sum_{n=1}^{N}\left(C_i^{meas} - C_i^{fit}\right)^2}{\sum_{n=1}^{N}(C_i^{meas} - < C_i >^{meas})^2} \tag{B.4}$$

where C_i^{meas} represents the discrete measurements of mean sediment concentration at the i^{th} cross-shore position, $< C_i >^{meas}$ is the mean value of C_i^{meas}. C_i^{fit} represents the values of fitted profile *C(z)*, for the various expressions of ν_t, at the same elevation as the measured undertow C_i^{meas}. An R^2 value of 1 means perfect fit, i.e. theoretical formulation matches exactly measured profile. A negative R^2 value indicates that the mean value $< c_i >^{meas}$ represents the vertical variation of the data better than the theoretical formulation. We fitted the measured profile with theoretical values between $z_o = 0.8$ to $z = 17$ cmab. We also performed the same operation with $z_o = 1.8$ cmab and $z_o = 5$ cmab but did not notice any significant change in the results. Consequently, we will use $z_o = 0.8$ cmab in the remainder of this paper.

The exponential profile did not fit our observations very well ($R^2 < 0$ for all datasets but 5), but the Rouse and power profiles performed equally well ($R^2 \geq 0.9$ during phases 'OG' and 'MS', $R^2 \approx 0.7$ in the surf zone and $R^2 \approx 0.5$ for all profiles). In view of the similar performance of both Rouse and power profiles, we decided to evaluate Equation B.1 by fitting measured mean sediment concentration profiles with a power-law profile, because they are more suitable for nearshore environments than Rouse profiles (Soulsby (1997)). We note, in passing, that the poor performance of the exponential fit, and the good performance of the power profile indicate that sheet flow conditions probably dominated during the experiment, and the ripples observed did not contribute to sediment transport.

We solved Equation B.1 for eddy diffusivity ϵ_f, with and without vertical advection, and rms error between the two profiles of ϵ_f is presented in Figure B.1. In general, rms error is less than 10%, which suggests that the role of vertical advection is relatively small. We also estimated that, when compared to a purely diffusive process, vertical advection generally accounted for less than 20% of the total value of the sediment eddy diffusivity. Consequently, we deduce that suspended sediment was mainly diffused upwards in the breaking and surf zone regions; vertical and horizontal advection played a smaller role.

Depth-averaged values of eddy diffusivity are presented in Figure B.1. Because the role of vertical advection was limited, profiles of $\epsilon_f(z)$ were fairly linear, and depth-averaged values are also an indication of the slope of the profiles. In general, eddy diffusivity are higher in the surf zone than in offshore regions. We also notice that, especially during middle bar generation and stagnation, ϵ_f steadily increases in the surf zone to reach a maximum near the shoreline. Also, eddy diffusivity values are of the same order of magnitude as eddy viscosity in the surf zone, but one to two order of magnitude larger than typical eddy viscosity values in shoaling regions. However, we can not fully trust values obtained in the offshore regions, as horizontal advection might have played a role.

In the surf zone ($X \geq 65\,m$) values of eddy diffusivity obtained in this section are, on average, 4 to 6 times higher than eddy viscosity computed with the $k - \epsilon$ model.

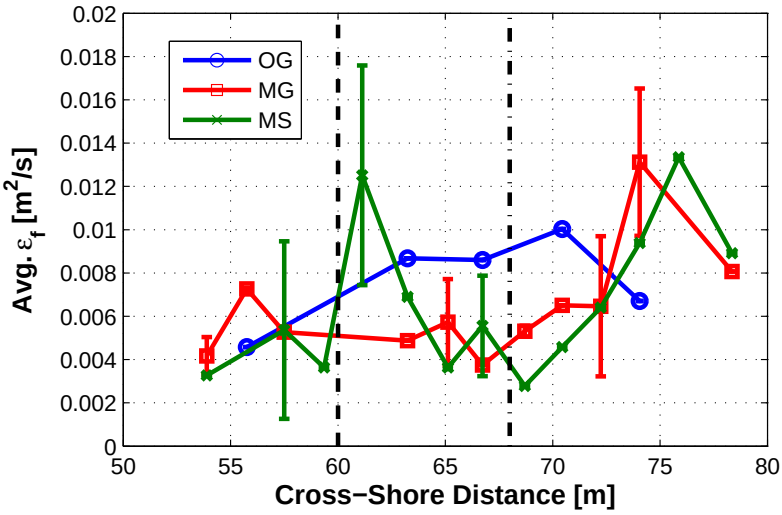

Fig. B.2: Depth-averaged eddy diffusivity during offshore bar generation ('OG'), middle bar generation ('MG') and middle bar stagnation ('MS').

C.2 Simplification of Wave Stress Terms

Consistent with LWT, we assume that the flow is irrotational, which means that $\widetilde{\omega} = 0$. We decompose the vertical derivative of $\widetilde{\overline{u}}\widetilde{\overline{w}}$ as (Rivero & Arcilla (1995)):

$$\frac{\partial}{\partial z}\left(\widetilde{\overline{u}}\widetilde{\overline{w}}\right) = -\frac{1}{2}\frac{\partial}{\partial x}\left(\widetilde{\overline{u^2}} - \widetilde{\overline{w^2}}\right) \tag{C.5}$$

Dropping the tildes over wave velocity ($\widetilde{u} = u$), we combine this expression with the other wave velocity terms in Equation 3.14 to obtain (Garcez-Faria *et al.* (2000)):

$$\frac{\partial \overline{u^2} - \overline{w^2}}{\partial x} + \frac{\partial \overline{uw}}{\partial z} = \frac{1}{2}\frac{\partial \overline{u^2} - \overline{w^2}}{\partial x} \tag{C.6}$$

We further simplify this latter equation by using the LWT expressions of u and w to obtain a depth uniform term (Longuet-Higgins & Stewart (1962), Dally (1980), Rivero & Arcilla (1995)):

$$\rho(\overline{u^2} - \overline{w^2}) = \frac{2kE_w}{\rho \sinh(2kh)} \tag{C.7}$$

The wave radiation stress is expressed as (Longuet-Higgins & Stewart (1962, 1964)):

$$\begin{aligned} S_{xx} &= \overline{\int_{-h}^{\eta} \rho\widetilde{u}^2 + p\,dz} - \frac{1}{2}\rho g(h+\overline{\eta})^2 \\ &= E_w\left(2\frac{C_g}{C} - \frac{1}{2}\right) \\ &= \frac{2khE_w}{\sinh 2kh} + \frac{E_w}{2} \end{aligned} \tag{C.8}$$

so, Equation C.7 becomes:

$$\rho(\overline{u^2} - \overline{w^2}) = \frac{S_{xx} - E/2}{h} \tag{C.9}$$

C.3 Dimensional Analysis for Mean Vertical Velocity

To estimate the relative order of mean vertical velocity with respect to mean horizontal velocity, we first decompose horizontal and vertical velocities into mean, wave and turbulent components:

$$u = U + \widetilde{u} + u' \tag{C.10}$$

$$w = W + \widetilde{w} + w' \tag{C.11}$$

We apply this decomposition to the continuity equation, Equation 3.2, and obtain after wave-averaging:

$$\frac{\partial U}{\partial x} + \frac{\partial W}{\partial x} = 0 \tag{C.12}$$

Now, we assume that mean velocities vary on an horizontal length scale $X = L_U$, which is much longer than the wave length scale $L_w = 2\pi/k$, a vertical length scale equal to the total water depth $Z = h$, and a time scale T_U which is much larger than the waves timescale $T_w = 2\pi/\sigma$. We then define non-dimensional velocities U^* and W^* as: $U^* = T_U U/L_U$ and $W^* = T_U W/L_U$, and we define non-dimensional length scale as:$x^* = x/X$ and $z^* = z/Z$. Hence the wave-averaged continuity equation becomes:

$$\frac{\partial U}{\partial x} + \frac{\partial W}{\partial x} = \frac{L_U}{T_U}\frac{1}{L_U}\frac{\partial U^*}{\partial x^*} + \frac{L_U}{T_U}\frac{1}{h}\frac{\partial W^*}{\partial z^*} \tag{C.13}$$

which yields $W \sim \epsilon U$, with $\epsilon = h/L$. Consequently, in the wave-averaged horizontal momentum equation, Equation 3.14, we have:

$$\frac{\partial U^2}{\partial x} + \frac{\partial W^2}{\partial x} = \frac{L_U^2}{T_U^2}\frac{1}{L_U}\frac{\partial U^{*2}}{\partial x} + \frac{L_U^2}{T_U^2}\frac{1}{L_U}\frac{\partial W^{*2}}{\partial z^*} \tag{C.14}$$

which means that $\partial_x W^2 \sim \epsilon^2 \partial_x U^2$. We now decide that, although we will keep terms of order ϵ in the remainder of this paper, we will neglect terms of order ϵ^2. Consequently, we will neglect terms in W^2, but keep terms in W in the wave-averaged horizontal momentum equation.

C.4 Evolution Equation for M^w

The wave action equation reads (Mei (1989); Svendsen (2006)):

$$\frac{\partial}{\partial t}\frac{E_w}{\sigma_r} + \frac{\partial}{\partial x}\frac{E_w(C_g + U_r)}{\sigma_r} = -\frac{\mathcal{D}}{\sigma_r} \tag{C.15}$$

where $A = E_w/\sigma_r$ is the wave action, and $(2\pi/T - U_r k)^2 = \sigma_r^2 = gk \tanh kh$. Expanding this equation by recognizing that the net wave momentum M^w is $M^w = Ak = kE_w/\sigma_r =$

E_w/C gives:

$$\frac{\partial M^w}{\partial t} + \frac{\partial}{\partial x} M^w (C_g + U_r) - A \left(\frac{\partial k}{\partial t} + (C_g + U_r) \frac{\partial k}{\partial x} \right) = -\frac{k\mathcal{D}}{\sigma_r} \tag{C.16}$$

To simplify this expression, we use the expression of the kinematical conservation equation (Phillips (1977), p.23):

$$\frac{\partial k}{\partial t} + \nabla(\sigma_r + kU_r) = \frac{\partial k}{\partial t} + (C_g + U_r)\frac{\partial k}{\partial x} + k\frac{\partial U_r}{\partial x} + \frac{\partial \sigma_r}{\partial h}\frac{\partial h}{\partial x} = 0 \tag{C.17}$$

where we used $\partial_k \sigma_r = C_g$. Hence, Equation C.16 becomes:

$$\frac{\partial M^w}{\partial t} + \frac{\partial}{\partial x} M^w (C_g + U_r) = -\frac{k\mathcal{D}}{\sigma_r} - A \left(k\frac{\partial U_r}{\partial x} + \frac{\partial \sigma_r}{\partial h}\frac{\partial h}{\partial x} \right) \tag{C.18}$$

Equation C.18 is further simplified by expressing $A\partial_h \sigma_r$ using the expression of C_g and trigonometric identities:

$$\frac{E_w}{\sigma_r}\frac{\partial \sigma_r}{\partial h} = \frac{E_w}{\sigma_r}\frac{\sigma_r k}{\sinh(2kh)} = kE\frac{2n-1}{2kh} \tag{C.19}$$

where $n = C_g/C$. Consequently Equation C.18 becomes (see Smith (2006), Equation 2.27):

$$\frac{\partial M^w}{\partial t} + \frac{\partial}{\partial x} M^w (C_g + U_r) = -\frac{k\mathcal{D}}{\sigma_r} - M^w \frac{\partial U_r}{\partial x} - M^w \frac{E(n-1/2)}{h}\frac{\partial h}{\partial x} \tag{C.20}$$

Recognizing that $S_{xx} = 2M^w C_g - E/2 = E(2n-1/2)$, we can rewrite Equation C.20 as:

$$\frac{\partial M^w}{\partial t} + \frac{\partial S_{xx}}{\partial x} - \frac{\partial}{\partial x}\frac{E(2n-1)}{2} - h\frac{E(2n-1)}{2}\frac{\partial}{\partial x}\left(\frac{1}{h}\right) + \frac{\partial M^w U_r}{\partial x} + M^w \frac{\partial U_r}{\partial x} = -\frac{\mathcal{D}}{C} \tag{C.21}$$

Finally, the wave action equation becomes:

$$\frac{\partial M^w}{\partial t} + \frac{\partial S_{xx}}{\partial x} - h\frac{\partial}{\partial x}\left(\frac{S_{xx} - E/2}{2h}\right) + \frac{\partial M^w U_r}{\partial x} + M^w \frac{\partial U_r}{\partial x} = -\frac{\mathcal{D}}{C} \tag{C.22}$$

C.5 Derivation of Undertow Forcing for Depth-Uniform Horizontal Current

In Section 3.2.4, we derived an expression for the solution of the wave-averaged momentum equation, Equation 3.16, using a bottom shear stress boundary condition:

$$\tau(z) = (F + P)(z + d) + \rho\frac{\partial}{\partial x}\int_{-d}^{z} U^2\, dz - \rho U^2 \frac{\partial z}{\partial x} + \rho UW + \tau_b \tag{C.23}$$

We can simplify the nonlinear terms of this expression assuming a weak vertical variation of the mean horizontal current, i.e. $U(x,z) = U_r(x,z) + \epsilon U_1(x,z)$, with $\epsilon << 1$:

$$\begin{aligned}\rho\frac{\partial}{\partial x}\int_{-d}^{z} U^2\,dz + \rho UW &= \int_{-d}^{z}\rho\frac{\partial U_r^2}{\partial x} + \rho\frac{\partial U_r W}{\partial z}\,dz \\ &= \rho\frac{\partial U_r^2}{\partial x}(z+d) + \rho(W(z) - W(-d)) \\ &= \rho U_r\frac{\partial U_r}{\partial x}(z+d) - \rho U_r^2\frac{\partial z}{\partial x} \end{aligned} \tag{C.24}$$

where we neglected $\partial_x z$ and used the integral the wave-averaged continuity equation (Equation 3.2) between z and -d: $(z+d)\partial_x U_r + W(z) - W(-d) = 0$. Hence Equation C.23 becomes:

$$\rho\nu_t\frac{\partial U}{\partial z} = \left[\frac{\partial}{\partial x}\left(\frac{S_{xx} - E/2}{2h}\right) + \rho g\frac{\partial\overline{\eta}}{\partial x} + \rho U_r\frac{\partial U_r}{\partial x}\right](z+d) + \tau_b \tag{C.25}$$

Similarly, the expression for the solution of the wave-averaged momentum equation, Equation 3.16, using a shear stress at the MWL as boundary condition was:

$$\rho\nu_t\frac{\partial U}{\partial z} = (F+P)(z-\overline{\eta}) - \rho\frac{\partial}{\partial x}\int_{z}^{\overline{\eta}} U^2\,dz - \rho U^2\frac{\partial z}{\partial x} + \rho UW - \rho U_{|\overline{\eta}}\frac{\partial M^w}{\partial x} + \tau_s \tag{C.26}$$

and after simplifying the nonlinear terms in this equation, assuming a weak vertical variation of the mean horizontal current, and invoking the wave-averaged continuity equation (Equation 3.2) between z and MWL $\overline{\eta}$, we obtain:

$$\rho\frac{\partial}{\partial x}\int_{z}^{\overline{\eta}} U^2\,dz - \rho U^2\frac{\partial z}{\partial x} + \rho UW - \rho U_{|\overline{\eta}}\frac{\partial M^w}{\partial x} = \rho U_r\frac{\partial U_r}{\partial x}(\bar{\eta} - z) \tag{C.27}$$

and we obtain in Equation C.26:

$$\rho\nu_t\frac{\partial U}{\partial z} = \left[\frac{\partial}{\partial x}\left(\frac{S_{xx} - E/2}{2h}\right) + \rho g\frac{\partial\overline{\eta}}{\partial x} + \rho U_r\frac{\partial U_r}{\partial x}\right](z - \overline{\eta}] + \tau_s \tag{C.28}$$

Subtracting Equation C.28 from Equation C.25 yields the steady state mean momentum equation:

$$h\frac{\partial}{\partial x}\left(\frac{S_{xx} - E/2}{2h}\right) + \rho g h\frac{\partial\bar{\eta}}{\partial x} + \rho h U_r\frac{\partial U_r}{\partial x} + \tau_b - \tau_s = 0 \tag{C.29}$$

Finally, if we express $F + P$ from Equation C.25, we find that Equation C.29 becomes:

$$\rho\nu_t\frac{\partial U}{\partial z} = \frac{\tau_s - \tau_b}{h}(z+d) + \tau_b \tag{C.30}$$

where all explicit non-linear terms have now vanished.

We now point out that Equation C.29 is identical to the steady state momentum

equation derived in Section 3.2.3, Equation 3.28, because:

$$\begin{aligned}\frac{\partial U_r^2 h}{\partial x} + U_r \frac{\partial M^w}{\partial x} &= 2hU_r \frac{\partial U_r}{\partial x} - U_r h \frac{\partial U_r}{\partial x} \\ &= hU_r \frac{\partial U_r}{\partial x} \end{aligned} \tag{C.31}$$

These equalities are exact because $hU_r = -M^w$. But, in the surf zone, $hU_r = -M^r + M^w$. So, for Equation C.31 to hold, we need to redefine M^w as $M^w = M^w + M^r$ (see Svendsen (1984a)). But if we do so, then we can no longer arrive at the wave action equation, Equation 3.29, since it was derived in Section C.4 by taking $M^w = E_w/C$.

Consequently, for all equations to be consistent, we need to take roller into account in the evolution of wave action. This problem illustrates once again the need to develop a rigorous equation for the wave roller evolution that can be incorporated in the momentum equation.

C.6 Solutions to Eddy Viscosity Parametrizations

Equations 3.35, 3.36 and 3.38 are all of the form:

$$\nu_t \frac{\partial U}{\partial z} = Az + B \tag{C.32}$$

The solution to this equation for the different formulations of eddy viscosity presented in Section 3.3 are:

1. If $\nu_t = \alpha$, then $U(x,z) = \frac{A}{2\alpha} z^2 + \frac{B}{\alpha} z + C$,
2. If $\nu_t = \alpha z + \beta$, then $U(x,z) = \frac{A}{\alpha} z + \frac{B\alpha - A\beta}{\alpha^2} \ln(\alpha z + \beta) + C$,
3. If $\nu_t = \alpha\sqrt{z} + \beta$, then $U(x,z) = \frac{2A}{3\alpha} z^{3/2} - \frac{A\beta}{\alpha^2} z + \frac{2(A\beta^2 + B\alpha^2)\sqrt{z}}{\alpha^3} - \frac{2(A\beta^3 + B\alpha^2\beta)\ln(\alpha\sqrt{z}+\beta)}{\alpha^4} + C$,
4. If $\nu_t = \alpha(z - z^2) + \beta$, then $U(x,z) = (A + 2B)\frac{arctanh(\frac{a(2x-1)}{\sqrt{a^2+4ba}})}{\sqrt{a^2+4ba}} - A\frac{\ln(ax^2 - ax - b)}{2a} + C$,
5. If $\nu_t = \alpha(h + z)\sqrt{h + z}$, then $U(x,z) = \frac{2(A(z+2h) - B)}{\alpha\sqrt{h+z}} + C$,
6. If $\nu_t = \alpha \exp(-\beta z)$, then $U(x,z) = \frac{A + \beta A z + \beta B}{\alpha\beta^2} \exp(\beta z) + C$

where α and/or β are calibration constants, and C is a constant of integration.